





# Measurements of Transitions between Different Hyperfine Structure Substates of Hydrogen using a Sona Transition Unit

#### MASTER THESIS

Author:
Hendrik Smitmanns

First examiner:
Prof. Dr. Andreas Lehrach
Second examiner:
Prof. Dr. Jörg Johannes Pretz

The present work was submitted to the III. Physikalisches Institut B in fulfillment of the requirements for the degree of Master of Science.

## Abstract

Nuclear spin polarization and its phenomena have been studied since the early days of quantum mechanics. Today, in particular, nuclear spin polarized hydrogen and deuterium are used in many ways, e.g. as target material or in the form of polarized beams. One way of measuring the polarization of such a beam is the Lambshift polarimeter. In an experiment conducted at the Institut für Kernphysik of the Forschungszentrum Jülich to study the influence of a Sona transition unit on the polarization of a nuclear spin-polarized hydrogen beam, unexpected oscillations of the occupation numbers of different hyperfine substates of hydrogen atoms as a function of the magnetic field were discovered. The oscillations are induced within the Sona transition unit, which allows an exchange of the occupation numbers of the  $\alpha_1$  and  $\beta_3$  states by reversing the direction of the magnetic field defining the quantization axis. The transition energies between the different substates were in the range of only a few neV.

In order to investigate this phenomenon further, a similar experiment is set up in Jülich which allows measuring these oscillations of the occupation numbers of metastable  $2S_{1/2}$  hydrogen as well as the recording of the thereby produced spectra of the two  $\alpha$  states. In addition, an analysis method is developed and applied to determine the energies of the transitions that occur between the different substates. The aim of the method is to measure these transition energies with an accuracy that allows the QED corrections to the classical Breit-Rabi formula to be detected.

## Zusammenfassung

Die Kernspinpolarisation und deren Phänomene werden seit den frühen Tagen der Quantenmechanik untersucht. Heute werden insbesondere kernspinpolarisierter Wasserstoff und Deuterium in vielfältiger Weise genutzt, entweder als Target oder in Form von polarisierten Strahlen. Eine Möglichkeit die Polarisation eines solchen Strahls zu messen ist das Lambshift-Polarimeter. In einem am Institut für Kernphysik des Forschungszentrums Jülich durchgeführten Experiment zur Untersuchung des Einflusses einer Sona-Übergangseinheit auf die Polarisation eines kernspinpolarisierten Wasserstoffstrahls wurden unerwartete Oszillationen der Besetzungszahlen von verschiedenen Hyperfeinstrukturunterzuständen der Wasserstoffatome als Funktion des Magnetfeldes entdeckt. Die Übergänge werden innerhalb der Sona-Übergangseinheit induziert, die einen Austausch der Besetzungszahlen der  $\alpha_1$  und  $\beta_3$  Zustände durch Umkehrung der Richtung des Magnetfeldes, welches die Quantisierungsachse definiert, ermöglichen. Die Übergangsenergien zwischen den beobachteten Übergängen lagen dabei im Bereich von einigen neV.

Um dieses Phänomen weiter zu untersuchen, wurde in Jülich ein ähnliches Experiment aufgebaut, das die Messung der Oszillationen der Besetzungszahlen von metastabilem  $2S_{1/2}$ -Wasserstoff sowie die Aufnahme der dabei erzeugten Spektren der beiden  $\alpha$ -Zustände erlaubt. Darüber hinaus wird eine Analysemethode entwickelt und angewendet, um die Energien der Übergänge zwischen den verschiedenen Unterzuständen zu bestimmen. Ziel der Methode ist es, diese Übergangsenergien mit einer Genauigkeit zu messen, die es erlaubt, die QED-Korrekturen zur klassischen Breit-Rabi-Formel zu quantifizieren.

## Contents

$\mathbf{A}$	bstra	$\mathbf{ct}$		iii
$\mathbf{Z}$ ι	ısam	menfa	ssung	v
Li	st of	Figur	es	ix
1	Intr	oduct	ion	1
2	The	eoretic	al Framework	3
	2.1	Atomi	ic Theory	3
		2.1.1	Hydrogen	3
		2.1.2	Angular Momentum	4
		2.1.3	Stern-Gerlach Effect	5
		2.1.4	Fine Structure	6
		2.1.5	Hyperfine Structure	7
		2.1.6	Lamb-shift	8
		2.1.7	Zeeman and Paschen-Back Effect of the Hyperfine Structure $$ .	10
		2.1.8	Stark Effect and the Metastable $2S_{1/2}$ State	11
		2.1.9	Polarization	12
	2.2	Breit	Rabi Formula	13
		2.2.1	The Breit-Rabi Formula for Hydrogen	13
		2.2.2	The Breit-Rabi Formula for Hydrogen including QED Corrections	s 14
	2.3	Lamb-	-Shift Polarimeter	18
		2.3.1	Ionizer	18
		2.3.2	Wienfilter	19
		2.3.3	Cesium Cell	20
		2.3.4	Spin Filter	21
		2.3.5	Quenching Chamber	24
	2.4	Sona '	Transition	25
3	Exp	erime	ntal Setup	31
	3.1	Electr	on Cyclotron Resonance Ion Source	32
	3.2	Wienf	filter	32
	3.3	Cesiui	m Cell	32
	3.4	Spin I	Filters	33

		3.4.1 Solenoid	35
		3.4.2 Cavity	35
	3.5	Sona Transition Unit	37
	3.6	Quench Chamber	39
	3.7	Problems during the Measurements	39
		3.7.1 ECR Plasma	39
		3.7.2 Spin Filter Stray Fields	40
4	Mea	asurements and Analysis	43
	4.1	Principle of Measurement	43
	4.2	Principle of Analysis	45
		4.2.1 Search for the Peak Positions	46
		4.2.2 Fits to the Breit-Rabi Transition Energies	48
	4.3	Comparison of the Measurements Series	53
5	Con	nclusions and Outlook	57
	5.1	Conclusions	57
	5.2	Outlook	59
A	$\mathbf{Bre}$	eit Rabi formula Coefficients	61
В	Pho	otos of the Experimental Setup	63
$\mathbf{C}$	List	ting of the Measurement and Fit Parameters	69
	C.1	Listing of the Measurement Parameters	69
	C.2	Listing of the Fit Parameters	70
Bi	bliog	graphy	71
Ad	cknov	wledgements	75

# List of Figures

2.1	Scheme of the Stern-Gerlach experiment	1
2.2	Term scheme of the hydrogen atom	Ĝ
2.3	Digrams to illustrate the Zeeman and Paschen-Back effect	10
2.4	Lifetime of the $2S_{1/2}$ -state as function of an external electirc field	11
2.5	Breit-Rabi diagram of the $1S_{1/2}$ state of hydrogen	15
2.6	Breit-Rabi diagram of the $1S_{1/2}$ -state of hydrogen, including QED-	
	corrections	16
2.7	Difference between the conventional Breit-Rabi formula and the version	
	that includes QED corrections	17
2.8	Schematic of the Lamb-shift polarimeter	18
2.9	Cross-section of charge transfer reactions of Hydrogen ions with Caesium	2
2.10	Breit-Rabi diagram of the $2S_{1/2}$ - and $2P_{1/2}$ -state	22
2.11	Working principle of the spin filter	23
2.12	Exemplary Lyman- $\alpha$ spectrum of polarised hydrogen measured with a	
	LSP	24
2.13	Scheme of the working principle of the LSP	25
2.14	Sketch of a Sona transition unit	26
2.15	Breit-Rabi diagram of the $2S_{1/2}$ state of hydrogen extended to negative	
	magnetic fields	27
2.16	Example of multi photon transitions in $2S_{1/2}$ hydrogen induced inside	
	a Sona transition unit	29
2.17	Simulation of the occupation numbers of three hyperfine substates of	
	$2S_{1/2}$ hydrogen in a Sona transition unit	29
3.1	Schematic drawing of the experimental setup	31
3.2	Schematic drawing of a cesium cell	33
3.3	Schematic drawing of a spin filter	34
3.4	Longitudinal magnetic field along the spin filter beam axis at different	
		35
3.5		36
3.6	Longitudinal magnetic field configuration of the Sona transition unit	
	and both spin filters	37
3.7	Longitudinal magnetic field $B_z$ of the Sona transition unit for different	
		38

3.8	Calculated radial magnetic field $B_r$ of the Sona transition unit for	20
	different currents	38
3.9 3.10	Wienfilter mass spectrum of the ion beam generated by the ECR source Longitudinal magnetic fields of the Sona transition unit for different	40
	magnetic field settings of the second spin filter	41
3.11	Influence of stray fields of the second spin filter on the Sona transition	
	unit	41
4.1	Measured Sona spectrum of the $\alpha_1$ state of the measurement series	4.4
4.2	'E1270'	44
	'E1270'	44
4.3	Sona transition energies as function of the longitudinal magnetic field	46
4.4	Lorentz curves fitted on the measured $\alpha_1$ spectrum of the measurement series 'E1270'	47
4 =		47
4.5	Lorentz curves fitted on the measured $\alpha_2$ spectrum of the measurement series 'E1270'	47
4.6	Plot of the measured data points and fit functions using the parameters	
	of the $\alpha_1 - \alpha_2$ transition fit of the measurement series 'E1270'	49
4.7	Residuals of the $\alpha_1 - \alpha_2$ transition energy fits of the measurement series	
	'E1270'	50
4.8	Residuals of the $\alpha_1 - \alpha_2$ transition energy fits of the measurement series	
	'E1270' (only $\alpha_1 - \alpha_2$ )	50
4.9	Plot of the measured data points and fit functions using the parameters	<b>-</b> 1
4.10	of the $\alpha_2 - \beta_3$ transition fit of the measurement series 'E1270'	51
4.10	Residuals of the $\alpha_2 - \beta_3$ transition energy fits of the measurement series 'E1270'	51
4.11	Residuals of the $\alpha_2 - \beta_3$ transition energy fits of the measurement series	
	'E1270' (only $\alpha_2 - \beta_3$ )	52
4.12	Energy of the basic photon energy $\Delta E_{Sona}$ as function of $E_{kin}$ for all	
4.10	measurement series	54
4.13	Energy of the basic photon energy $\Delta E_{Sona}$ as function of $E_{kin}$ for all measurement series (Zoom)	54
4.14	Magnetic scaling parameter $\mathbf{B_{sca}}$ as function of $E_{kin}$ for all measure-	
	ment series	55
4.15	Magnetic offset parameter $\mathbf{B}_{\mathbf{off}}$ as function of $E_{kin}$ for all measurements	
	series	55
B.1	Photo of the complete experimental setup	63
B.2	Photo of the ECR ion source	64
B.3	Photo of the Wienfilter	64
B.4	Photo of the cesium cell	65
	Photo of the first spin filter	65

B.6	Photo of the Sona transition unit	66
B.7	Photo of the second spin filter	66
B.8	Photo of the quench chamber with the photomultiplier tube on top	67
B.9	Photo of the cross connection between ECR and Wienfilter	68

## Chapter 1

## Introduction

Since the days of Joseph von Fraunhofer [1] with the discovery of absorption lines in the optical spectrum of the Sun in 1814, the study of spectral lines became an important field of research in modern physics. In 1897, Johann Jakob Balmer [2] succeeded in the first mathematical description of such lines for hydrogen, but it was not until the emergence of quantum mechanics in the 20th century that spectral lines could be understood as transitions of electrons between different energetic bonding states. During the 20th century, more and more precise methods were developed in order to investigate these binding energies. For example, today, the transition between the  $1S_{1/2}$  and  $2S_{1/2}$  states of hydrogen is measured with an uncertainty of  $10^{-14}$ eV using 2-photon spectroscopy.

Some spectroscopy experiments as well as multiple other kinds of experiments are conducted using nuclear spin-polarized hydrogen and deuterium atoms and ions. Thereby, polarized beams as well as targets are of equally interest in experimental nuclear physics. Polarization observables can be utilized as an additional quantity to give deeper insights in physics of nuclear and particle reactions than with cross-sections alone. One way to measure the polarization of particle beams with an accuracy of 1% [3] is the Lamb-shift polarimeter, which utilizes the fact that the metastable  $2S_{1/2}$ state and the very short-lived  $2P_{1/2}$  state are separated by the Lamb-shift, but can be coupled using the right combination of static electric and magnetic fields, and a radiofrequency. At the Institut für Kernphsik at the Forschungszentrum Jülich Lamb-shift polarimeters were and are in use in many experiments, like at the ANKE experiment [4], or in recombination experiments where polarized atoms recombine to molecules [5, 6]. However, this kind of polarimeter is only able to detect the  $\alpha_1$  and  $\alpha_2$  substates. But for some experiments, like the BoB experiment [7], it is necessary to be able to measure the  $\beta_3$  substate as well. Therefore, a combination of a Lambshift polarimeter and a Sona transition unit was set up to allow such measurements, because a Sona-transition unit is able to exchange the occupation numbers of the hyperfine substates  $\alpha_1$  and  $\beta_3$  by rotating the quantization axis faster than the Larmor precession can follow. During the first experiments with this setup, it was discovered that the Sona transition unit induces unexpected oscillations between the occupation numbers of the different hyperfine substates of the metastable particles as a function of the internal magnetic field of the Sona transition unit [8].

This thesis is dedicated to further investigate these oscillations. Therefore, at the Institut für Kernphysik an experiment is set up, including a Lamb shift polarimeter and a Sona transition unit. Using an electron cyclotron ion source in combination with the previously mentioned components, the oscillations between the occupation numbers can be created and the recording of the thereby resulting  $\alpha_1$  and  $\alpha_2$  spectra. Thereby, two main goals are pursued. The first is to measure the oscillation spectra at a higher resolution than in the previous experiment, and the second is to calculate the transition energies between the induced transitions accurately enough to detect the QED correction to the Breit-Rabi formula [9]. Therefore, a new analysis method is applied and tested that attempts to relate the structure of the spectra to the Breit-Rabi formula.

The structure of this thesis is as follows. Firstly, in chapter 2, a theoretical introduction to atomic physics and the physics of the different experimental components are presented, as well as an introduction to the classical Breit-Rabi forumla and the one which includes QED corrections. Afterwards, in chapter 3, the experimental setup is explained in detail and problems of the setup which were discovered during and after the measurements are discussed. In chapter 4, the measurement principle is addressed, and the analysis method used in this thesis to investigate the measured data is explained. At the end, in chapter 5, the results of the measurements and the applied fitting method and its limits are critically discussed and an outlook on future improvements and applications of the presented experiment is given.

## Chapter 2

## Theoretical Framework

#### 2.1 Atomic Theory

Since the classical antiquity, people developed the idea of atoms as the fundamental building blocks of nature, from which everything is made of. They were considered us uncuttable particles too small to be investigated. Since then, the knowledge about atoms has dramatically increased.

The topic really accelerated at the end of the 19th century. In 1897, Joseph J. Thomson [10] discovered the electron as a negative charged particle that is part of atoms. This brought up the first models to describe the inner structures of atoms. In 1907, Ernest Rutherford [11] could show with his famous experiment that inside the atom exists a heavy nucleus, which is positively charged and includes nearly all the mass of the atom. Based on this, in 1913, Niels Bohr [12] proposed his first atom model of electrons bound on fixed trajectories around the nucleus. He stated, that electrons are only allowed to possess angular momenta which are multiples of the Plank constant h, and, thus, starting the idea of quantum mechanics.

In 1924, Louis de Broglie [13] postulated that particles can also process a wave-like character. After this, Erwin Schrödinger [14] postulated his Schrödinger equation. For the spinless electron, in the Dirac notation, the Schrödinger equation can be written as

$$\hat{H}|\psi\rangle = E|\psi\rangle , \qquad (2.1)$$

where  $\hat{H}$  is the Hamilton operator of the electron, E its energy eigenvalues and  $|\psi\rangle$  describes the state of the electron. In opposite to Bohr's model, electrons do not follow trajectories around the nucleus, but instead are just probability functions of electrons located inside a volume. Later, in 1928 Paul Dirac [15] established a theory also including relativity and spins of the electron into the model.

#### 2.1.1 Hydrogen

Hydrogen is the most frequent element in the universe. On Earth, it is mostly found bound in chemical compounds, among which water H<sub>2</sub>O is most common. In experiments, most of the time atomic hydrogen is used, produced by dissociation of molecular hydrogen H<sub>2</sub>.

In nature, hydrogen occurs in three forms, two of which are stable, namely normal hydrogen (<sup>1</sup>H), which consists of one proton and one electron, and deuterium (<sup>2</sup>H or D), also called heavy hydrogen, whose nucleus contains an additional neutron. The third form is tritium (<sup>3</sup>H or T) whose nucleus contains two additional neutrons. Tritium is unstable and thus highly radioactive, making it difficult to use in experiments.

#### 2.1.2 Angular Momentum

Each electron bound to an atomic orbit posses an orbital angular momentum. In general, the angular momentum  $\vec{L}$  is defined as

$$\vec{L} = \vec{r} \times \vec{p} \,\,, \tag{2.2}$$

where  $\vec{r}$  is the rotational axis and  $\vec{p}$  is the linear momentum. In quantum mechanics,  $\hat{\mathbf{L}}$ ,  $\hat{\mathbf{r}}$  and  $\hat{\mathbf{p}}$ , as being observable variables, are expressed as operators, for which the Equation 2.2 also holds. Applying the canonical commutation relation to  $\hat{\mathbf{r}}$  and  $\hat{\mathbf{p}}$  one gets,

$$[\hat{r}_k, \hat{p}_l] = i\hbar \delta_{kl} , \qquad (2.3)$$

which is a representation of the Heisenberg uncertainty principle [16]. In combination with Equation 2.2, it results in the commutation relation for the angular momentum,

$$[\hat{L}_k, \hat{L}_l] = i\hbar \epsilon_{klm} \hat{L}_m . \tag{2.4}$$

As a consequence of Equation 2.4, only one component of the angular momentum can be observed at the same time.  $\hat{L}^2 = \hat{L}_x^2 + \hat{L}_y^2 + \hat{L}_z^2$  commutes with its single components  $\hat{L}_{x,y,z}$ ,

$$[\hat{L}^2, \hat{L}_x] = [\hat{L}^2, \hat{L}_y] = [\hat{L}^2, \hat{L}_z] = 0.$$
 (2.5)

So,  $\hat{L}^2$  and a single component  $\hat{L}_z^{-1}$  of an angular momentum can be measured simultaneously. Their eigenfunctions  $|l, m_l\rangle$  can be defined as

$$\widehat{L}^2|l,m_l\rangle = \hbar^2 \ l \ (l+1) \ |l,m_l\rangle \ , \tag{2.6}$$

$$\widehat{L}_z^2|l,m_l\rangle = \hbar \ l|l,m_l\rangle \ . \tag{2.7}$$

Using ladder operators  $\hat{L}_{\pm} = \hat{L}_x \pm i \ \hat{L}_y$ , one can derive that

$$l = 0, 1, 2, \dots$$
 or  $l = \frac{1}{2}, \frac{3}{2}, \frac{5}{2}, \dots$  (2.8)

$$m_l = -l, -(l-1), ..., (l+1), l.$$
 (2.9)

For an orbital angular momentum of an electron, only integer values are allowed for l. Therefore, for an electron bound to an atomic orbit, one defines the quantum

<sup>&</sup>lt;sup>1</sup>One usually uses the z-component.

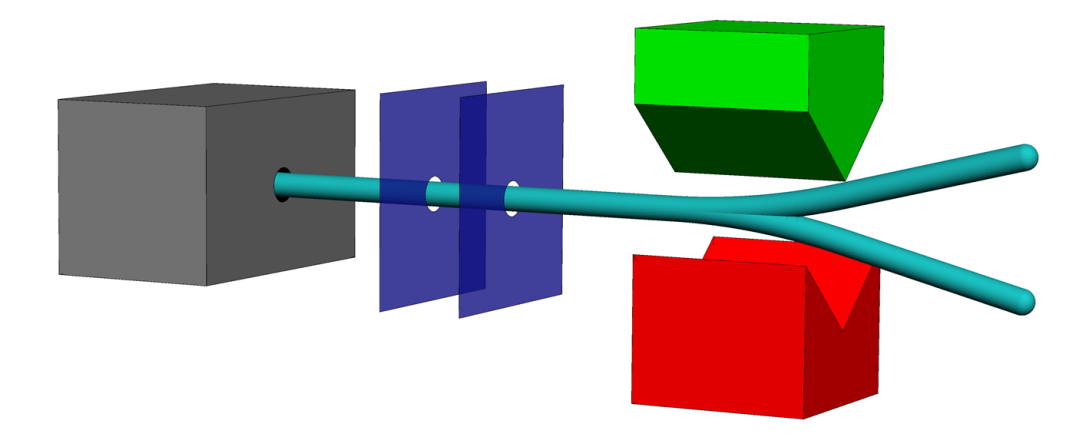


FIGURE 2.1: Scheme of the Stern-Gerlach experiment [18]. A beam of silver atoms created by a furnace and a set of collimators splits inside an inhomogeneous magnetic field created by two magnets.

number of the angular momentum  $\ell^2$  and the magnetic quantum number of the angular momentum  $m_{\ell}$ . The half integer values are a solution for the spin, which will be explained in subsection 2.1.3.

For an electron on a specific electron shell, which is described by the principal quantum number n,  $\ell$  can take the following values

$$\ell = 0, 1, 2, ..., (n-1),$$
 (2.10)

while n ranges from 1 to the shell containing the weakest bound electron.

#### 2.1.3 Stern-Gerlach Effect

In 1922, Otto Stern and Walther Gerlach [17] demonstrated that electric neutral silver atoms posses a magnetic moment. They produced a beam of silver atoms using an evaporating furnace and a set of collimators. The beam was guided through an inhomogeneous magnetic field with a strong gradient in the vertical (z-) direction to hit a photographic plate. A scheme of the experiment is shown in Figure 2.1.

Based on the theory of classical physics, the silver beam should have created a picture with a continuous distribution. However, the observed picture showed two from each other isolated impact positions on the photographic plate. Both positions were shifted, one upward, one downward, contrary to a beam that did not traverse an inhomogeneous magnetic field. Therefore, the atoms needed to carry a magnetic moment  $\vec{\mu}$ , because the potential V inside the magnetic field  $\vec{B} = B(z)\vec{e_z}$  is given by

$$V = -\vec{\mu} \cdot \vec{B} \ . \tag{2.11}$$

<sup>&</sup>lt;sup>2</sup>Note, that  $\ell$  is only used for the angular momentum of an electron bound to an atomic orbit, while l can stand for any angular momentum.

The force created by this potential is given by

$$\vec{F} = -\vec{\nabla} \ V = -\mu_z \cdot \frac{\partial B_z}{\partial z} \ \vec{e_z} \ . \tag{2.12}$$

At that time, the quantization of the magnetic moment caused by a quantized angular momentum was already expected. However, since half-integer quantum numbers were still unknown, it was expected that the beam would split into an odd number of  $(2\ell+1)$  beams according to the magnetic quantum number of the angular momentum  $m_{\ell}$ , and not into two as in the experiment.

A few years later, this phenomenon was explained with the electron spin. In 1925, Samuel Goudsmit and George E. Uhlenbeck [19] introduced the idea of an intrinsic angular momentum of the electron, the electron spin s. In 1927, Thomas E. Phipps and John B. Taylor [20] repeated the Stern-Gerlach experiment with a beam of atomic hydrogen and again observed a bisection of the beam, further supporting the electron spin hypothesis.

The electron spin can only take values that are odd multiples of  $\frac{1}{2}$ . As later discovered, not only electrons but every particle possess a spin. The spin describes a fundamental property of particles, separating them in two classes, Bosons with integer spins (s = 0, 1, 2, ...) and Fermions with half-integer spins  $(s = \frac{1}{2}, \frac{3}{2}, \frac{5}{2}, ...)$ . The spin behaves mathematically identical to an angular momentum. Therefore, for a spin s, one can find the magnetic quantum number of the spin  $m_s$ . Similar to  $m_\ell$  described in subsection 2.1.2,  $m_s$  can take values of

$$m_s = -s, -(s-1), ..., (s+1), s.$$
 (2.13)

So in case of an electron, one has  $s=\frac{1}{2}$ , leading to two possible orientations in the magnetic field,  $m_s=+\frac{1}{2}$  which is commonly referred to as "spin up" and  $m_s=-\frac{1}{2}$  which is referred to as "spin down". The projections on the quantization axis are either  $s_z=\pm\frac{1}{2}\hbar$  and the magnetic moment  $\mu_s$  created by the electron spin is given by

$$\mu_s = -g_s \cdot \mu_B \cdot m_s, \quad \text{with} \quad \mu_B = \frac{e \cdot \hbar}{2m_e} .$$
 (2.14)

 $\mu_B$  is called the Bohr magneton,  $m_e$  is the electron mass, e is the elementary charge and  $g_s$  <sup>3</sup> is the Landé factor of the electron spin. When one assumes that the atoms in the experiments were in the ground state ( $\ell = 0$ ), the splitting of the beams can be explained with the magnetic moment of the electrons, which can obtain two different values.

#### 2.1.4 Fine Structure

With the electron spin, it was now also possible to explain the structure of the spectral lines. Already in 1887, Albert A. Michelson and Edward W. Morley [22] discovered

 $<sup>^{3}</sup>g_{s} \approx 2.00231930436182(52)[21]$ 

fine splittings in the spectral lines of hydrogen. These are created by the interaction of the magnetic moments created by the electron spin  $\vec{s}$  and the angular momentum of the electron  $\vec{\ell}$ . Both momenta combine to the total angular momentum of the electron  $\vec{J}$ , with

$$|\vec{\ell} - \vec{s}| \le |\vec{J}| \le |\vec{\ell} + \vec{s}| .$$
 (2.15)

The energy splitting  $\Delta E_{\ell,s}$  for hydrogen, created by this interaction, is

$$\Delta E_{\ell,s} = \frac{a}{2} [(J(J+1) - \ell(\ell+1) - s(s+1)]. \qquad (2.16)$$

The quantity a is the spin orbit interaction constant.

Because the electron moves with near the speed of light c,  $\Delta E_{\ell,s}$  has to be calculated using the theory of special relativity. This is the reason for an additional relativistic energy correction

$$\Delta E_r = -E_n \frac{\alpha^2}{n^2} \left( \frac{3}{4} - \frac{n}{\ell + \frac{1}{2}} \right) \quad \text{with} \quad \alpha = \frac{e^2}{4\pi \cdot \epsilon_0 \cdot \hbar \cdot c} , \quad (2.17)$$

where  $\alpha \approx \frac{1}{137}$  is the fine-structure constant, c the speed of light in vacuum and  $\epsilon_0$  is the dielectric constant.

Due to the uncertainty principle [16], the position of the electron can only be given in a range of the Compton-length  $\lambda_C = \frac{\hbar}{m_e \cdot c}$ . The electron in the electric field of the nucleus is now affected by the field inside the volume  $\lambda_C^3$ , which is taken into account by adding the so called Darwin-term. In total, the energy splitting of the fine structure  $E_{n,j}$  is given by

$$\Delta E_{n,j} = \left[ 1 + \frac{\alpha^2}{n} \left( \frac{1}{j + \frac{1}{2}} - \frac{3}{4n} \right) \right] . \tag{2.18}$$

#### 2.1.5 Hyperfine Structure

Similar to the fine splitting, an even finer, the so-called hyperfine splitting, was discovered. As mentioned in subsection 2.1.3, every particle posses a spin. As a result, an atomic nucleus possesses a nuclear spin  $\vec{I}$ , that is defined by the spins of the nucleons. Nuclei consist of protons and neutrons, which are both fermions, possessing a spin of  $\frac{1}{2}$ . Since the nucleus of hydrogen only consists of one proton, the nuclear spin of hydrogen  $\vec{I}$  is  $\frac{1}{2}$  as well. This nuclear spin creates a nuclear magnetic moment  $\mu_I$  with

$$\vec{\mu_I} = -g_I \frac{\mu_n}{\hbar} \vec{I} \quad \text{with} \quad \mu_n = \frac{e \cdot \hbar}{2m_P} ,$$
(2.19)

where  $g_I$  is the nuclear-g-factor <sup>4</sup>,  $\mu_n$  is the core-magneton and  $m_P$  is the mass of the proton. Due to the mass ratio  $\frac{m_p}{m_e} \approx 1836$ , the magnetic moment created by the

 $<sup>^{4}</sup>g_{I} = 5.585694702(17)[21]$ 

proton spin is by about three orders of magnitude smaller than that of the electron.

Similar to the fine structure splitting, the magnetic moment of the total angular momentum of the electron and the nuclear magnetic moment interact with one another, resulting in the hyperfine structure. The total angular momentum of the electron and the nuclear spin combine to the total angular momentum of the atom  $\vec{F}$ , with

$$|\vec{J} - \vec{I}| \le |\vec{F}| \le |\vec{J} + \vec{I}| \ .$$
 (2.20)

The resulting energy splitting  $\Delta E_{HFS}$  can be calculated to

$$\Delta E_{HFS} = \frac{\Delta E_{HFS,0}(n\ell_j)}{2} [F(F+1) - J(J+1) - I(I+1)] , \qquad (2.21)$$

where  $\Delta E_{HFS,0}(n\ell_i)^{5}$  is the hyperfine structure constant, which is state dependent.

Therefore, the hyperfine structure splits the ground state  $(1S_{1/2})$  of hydrogen into four substates. A triplet state with F=1 and a singlet state with F=0, which are energetically separated by  $E_{HFS,0}(n\ell_j)$ . The quantum mechanical description of the four hyperfine states are

$$\alpha_1$$
:  $|F = 1, m_F = +1\rangle = |m_j = +\frac{1}{2}, m_I = +\frac{1}{2}\rangle$  (2.22a)

$$\alpha_2$$
:  $|1,0\rangle = \frac{1}{\sqrt{2}} \left[ \sqrt{1+a} \mid +\frac{1}{2}, -\frac{1}{2}\rangle + \sqrt{1-a} \mid -\frac{1}{2}, +\frac{1}{2}\rangle \right]$  (2.22b)

$$\beta_3$$
:  $|1, -1\rangle = |-\frac{1}{2}, -\frac{1}{2}\rangle$  (2.22c)

$$\beta_4$$
:  $|0,0\rangle = \frac{1}{\sqrt{2}} \left[ \sqrt{1-a} \mid +\frac{1}{2}, -\frac{1}{2} \rangle - \sqrt{1+a} \mid -\frac{1}{2}, +\frac{1}{2} \rangle \right] ,$  (2.22d)

with

$$a = \frac{\frac{B}{B_c}}{\sqrt{1 + \left(\frac{B}{B_c}\right)^2}} \quad \text{with} \quad B_c \approx \frac{\Delta E_{HFS,0}(n\ell_j)}{2\mu_B} , \qquad (2.23)$$

where  $B_c$  <sup>6</sup> is the critical magnetic field strength. The spin orientations for the states  $|2\rangle$  and  $|4\rangle$  have a dependency on an external magnetic field, whereas for  $|1\rangle$  and,  $|3\rangle$  the orientation is independent of an external magnetic field.

#### 2.1.6 Lamb-shift

In 1937, by multiple research groups [23, 24, 25] another splitting in the spectrum of hydrogen was discovered, which could not be explained by the interaction of the various magnetic moments. In 1947, Willis E. Lamb and Robert C. Retherford [26] were able to precisely measure this splitting, by measuring the energy levels of the temporal

 $<sup>{}^5</sup>n\ell_j$  is the standard notation of the electron orbit., e.g.  $2S_{\frac{1}{2}}$  stands for an electron with n=2,  $\ell=0$  and  $j=\frac{1}{2}$ .

<sup>&</sup>lt;sup>6</sup>For the S states of hydrogen  $B_c = 50.7 \,\mathrm{mT}$  [4].

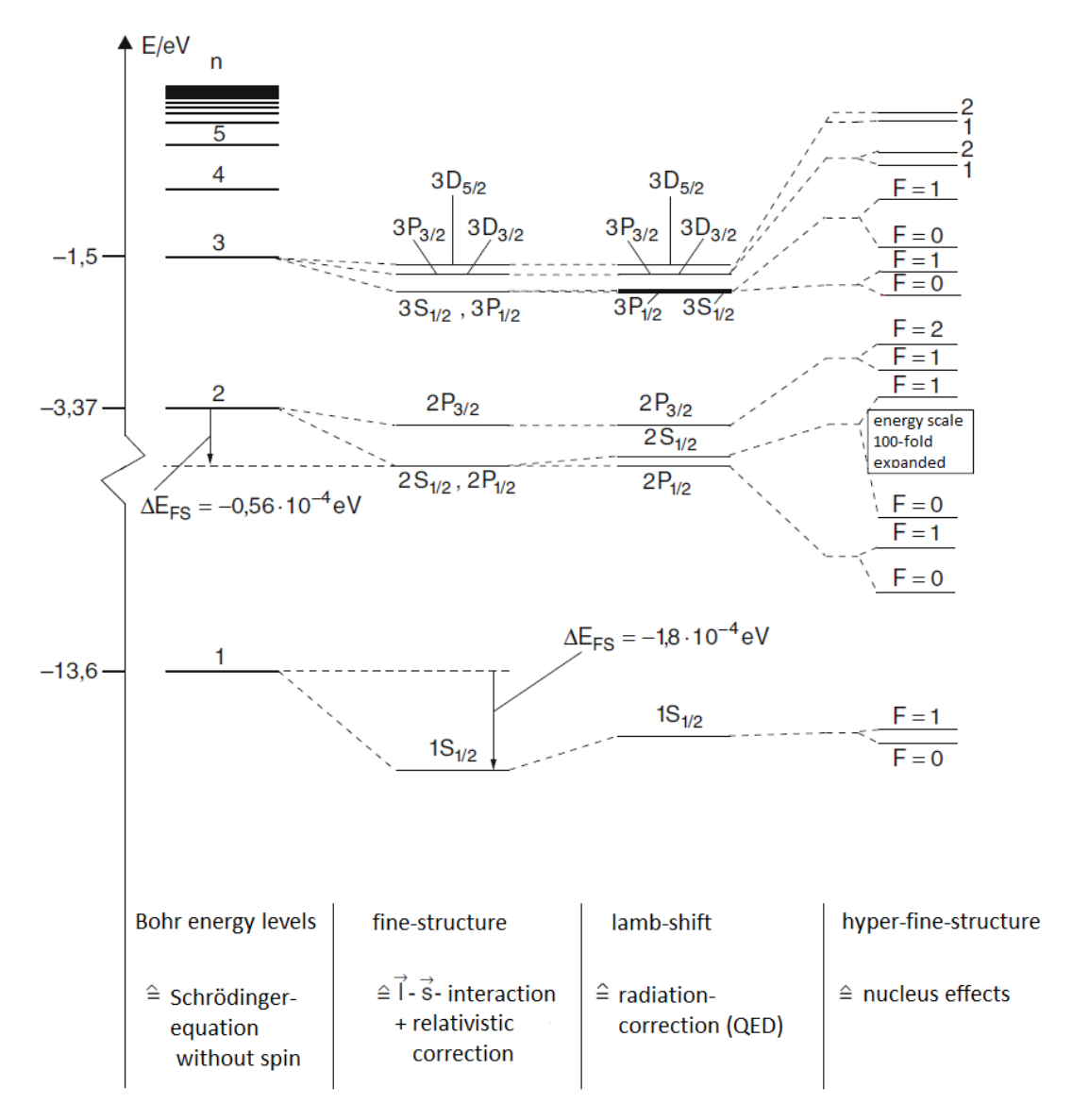


FIGURE 2.2: Term scheme of the hydrogen atom [28]. (Modified from source)

means to the  $2P_{1/2}$  states of hydrogen and deuterium. For hydrogen, they found that the  $2S_{1/2}$  state has a  $4.4 \times 10^{-6}$  eV lower binding energy than the  $2P_{1/2}$  state.

This was explained in 1948 by Richard Feynman [27] in the framework of quantum electrodynamics (QED). Most of the phenomenon can be explained due to effects like vacuum fluctuations. In agreement with the uncertainty principle, for a short period of time  $\Delta t < \frac{h}{\Delta E} = \frac{1}{f}$ , an electron can absorb or emit a photon with the energy  $\Delta E = h \cdot f$  without changing its state. This causes a trembling movement of the electron, weakening the temporal means of the atomic potential. Because electrons on a lower shell are closer to the nucleus, electrons with  $\ell > 0$  are less influenced by this effect. Therefore, the  $2S_{1/2}$  state is slightly less bound than the  $2P_{1/2}$  state. A term scheme of the hydrogen atom can be found in Figure 2.2.

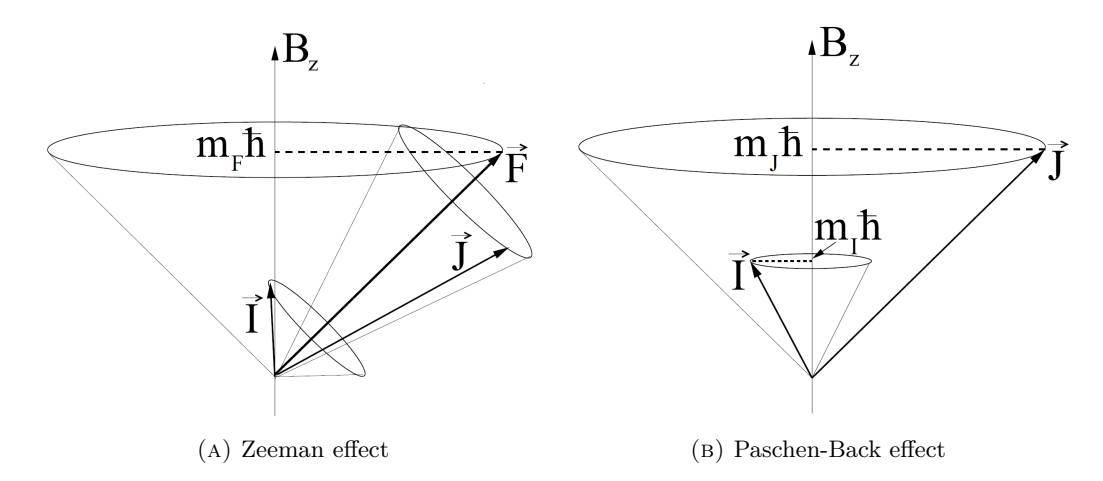


FIGURE 2.3: A: Diagram to illustrate the Zeeman effect of the hyperfine splitting.  $\vec{J}$  and  $\vec{I}$  combine to  $\vec{F}$ , which precesses around  $B_z$ . B: Diagram to illustrate the Paschen-Back effect of the hyperfine splitting. The  $\vec{J}$ - $\vec{I}$  coupling is broken and they both precess around  $B_z$ .

#### 2.1.7 Zeeman and Paschen-Back Effect of the Hyperfine Structure

As discussed in subsection 2.1.5, the total angular momentum of the electron  $\vec{J}$  and the nuclear spin  $\vec{I}$  couple to the total angular momentum of the atom  $\vec{F}$ . In a weak external magnetic field  $B_{ext}$ , with  $B_{ext} < B_c$ , the coupling is preserved, however,  $\vec{F}$  precesses around the magnetic field direction  $B_z$ , see Figure 2.3a. In this case, the total magnetic moment of the atom  $\mu_F$  is defined by the sum of the total magnetic moment of the electron  $\mu_J$  and the magnetic moment of the nuclear spin  $\mu_I$ , with respect to the quantization axis (z),  $\mu_F$  is given by

$$\langle \mu_F \rangle_z = \langle \mu_J \rangle_z + \langle \mu_I \rangle_z = -g_F \cdot \mu_B \cdot m_F , \qquad (2.24)$$

where  $g_F$  is the g factor of the total angular momentum, with

$$g_F = g_j \frac{F(F+1) + J(J+1) - I(I+1)}{2F(F+1)} - g_I \frac{\mu_I}{\mu_B} \frac{F(F+1) + I(I+1) - J(J+1)}{2F(F+1)},$$
(2.25)

where  $g_j$  is the g-factor for the total angular momentum of the electron. Due to the dependency on  $m_F$  the magnetic field now removes the degeneration of the hyperfine states with F > 0. The resulting energy correction is given by

$$\Delta E_{HFS,weak}(B_z) = \langle \vec{\mu_F} \rangle_z \cdot B = -m_F \cdot g_F \cdot \mu_B \cdot B_z . \qquad (2.26)$$

Therefore, for hydrogen, the mixed states with antiparallel spins ( $|2\rangle$  and  $|4\rangle$ ) do not have to be corrected, while the other two states with parallel spin ( $|1\rangle$  and  $|3\rangle$ ) do. The effect is named after Pieter Zeeman [29], who first observed it in 1896.

In a strong external magnetic field, with  $B_{ext} > B_c$ , the coupling of  $\vec{J}$  and  $\vec{I}$  is broken, and both precess around the magnetic field direction  $B_z$ , see Figure 2.3b. This is called the Paschen-Back effect, named after Friedrich Paschen and Ernst

Back [30], who discovered it in 1921. The magnetic moments of  $\vec{J}$  and  $\vec{I}$  now contribute individually. The resulting energy correction can be written as

$$\Delta E_{HFS,strong}(B_z) = g_J \cdot \mu_B \cdot m_J \cdot B_z + \Delta E_{HFS,0}(n\ell_i) \cdot m_J \cdot m_I - g_I \cdot \mu_n \cdot m_I \cdot B_z , \quad (2.27)$$

where the first term is the contribution of the electrons in the atomic shell, the second term is the hyperfine interaction between  $\vec{J}$  and  $\vec{I}$ , and the third term is the contribution of the nucleus, which is about three orders of magnitude smaller than that of the electrons.

#### 2.1.8 Stark Effect and the Metastable $2S_{1/2}$ State

Like magnetic fields, external electric fields  $\vec{E}$  also influence the atomic binding energy, very similar to the Zeeman effect. However, it does not remove the degeneracy of an atomic level, i.e., that states with the same value of the magnetic quantum number of the total angular momentum are still degenerate. The effect was discovered in 1913 by Johannes Stark [31]. One distinguishes between the linear and the quadratic Stark effect, where the modification of the atomic binding energy due to the external electric field is proportional to  $|\vec{E}|$  or  $|\vec{E}^2|$ . The linear stark effect is observed in hydrogenlike atoms in states with principal quantum number n > 1. For all other atoms, the quadratic Stark effect applies.

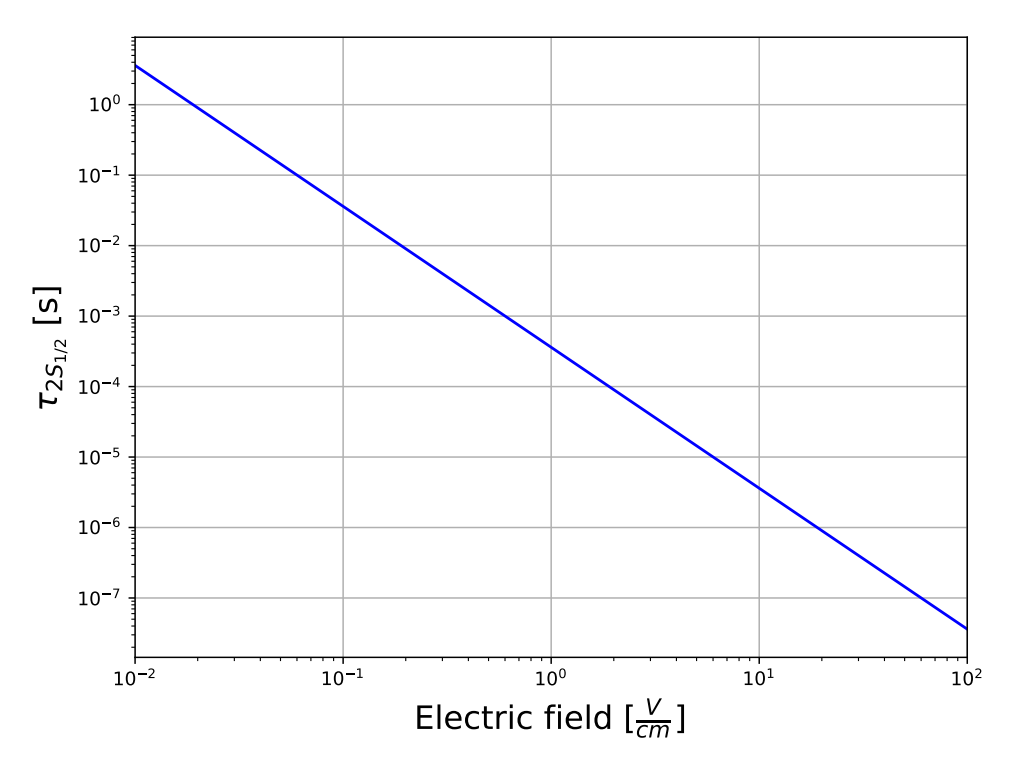


Figure 2.4: Lifetime of the  $2S_{1/2}$ -state as function of an external electric field.

Furthermore, the linear Stark effect has an influence on the lifetime  $\tau$  of the  $2S_{1/2}$  state. Without electric fields, due to the conservation of angular momentum, the  $2S_{1/2}$  state can only transition into the ground state via a multi-photon transition, therefore becoming a metastable state with a relative long lifetime of  $\tau_{2S_{1/2}}\approx 0.14\,\mathrm{s}$ . Inside electric fields, however, the Stark effect now creates a mixing between the  $2S_{1/2}$  state with the short-lived  $2P_{1/2}$  state ( $10^{-7}\mathrm{s} < \tau_{2P_{1/2}}$ ). As a result, the lifetime of the  $2S_{1/2}$  state decreases with the increase of an external electric field. The  $\tau_{2S_{1/2}}$  as function of an external electric field is plotted in Figure 2.4.

#### 2.1.9 Polarization

As discussed in subsection 2.1.2, the angular momentum l of a particle has 2l + 1 possible orientations. In an external magnetic field  $\vec{B} = B_z e_z$ , the expectation value of  $\hat{L}_z$  is

$$\langle \hat{L}_z \rangle = \langle l, m_l | \hat{L}_z | l, m_l \rangle = \hbar m_l . \tag{2.28}$$

For an ensemble of particles of angular momentum l, the particles can occupy different values of  $m_l$ . This can be described by the density operator  $\hat{\rho}$ . It is given by

$$\widehat{\rho} = \sum_{i=1}^{n} P_i |\psi_i\rangle\langle\psi_i| , \qquad (2.29)$$

with  $P_i$  being the probability of a particle to be in the *i*th state  $(|\psi_i\rangle)$  in the ensemble with n different states. Obviously, the sum over all probabilities equals 1. The expectation value of  $\hat{L}_z$  is the polarization vector  $\vec{P} = p_i$ , with

$$p_{i} = \frac{1}{\hbar l} \langle \hat{L}_{i} \rangle = \frac{1}{\hbar l} tr(\hat{\rho} \hat{L}_{z}) = tr\left(\sum_{i=1}^{2l+1} P_{i} |l, m_{l}\rangle \langle l, m_{l}| \hat{L}_{z}\right)$$
(2.30)

As consequence of Equation 2.4, the components  $p_i$  cannot be measured simultaneously, and, because we choose z as quantization axis, only  $p_z$  is of further interest. It is commonly called the vector polarization.

For a l=1/2 particle, one gets

$$|1/2, +1/2\rangle = |\uparrow\rangle = \begin{pmatrix} 1\\0 \end{pmatrix} \qquad |1/2, -1/2\rangle = |\downarrow\rangle = \begin{pmatrix} 0\\1 \end{pmatrix} , \qquad (2.31)$$

the z- component of the angular momentum operator is

$$\hat{L}_z = \frac{\hbar}{2} \sigma_z \ , \tag{2.32}$$

with  $\sigma_z$  being the third Pauli matrix. The density operator becomes

$$\widehat{\rho} = \sum_{i=1}^{n} P_i |\psi_i\rangle\langle\psi_i| = \begin{pmatrix} P_{\uparrow} & 0\\ 0 & P_{\downarrow} \end{pmatrix} , \qquad (2.33)$$

where  $P_{\uparrow}$  and  $P_{\downarrow}$  are the probabilities of a particle to be in the state  $|\uparrow\rangle$  or  $|\downarrow\rangle$ , respectively. The vector polarization results to

$$p_z = \frac{2}{\hbar} tr\left(\widehat{\rho}\widehat{L}_z\right) = tr\left(\widehat{\rho}\widehat{L}_z\right) = P_{\uparrow} - P_{\downarrow} . \tag{2.34}$$

An alternate way to describe  $p_z$  using the occupation numbers  $N_{\uparrow}$  and  $N_{\downarrow}$  is

$$p_z = \frac{N_{\uparrow} - N_{\downarrow}}{N_{\uparrow} + N_{\downarrow}} \ . \tag{2.35}$$

The vector polarization is fully sufficient to describe the polarization of an ensemble of l=1/2 particles. For l=1 particles like deuterium, to describe the complete polarization, additionally the tensor polarization  $p_{zz}$  needs to be calculated.

#### 2.2 Breit Rabi Formula

The formulas given in the subsection 2.1.7 only allow the modification of the energy correction caused by external magnetic fields that are either strong or weak compared to the critical magnetic field of the atoms, and do not give a sufficiently accurate solution for mean magnetic fields with  $B_{ext} \approx B_c$ .

An alternative to describe the energy correction of the binding for all magnetic fields is the Breit-Rabi forumla, published in 1931 by Isidor Isaac Rabi and Gregory Breit [9]. The formula gives an over all solution for the binding energy in atoms with  $F = I \pm 1/2$ , which also holds for fields around  $B_{ext} \approx B_c$ . In the following subsections, the original Breit-Rabi formula for the hydrogen atom is presented, as well as a modified version with various corrections from quantum electrodynamics that were not known to Breit and Rabi at the time of the original publication.

#### 2.2.1 The Breit-Rabi Formula for Hydrogen

By solving the eigenvalue problem of the hyperfine Hamilton operator in a magnetic field  $\vec{B} = B_z \vec{e}_z$  for the  $1S_{1/2}$  state of hydrogen, one gets the solutions for the modification of the binding energy for the four hyperfine substates. The Hamilton operator  $\hat{H}_{HFS}$  is given by

$$\widehat{H}_{HFS} = \Delta E_{HFS,0}^{7} \frac{\widehat{I} \cdot \widehat{J}}{\hbar^{2}} + \left( g_{j} \mu_{B} \frac{\widehat{J}_{z}}{\hbar} - g_{I} \mu_{B} \frac{\widehat{I}_{z}}{\hbar} \right) B , \qquad (2.36)$$

<sup>&</sup>lt;sup>7</sup>Here and in the following  $\Delta E_{HFS,0}$  is an abbreviated form for  $\Delta E_{HFS,0}(1S_{1/2})$  the hyperfine constant for the  $(1S_{1/2})$  state, which has been shortened for better readability.

the value for  $\Delta E_{HFS,0}(1S_{1/2})$  is  $5.87\times 10^{-6}$  eV, and the four solutions for the substates are

$$\delta E_{\alpha_1}(B_z) = \frac{\Delta E_{HFS,0}}{4} - \frac{g_s \mu_B B_z}{2} - \frac{g_I \mu_n B_z}{2}$$
 (2.37a)

$$\delta E_{\alpha_2}(B_z) = -\frac{\Delta E_{HFS,0}}{4} + \frac{1}{2} \sqrt{\Delta E_{HFS,0}^2 + (g_s \mu_B - g_I \mu_n)^2 B_z^2}$$
 (2.37b)

$$\delta E_{\beta 3}(B_z) = \frac{\Delta E_{HFS,0}}{4} + \frac{g_s \mu_B B_z}{2} + \frac{g_I \mu_n B_z}{2}$$
 (2.37c)

$$\delta E_{\beta 4}(B_z) = -\frac{\Delta E_{HFS,0}}{4} - \frac{1}{2} \sqrt{\Delta E_{HFS,0}^2 + (g_s \mu_B - g_I \mu_n)^2 B_z^2} . \tag{2.37d}$$

This is in agreement with the conventional Breit-Rabi formula[9] that can be written as

$$\delta E_{HFS,mag}(x) = \Delta E_{HFS,0} \left[ -a_1 m_F x \pm \frac{1}{2} \sqrt{1 + \frac{2m_F}{I + \frac{1}{2}} c_1 x + c_2 x^2} \right] - \frac{\Delta E_{HFS,0}}{2(2I+1)} ,$$
(2.38)

where

$$x(B_z) = \frac{\mu_B B_z}{\Delta E_{HFS,0}} = \frac{B_z}{B_c^8} \ . \tag{2.39}$$

The energies  $\delta E$  are counted from the hyperfine centroid. In Figure 2.5 the Breit-Rabi diagram for the  $1S_{1/2}$  state of hydrogen is shown.

Compared to the original notation of Breit and Rabi [9], the coefficients in Equation 2.38 are modified to allow a better comparison with Equation 2.37 and to allow a better understanding of the corrections that are presented in the following subsection. The coefficients are

$$a_1 = -g_I \mu_n \tag{2.40a}$$

$$c_1 = g_s \mu_B + g_I \mu_n \tag{2.40b}$$

$$c_2 = (g_s \mu_B + g_I \mu_n)^2 . (2.40c)$$

# 2.2.2 The Breit-Rabi Formula for Hydrogen including QED Corrections

Since the days of Breit and Rabi, the understanding of the hydrogen spectrum has drastically improved. D. L. Moskovkin and V. M. Shabaev [32] have calculated an improved and more accurate version of the Breit-Rabi formula that incorporates various corrections from quantum electrodynamics. Based on [32] the Breit Rabi formula for the  $1S_{1/2}$  state can be written as

 $<sup>^8</sup>B_c$  is again the critical magnetic field for hydrogen atoms, see subsection 2.1.5. For the  $2S_{1/2}$  state of hydrogen  $B_c=50.7\,\mathrm{mT}$  [4].

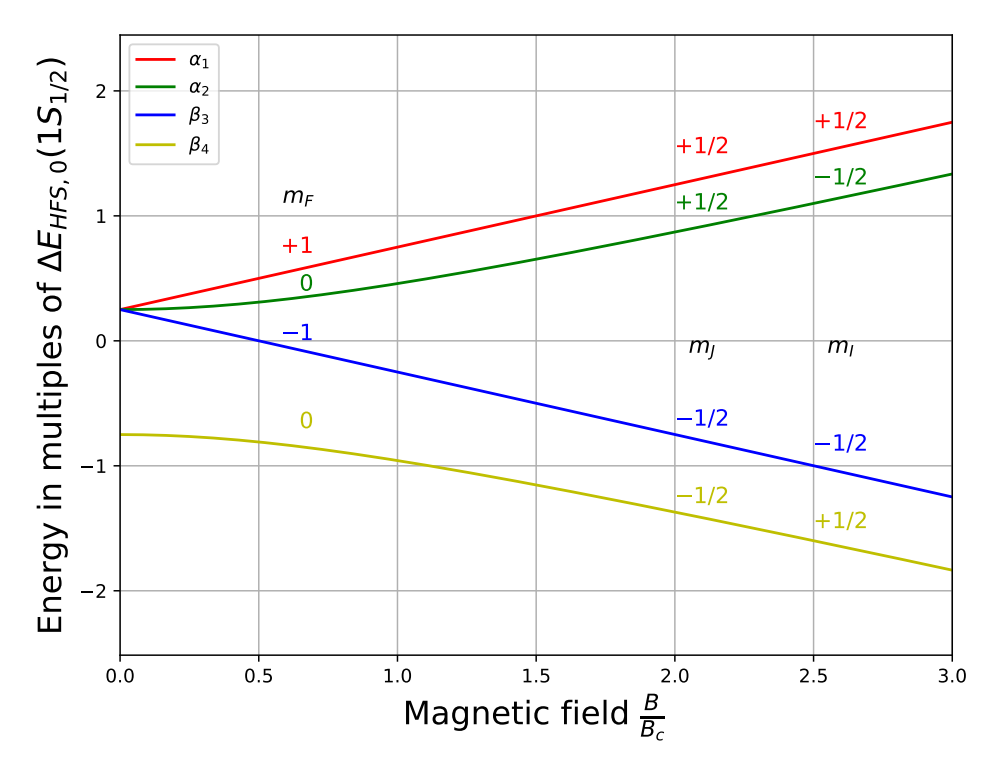


FIGURE 2.5: Breit-Rabi diagram of the  $1S_{1/2}$  state of hydrogen. The magnetic field B is given in multiples of  $B_c$ , the energy in multiples of  $E_{HFS,0}$ . The basis of the calculation is Equation 2.37.

$$\delta E_{HFS,mag}(x) = \Delta E_{HFS,0} \left[ -\alpha_1 (1 + \epsilon_1) m_F x + \epsilon_2 \frac{\Delta E_{HFS,0}}{m_e c^2} x^2 \right]$$

$$\pm \frac{1}{2} \sqrt{1 + \frac{2m_F}{I + \frac{1}{2}} c_1 (1 + \delta_1) x + c_2 (1 + \delta_2 + m_F^2 \delta_3) x^2} - \frac{\Delta E_{HFS,0}}{2(2I + 1)} .$$
(2.41)

The "-" and "+" correspond to the lower and higher values of F with same  $m_F$ , respectively. Following [32], the corrections of the binding energies of the four substates are

$$\delta E_{\alpha_1,QED}(x) = \Delta E_{HFS,0} \left[ \frac{1}{2} + d_1(1+\eta_1)x + \eta_2 \frac{\Delta E_{HFS,0}}{m_e c^2} x^2 \right]$$
 (2.42a)

$$\delta E_{\alpha_2,QED}(x) = \Delta E_{HFS,0} \left[ \epsilon_2 \frac{\Delta E_{HFS,0}}{m_e c^2} x^2 + \frac{1}{2} \sqrt{1 + c_2 (1 + \delta_2 + m_F^2) x^2} \right]$$
(2.42b)

$$\delta E_{\beta 3,QED}(x) = \Delta E_{HFS,0} \left[ \frac{1}{2} - d_1(1 + \eta_1)x + \eta_2 \frac{\Delta E_{HFS,0}}{m_e c^2} x^2 \right]$$
 (2.42c)

$$\delta E_{\beta 4,QED}(x) = \Delta E_{HFS,0} \left[ \epsilon_2 \frac{\Delta E_{HFS,0}}{m_e c^2} x^2 + \frac{1}{2} \sqrt{1 + c_2 (1 + \delta_2 + m_F^2) x^2} \right] . \quad (2.42d)$$

The coefficients  $\epsilon_1$ ,  $\epsilon_2$ ,  $\delta_1$ ,  $\delta_2$ ,  $\delta_3$ ,  $\eta_1$ ,  $\eta_2$ , and  $d_1$  were numerical calculated and can be found in Appendix A.

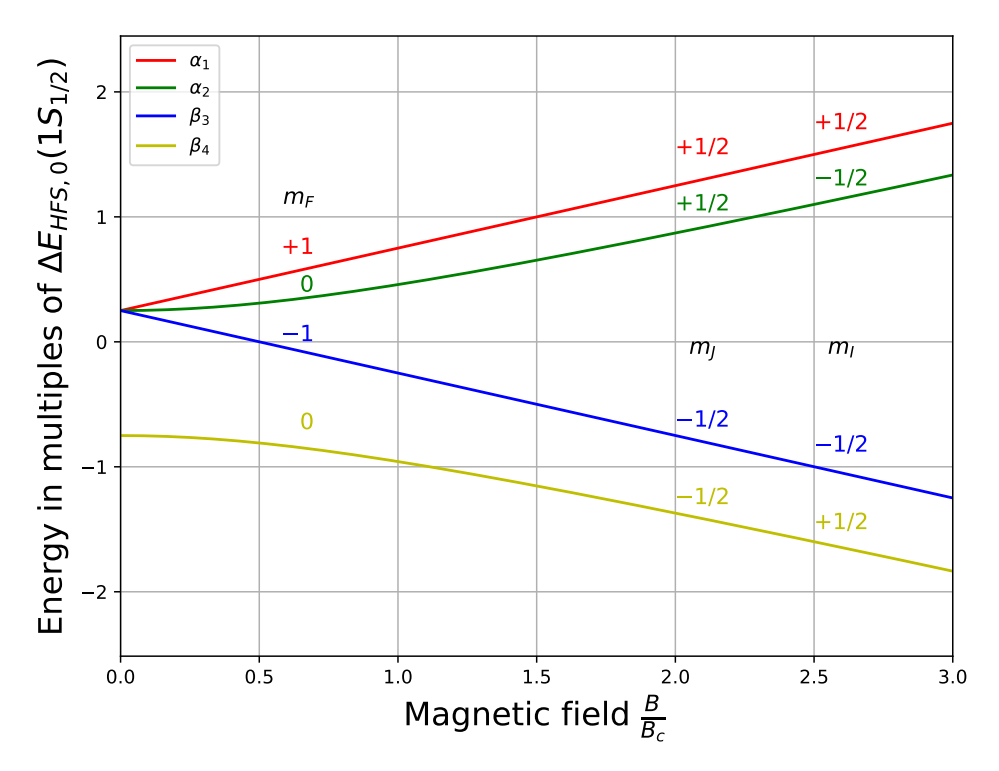


FIGURE 2.6: Breit-Rabi diagram of the  $1S_{1/2}$ -state of hydrogen, including QED-correction. The magnetic field B is given in multiples of  $B_c$ , the energy in multiples of  $E_{HFS,0}$ .

In Figure 2.6 the Breit-Rabi diagram for the  $1S_{1/2}$  state of hydrogen including the QED corrections is shown. The difference between Figure 2.5 and Figure 2.6 are just in the order of 0.002%  $\Delta E_{HFS,0}(1S_{1/2})$ . To get a better idea of the order, in Figure 2.7, the difference  $(\delta E_{HFS} - \delta E_{HFS,QED})$  is plotted for the first few  $B_c$ . One can see that the differences between the formula with QED corrections and without are very small. In the measurements presented in this thesis, only magnetic fields in the range below 1  $B_c$  are achieved. Here, the difference is in the order of below 0.01 neV. So in order to verify the QED corrections, the measurement uncertainties need to fall below this value.

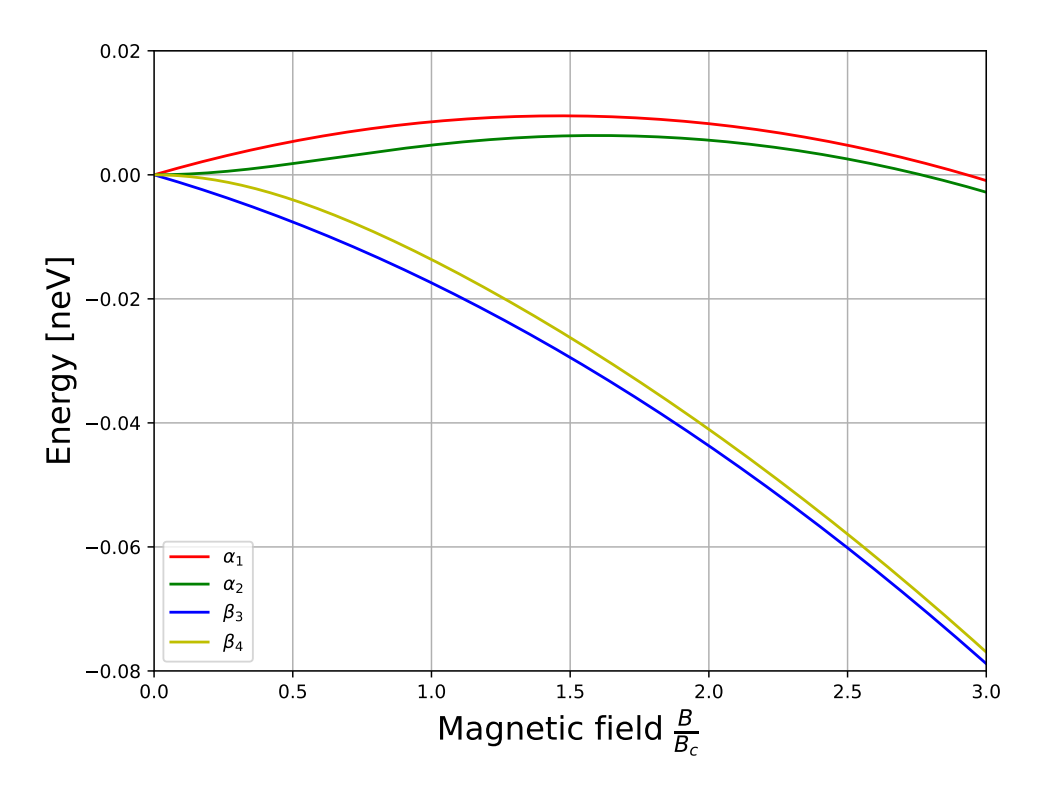


FIGURE 2.7: Difference between the conventional Breit-Rabi formula and the version that includes QED corrections. The magnetic field B is given in multiples of  $B_c$ .

#### 2.3 Lamb-Shift Polarimeter

The Lamb-shift polarimeters is a device designed to measure the nuclear spin polarization of hydrogen and/or deuterium atoms, ions and molecules or its isotopes by using the properties of the metastable  $2S_{1/2}$  state. In general, a Lamb-shift polarimeter consists of five main components, which are an ionizer/ion source, a Wienfilter, a cesium cell, a spin filter and a quenching chamber. In case of an ionizer, it is used to ionize an incoming beam of neutral particles. In case of an ion source, it directly creates a beam of ionized particles. The ions are accelerated towards the Wienfilter, which separates them according to their masses, so that only a single mass is transmitted. From there, the beam travels into the cesium cell, where the ions are transformed into metastable neutral atoms via a charge transfer reaction. After that they enter the spin filter, in where, the metastable atoms are quenched to the ground state except for one of the  $\alpha$ states. The remaining meta stable atoms are quenched to the ground state inside the quenching chamber. There, the Lyman- $\alpha$  photons emitted in the quenching process are detected by a photomultiplier tube. At the end of the quenching chamber, also a Faraday cup is mounted allowing to directly measure the current of the ion beam. Longitudinal magnetic fields in the ionizer, the Cesium cell and the spin filter, as well as a perpendicular magnetic field in the Wienfilter ensure a well-defined quantization axis along the polarimeter. A schematic drawing of the Lamb-shift polarimeter can be seen in Figure 2.8.

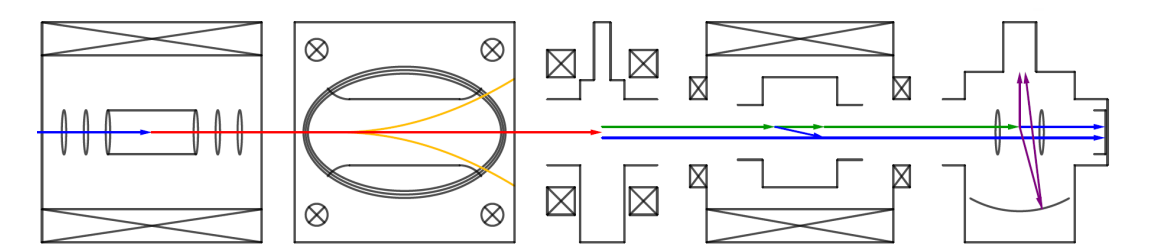


FIGURE 2.8: Schematic of the Lamb-shift polarimeter. Blue vectors indicate beams of neutral particles in the ground state. The red vector indicates the ion beam formed in the ionizer, consisting of ions of different masses. Ions of undesired masses (marked in yellow) are deflected in the Wienfilter. Metastable atoms are denoted in green. In the spin filter they are brought to the ground state and only one  $\alpha$ -state is allowed to pass. In the quenching chamber, all remaining metastable atoms are quenched to the ground state, whereas Lyman- $\alpha$  photons (marked in violet) are emitted, which are detected by a photomultiplier tube [18].

#### 2.3.1 Ionizer

Different types of ionizers are suitable to be used in a Lamb shift polarimeter. One possibility to create an ionized particle beam is electron impact ionization, using an electron gun, which for example can be used to create an ionized and polarized beam

out of a storage cell [5], or a Glavish-type ionizer which can be used to create a polarized HD-beam [6].

Another possibility is an electron-cyclotron-resonance (ECR) ion source, which is used in the experiments later described in this thesis. An electron cyclotron resonance occurs when an electron, located inside a static magnetic field  $B_{stat}$ , is irradiated with an electromagnetic frequency  $f_{HF}$  corresponding to the natural frequency of the electron's rotation within the magnetic field. Due to the Lorentz force in the magnetic field, a free electron will start to move on a closed trajectory. The angular frequency  $\omega_{cr}$  of the motion is

$$\omega_{cr} = 2\pi f_{HF} = \frac{eB_{stat}}{m_e \gamma} \quad \text{with} \quad \gamma = \frac{1}{\sqrt{1 - (\frac{v}{c})}}.$$
(2.43)

Inside an ECR-source  $B_{stat}$  is designed in a way that allows electrons to find a stable orbit. Commonly used conditions for ECR sources are  $B_{stat} = 87.5 \,\mathrm{mT}$  and  $f_{HF} = 2.45 \,\mathrm{GHz}$ . The electrons trapped in the ECR collide with molecular gas injected into the source to produce ions. The ions are then extracted using static electric potentials.

#### 2.3.2 Wienfilter

The Wienfilter is named after its developer Wilhelm Wien, who invented it in 1898 [33]. The electric  $\vec{F}_E$  and the Lorentz force  $\vec{F}_L$  are acting on a particle, carrying the charge q, and traveling though an electrical  $\vec{E}$  and magnetic field  $\vec{B}$  with the velocity  $\vec{v} = v_z \vec{e}_z$ . The total force acting on this particle is

$$\vec{F} = \vec{F}_E + \vec{F}_L = q \cdot \vec{E} + q \cdot \vec{v} \cdot \vec{B} . \qquad (2.44)$$

By arranging the flight direction of the particle perpendicular to both fields  $(z \perp \vec{B} \perp \vec{E} \perp z)$  a particle will not experience a force if

$$|v| = \frac{E}{B} \,, \tag{2.45}$$

with  $E = |\vec{E}|$  and  $B = |\vec{B}|$ . Therefore, particles with the same velocity can path the Wienfilter undisturbed, while all others will be deflected and can be stopped by a collimator.

For mono-energetic beams, where all particles have the same kinetic energy  $E_{kin}$ , the aperture becomes a mass filter, since

$$m = \frac{2E_{kin}}{v^2} = 2E_{kin}\frac{B^2}{E^2} \ . \tag{2.46}$$

In polarization experiments one also needs to consider that the magnetic moments of the particles will start to precess around the perpendicular magnetic field of the Wienfilter with the Lamor frequency

$$\omega_L = -\gamma B , \qquad (2.47)$$

where  $\gamma$  is the gyromagnetic ratio of the particle. The total angle  $\alpha$  of the rotation is defined by the time of flight  $\Delta t$  through the Wienfilter and the Larmor frequency, with

$$\alpha = \Delta t \cdot \omega_L = -\gamma \sqrt{\frac{m}{2E_{kin}}} \cdot B \cdot l , \qquad (2.48)$$

where l is the effective length of the magnetic field. For a proton beam it needs to be taken into account that in the absence of an electron, the nuclear magnetic moment will rotate and so change the polarization, because the LSP can measure the projection on the beam line only. Therefore, B and l need to be chosen carefully to compensate this. For molecular ions, this effect can be neglected, because the magnetic moment of the unpaired electron inside a molecule will realign with the magnetic field of the Wienfilter adiabatically and the nuclear magnetic moment is strongly coupled to that of the electron.

#### 2.3.3 Cesium Cell

Inside the cesium cell, metastable atoms  $(H_{2S_{1/2}} \text{ or } D_{2S_{1/2}})$  are produced using a charge-exchange reaction. The incoming beam reacts with cesium inside the cell. The cesium is heated so that it appears as saturated vapor with a temperature of around 100 °C. In case of an atomic beam, the H<sup>+</sup> or D<sup>+</sup> ions capture an electron from a cesium atom, which can be described as a "nearly resonant process" [34]. The equation of the reaction is

$$H^+ + Cs \to H^* + Cs^+$$
 (2.49)

Not all reactions result in the  $2S_{1/2}$ -state, the ground state as well as other excited radiative states are possible too. Figure 2.9 shows the cross-section of the charge transfer reaction. One can see that it reaches its maximum at 550 eV per nucleon. For the production of  $2S_{1/2}$  hydrogen, this corresponds to an efficiency of around 30%.

Measurements have shown, that the production of metastable atoms from a molecular ion beam is also possible [5, 6]. However, it is not yet resolved how exactly the metastable atoms are created. It is either a two steps process, which could look like this

$$H_2^+ + Cs \to 2H^+ + Cs^+ + 2e^-$$
 and then (2.50)

$$H^+ + Cs \to H_{2S_{1/2}} + Cs^+$$
, (2.51)

or they are produced directly, in a reaction like this

$$H_2^+ + Cs \to H_{1S_{1/2}} + H_{2S_{1/2}} + Cs^+$$
 (2.52)

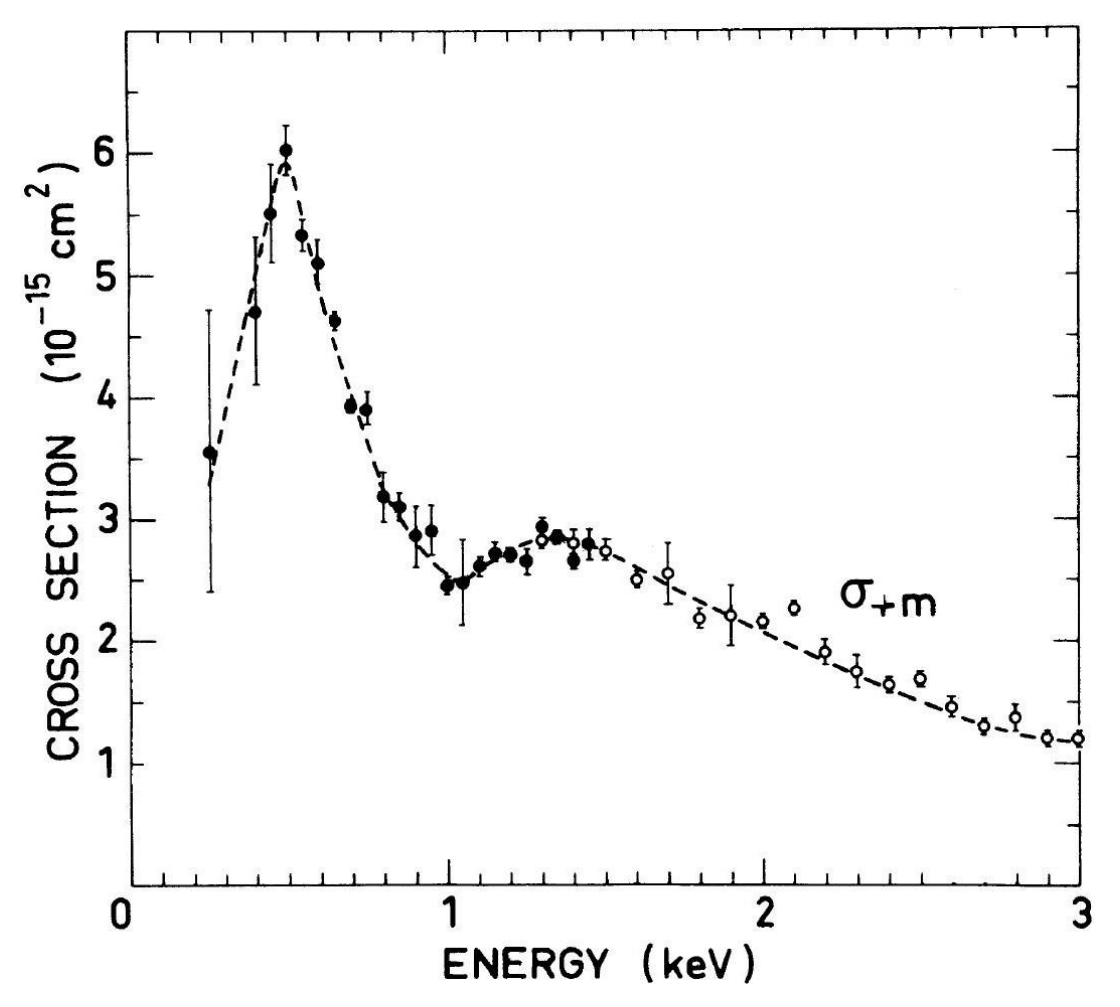


FIGURE 2.9: Cross-section of charge transfer reactions (•)  $Cs + D^+ \rightarrow D_{2S_{1/2}} + Cs^+$ , and (o)  $Cs + H^+ \rightarrow H_{2S_{1/2}} + Cs^+$  as function of the energy per nucleon [34].

Recent investigations by Lukas Huxold [18] have shown that the temperature of the Caesium vapor also has an effect on the efficiency of the  $2S_{1/2}$  formation process. It seems that a hotter Caesium vapor is beneficial, which would be a hint that the 2-step process is more likely.

#### 2.3.4 Spin Filter

The spin filter is the part of the LSP that filters for the different hyperfine substates. It was developed by McKibben, Lawrence, and Ohlsen [35] as part of a Lamb-shift ion source in 1968. It uses a combination of electric and magnetic fields and an injected radiofrequency to quench all metastable particles traveling through it to the  $2S_{1/2}$  state. By choosing the right amplitude of the fields and radiofrequency, all but one hyperfine substate are quenched to the ground state while passing through the spin filter.

As discussed in subsection 2.1.6 the  $2S_{1/2}$  state and the  $2P_{1/2}$  state are separated by 4.375  $\mu$ eV [36], the Lamb-shift. Similar to the  $1S_{1/2}$  state, the hyperfine substates of  $2S_{1/2}$  are named  $\alpha$  and  $\beta$  (see subsection 2.1.5). The hyperfine substates of the

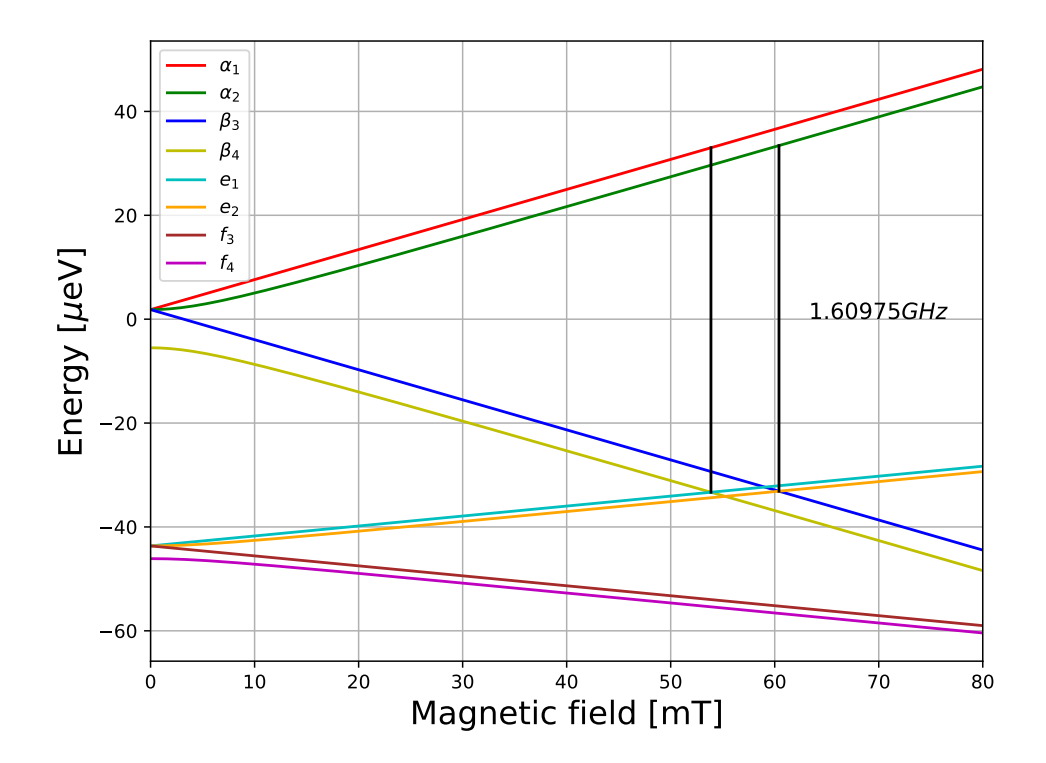


FIGURE 2.10: Breit-Rabi diagram of the  $2S_{1/2}$  and  $2P_{1/2}$  state. At  $B=53.5\,\mathrm{mT}$  the  $\beta_4$ - and the  $e_1$ -state are degenerate and the  $\alpha_1$  and the  $e_1$  state couple strongly using a radiofrequency with  $f_0=1.609\,75\,\mathrm{GHz}$ . At  $60.5\,\mathrm{mT}$  the same applies for the  $\beta_3$  and  $e_2$  states and the  $\alpha_2$ - and  $e_2$  state couple.

 $2P_{1/2}$  state are referred to as e and f. Shown in Figure 2.10 one can see, that for hydrogen, the  $\beta_3$  and  $e_2$  states are degenerate for an external magnetic field of 60.5 mT. For the  $\beta_4$  and  $e_1$  states, the same applies at  $B = 53.5 \,\mathrm{mT}$ . In combination with an external electric field of about  $10 \,\mathrm{V\,cm^{-1}}$  (Stark effect, see subsection 2.1.8), the lifetime of the  $\beta$  states goes below  $10^{-7}$  s and all particles in this state are quenched to the ground state. At the two above given crossing points via a radiofrequency of  $f_0 = 1.60975 \,\mathrm{GHz}$ , the  $\alpha_i$  states couple to the  $e_i$  states. Three possible coupling cases can be distinguished, a "weak" coupling, where not all particles in the  $\alpha$ -states move to the e state, a "medium" coupling, where all particles in the  $\alpha$ -state are transferred to the e-state from where they decay into the ground state, and a "strong" coupling, where the radiofrequency re-excites the transferred particles back into the  $\alpha$ -state. By using a cavity with a quality factor between 1000 and 3000, it can be insured that at the crossing points one  $\alpha_i$  e<sub>i</sub> transition couples strongly while the other only couples with a medium strength [4]. So only one, the strongly coupled  $\alpha$ -state, is not quenched to the ground state. An illustration of the complete working principle of the spin filter is shown in Figure 2.11.

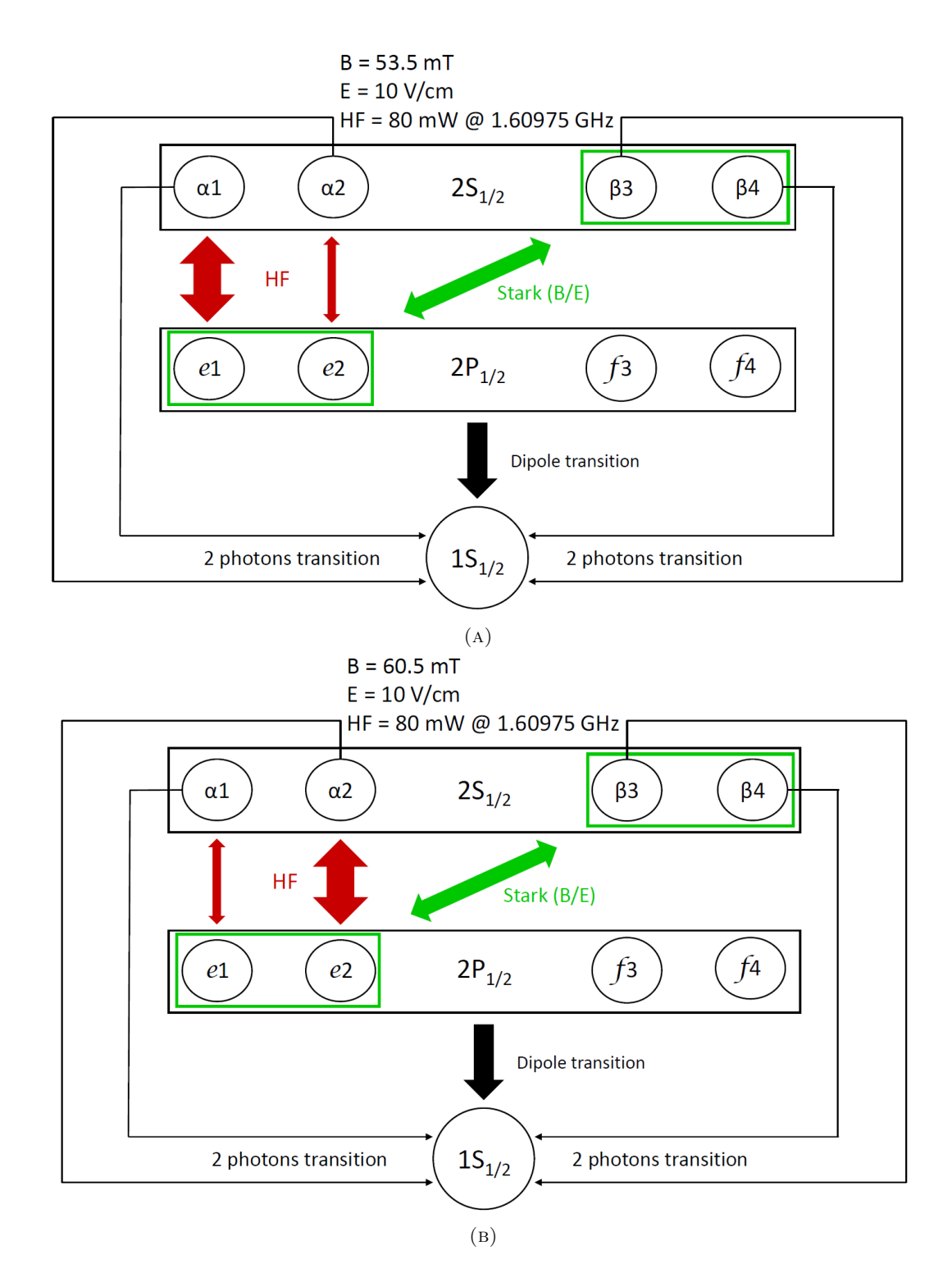


FIGURE 2.11: Working principle of the spin filter [18]. A: At  $B=53.5\,\mathrm{mT}$  the  $\alpha_1$  state can be transmitted. B: At  $B=60.5\,\mathrm{mT}$  the  $\alpha_2$  state can be transmitted. The green arrow indicates the transition via the Stark effect, the red arrows the transition induced by the radiofrequency. The big red arrow stands for strong coupling strength, the small for medium.

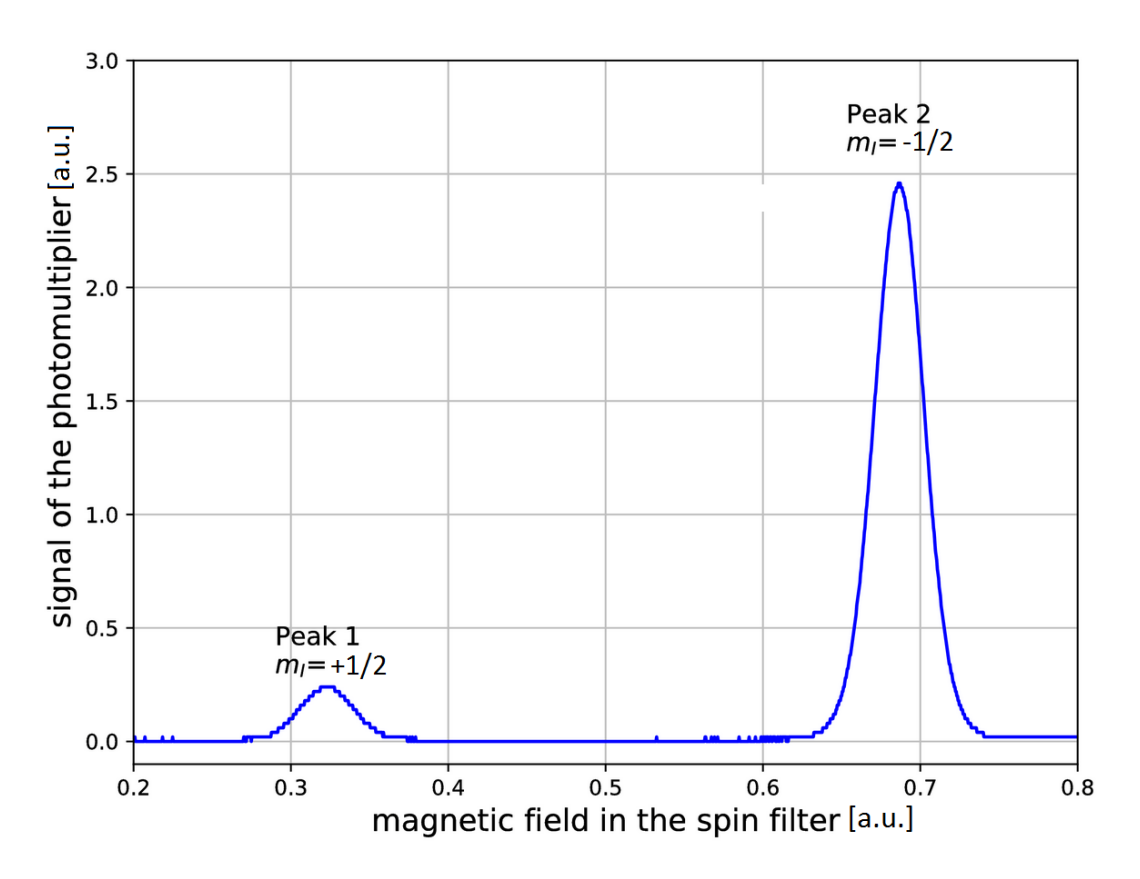


FIGURE 2.12: Exemplary Lyman- $\alpha$  spectrum of polarized hydrogen measured with a LSP.

#### 2.3.5 Quenching Chamber

After the spin filter, the surviving metastable states enter the quenching chamber. Again, using the Stark effect by applying a very strong electric field, the atoms are quenched to the ground state inside a small volume. During the quenching, Lyman- $\alpha$  photons are emitted, with an energy of  $E_{ph}=10.2\,\mathrm{eV}$ . Using a photomultiplier tube designed with a very narrow wavelength interval around the Lyman- $\alpha$  wavelength, the photons are converted to an electric signal, which can be read out with an oscilloscope. The strength of the photomultiplier signal is hereby proportional to the amount of quenched particles.

Depending on the geometry of the quench chamber, only a small amount of a few percent of the emitted photons reach the photomultiplier tube, since the photons are distributed in all directions equally. In combination with a quantum efficiency of about 10%, this results in a detection efficiency of  $10^{-3}$ . A way to increase the number of photons that reach the photomultiplier tube is to install an ellipsoidal aluminum mirror with one focus point located inside the quenching volume and the other at the entrance window of the photomultiplier.

In practice, to measure the polarization of a particle beam, the photomultiplier signal is measured while the magnetic field of the spin filter is ramped. Figure 2.12 shows a typical measured spectrum for a hydrogen beam. While the magnetic field is above or below the magnetic field needed to create the strong coupling, no meta

2.4. Sona Transition 25

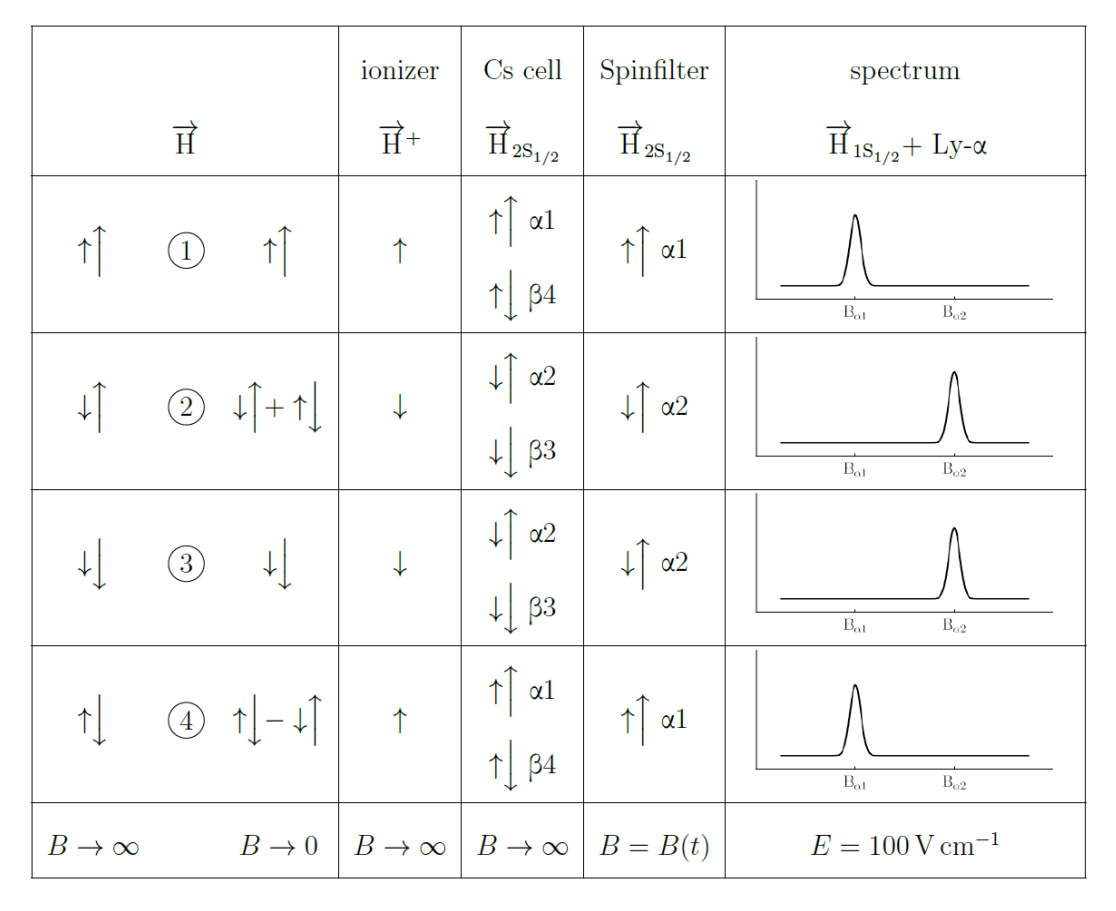


Figure 2.13: Scheme of the working principle of the LSP, according to [4]. The nuclear spin is indicated by the smaller and the electron spin by the larger arrows.

stable particle can transmit, and no signal is created. But if the magnetic field inside the spin filter reaches one of these coupling points, the respective  $\alpha$ -state is transmitted and the photomultiplier detects a Lorentz-like curve. Thereby, the peaks of the measured spectrum correspond to the occupation number of the respective spin state. Figure 2.13 shows a schematic of the operating principle of the Lamb-Shift polarimeter using hydrogen as an example.

## 2.4 Sona Transition

In 1967, P.G. Sona [37] proposed a method to increase the polarization of H<sup>-</sup> and D<sup>-</sup> beams by exchanging the occupation numbers of the metastable  $2S_{1/2}$  state. The idea of the Sona transition is to exchange the occupation number between the  $\alpha_1$  and the  $\beta_3$  state. To achieve this, a beam of polarized metastable particles is guided through a longitudinal magnetic field that reverses its field direction along the beam line. This can be realized by two solenoids, which are coaxial with the beam, but have opposing magnetic directions. Such a device creates a well-defined zero crossing of the longitudinal magnetic field. A schematic drawing of a Sona setup is shown in Figure 2.14. By reversing the direction of the magnetic field, the  $\alpha_1$  state, with both

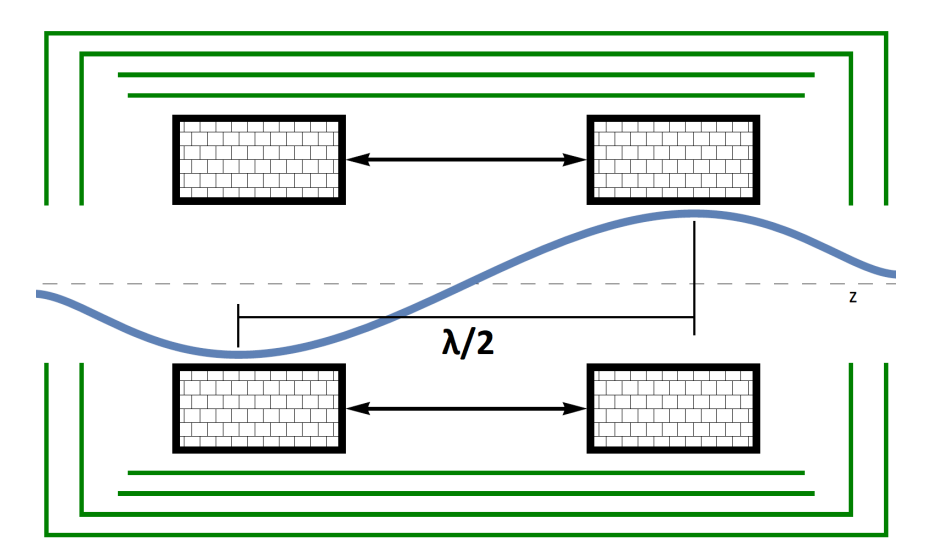


FIGURE 2.14: Sketch of a Sona transition unit [18]. The two opposing coils (black) are arranged along the beam axis z and should be shielded (green) from outside fields. The distance between the coils is  $\lambda/2$ . A typical longitudinal magnetic field curve is drawn (blue).

electron and nuclear spin parallel to the magnetic field, becomes the  $\beta_3$  state with both spins antiparallel, and vice versa. This is nothing different from extending the Breit-Rabi diagram to negative magnetic fields, as can be seen in Figure 2.15.

However, for this to work, the Larmor frequency of the total angular momentum of the atom F in the radial magnetic field has to be lower than the frequency of the reversal of the longitudinal magnetic field. According to Sona [37], this is ensured if

$$\frac{\partial B_z}{\partial z} << \frac{8v_H m_e}{er^2} , \qquad (2.53)$$

with  $v_H = \sqrt{2E_{kin}/m}$  being the velocity of the metastable particles, m the mass of these particles, r the radius of the beam and e the elementary charge. Otherwise, the spins would be able to reverse their direction along with the magnetic field adiabatically and, thus, staying in their initial state.

According to Maxwell's laws and the symmetries of the solenoids for the radial magnetic field component of the Sona transition follows

$$B_r(z,\rho) = -\frac{\rho}{2} \cdot \frac{\partial B_z}{\partial z} ,$$
 (2.54)

where  $\rho$  is the distance from the z-axis. Because the beam particles travel through the Sona transition unit with  $v_z = v_H$ , they experience a changing magnetic field, which in their inertial system is a time dependent magnetic field. With a Fourier analysis of the radial magnetic field, the frequency of the electromagnetic field seen by the particles can be obtained [8]. These frequencies are determined by the geometry of the Sona coils and the velocity of the particles  $v_H$ . The basic harmonic frequency of

2.4. Sona Transition 27

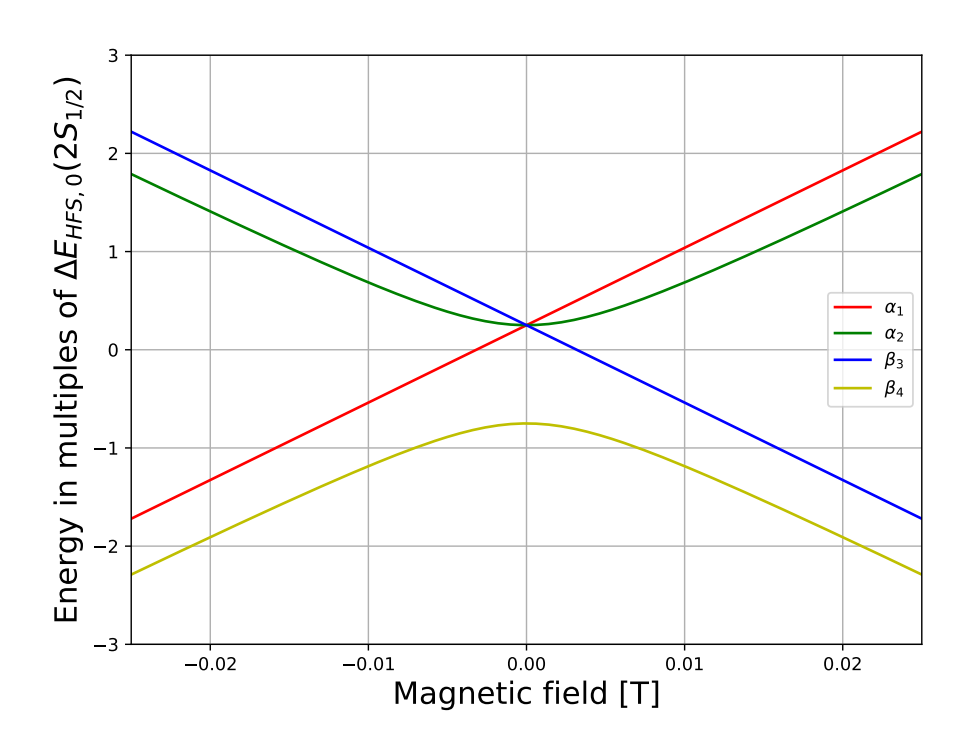


FIGURE 2.15: Breit-Rabi diagram of the  $2S_{1/2}$  state of hydrogen extended to negative magnetic fields. By crossing B=0 the state  $\alpha_1$  becomes  $\beta_3$  and vice versa. The states  $\alpha_2$  and  $\beta_4$  do not change.

the Sona transition is in the order of

$$f_{Sona} = \frac{v_H}{\lambda} , \qquad (2.55)$$

where the wavelength  $\lambda$  is approximately twice the distance between the centers of the two Sona coils. This corresponds to a photon in the particle picture with the same energy.

The oscillating radial magnetic field can induce  $\sigma$  transitions within the metastable particles, allowing them to change into another hyperfine substate with  $\Delta m_f = \pm 1$  if the energy difference between initial and final state is a multiple of  $\Delta E_{Sona} = h f_{Sona}$  or an integer multiple of it. Because photons are Bosons and therefore have a spin s=1, only odd multiples are allowed, otherwise the angular momentum conservation would be violated. Therefore, inside a Sona transition unit at different magnetic fields multi photon transitions between different hyperfine substates of the meta stable particles can occur. E.g., metastable particles in the  $\beta_3$  state change to the  $\alpha_2$  state and from there to  $\alpha_1$  or back to  $\beta_3$ . Figure 2.16 shows an example of the transitions drawn into a Breit-Rabi diagram.

For a beam of metastable hydrogen that enters the Sona transition unit in the  $\alpha_1$  state, the atoms will be transferred to the  $\beta_3$  state after the zero crossing, but from there they can change to the  $\alpha_2$  state and from there even back to the  $\alpha_1$  state. Thus, the occupation numbers between the different states start to oscillate as a function

of the magnetic field. Figure 2.17 shows a simulation of such oscillations, which was numerically calculated [8]. For the simulation, a magnetic field in the shape of a perfect sin-function was assumed, with a wavelength of  $\lambda = 32 \,\mathrm{cm}$ . The kinetic energy of the metastable hydrogen atoms was assumed to be  $E_{kin} = 1.28 \,\mathrm{keV}$ .

Based on this, the assumption is made, that the  $\alpha_1$  state peaks every time the magnetic field reaches the point where a multiphoton transition between the  $\alpha_1$  and  $\alpha_2$  state occurs. Comparing the Breit-Rabi diagram shown in Figure 2.16 and the simulated occupation numbers shown in Figure 2.17, this assumption seems reasonable. The spacing between the center of the peaks in the  $\alpha_1$  spectrum increases constantly, since the  $\alpha_1$  and  $\alpha_2$  lines in the Breit-Rabi diagram become parallel for increasing magnetic fields. For the  $\alpha_2$  spectrum the opposite is the case, here the distance between the center of the peaks becomes constant with increasing magnetic field, because the  $\alpha_2$  and  $\beta_3$  lines in the Breit-Rabi diagram diverge linearly.

In order to find particles in the  $\alpha_1$  state, they need to make the transition from  $\beta_3$  to  $\alpha_2$  first. Thus, a transition into the  $\alpha_1$  state is only possible, if the transitions  $\beta_3$  into  $\alpha_2$  and  $\alpha_2$  into  $\alpha_1$  sufficiently overlap due to the line width. However, as a result, the peaks are getting deformed, for example at a magnetic field, where both transitions  $\alpha_1 - \alpha_2$  and  $\alpha_2 - \beta_3$  occur, the amount of  $\alpha_2$  should be reduced, because most of them would end up in the  $\alpha_1$  state. Or, for magnetic fields where the  $\alpha_2 - \beta_3$  transition has a minimum and the  $\alpha_1 - \alpha_2$  transition has a maximum, the amount of  $\alpha_1$  should be reduced because there are fewer atoms in the  $\alpha_2$  state that can transition to  $\alpha_1$ .

2.4. Sona Transition 29

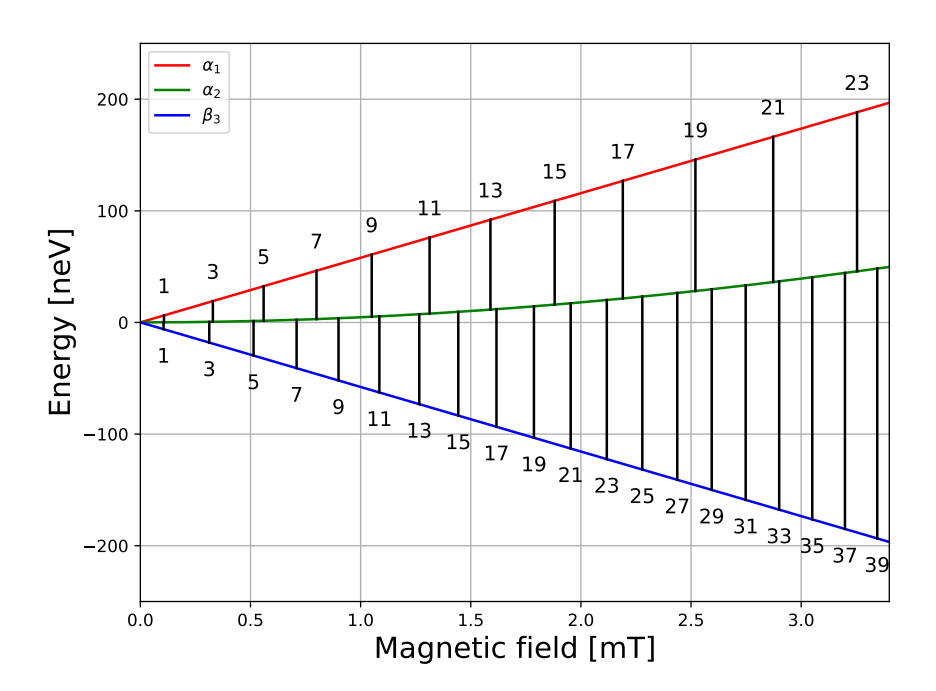


FIGURE 2.16: Example of multi photon transitions in  $2S_{1/2}$  hydrogen induced inside a Sona transition unit. The frequency of the Sona transition was chosen to  $f_{Sona}=1.5\,\mathrm{MHz}$ , which corresponds to an  $\Delta E\approx 6.93\,\mathrm{neV}$ . The counting labels indicate the number of photons needed for the transition.

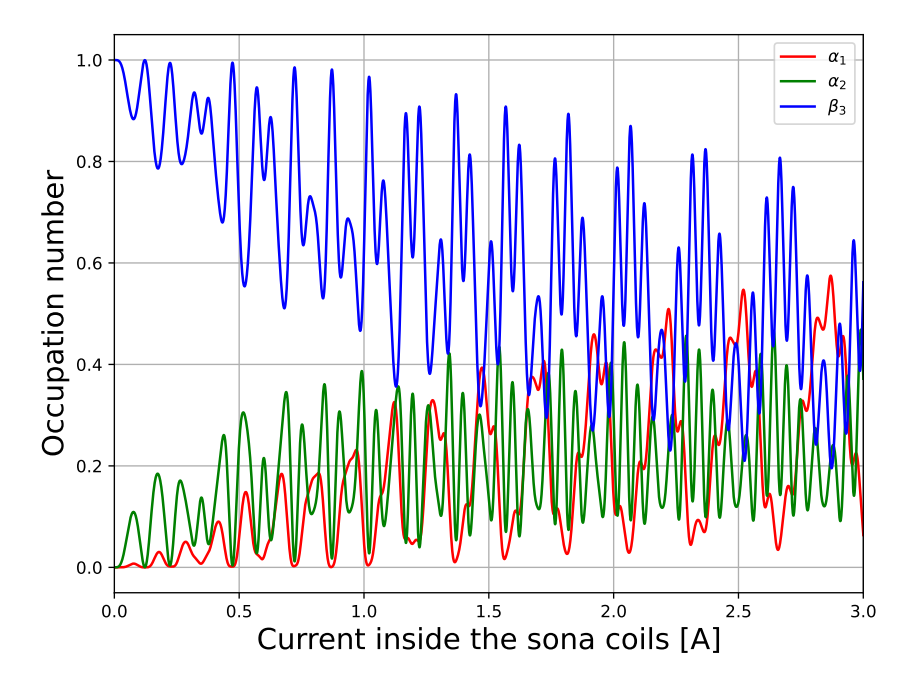


FIGURE 2.17: Simulation of the occupation numbers of three hyperfine substates of  $2S_{1/2}$  hydrogen in a Sona transition unit. For the simulation, a magnetic field in the shape of a perfect sin-function was assumed, as well as a kinetic energy for the metastable particles of  $E_{kin}=1.28\,\mathrm{keV}$  and a distance of the coils centers of 16 cm.

# Chapter 3

# Experimental Setup

As mentioned in chapter 1 the measurements presented in this thesis were performed at the Institut für Kernphysik at the Forschungszentrum Jülich. The main components of the exeriment are a customized version of the monogan® M-100 ECR ion source sold by the company Pantechnik¹, a Wienfilter, a cesium cell, two spin filters, a Sona transition unit and a quench chamber with a photomultiplier tube on top of it. Between the ECR-source and the Wienfilter, as well as under the quench chamber, turbo molecular pumps are mounted which provide the vacuum inside the components. A schematic drawing of the setup is shown in Figure 3.1 and a series of photos of the apertures inside the laboratory can be found in Appendix B. For a good alignment of the different components, everything was mounted on a bench. The vacuum conditions are measured at two locations using pressure gauges. The first is behind the ECR source above the first pump. There, the vacuum fluctuates between  $8 \times 10^{-7}$  mbar and  $1 \times 10^{-6}$  mbar. The second pressure gauge is located on the side of the quench chamber, there the vacuum conditions are slightly worse with a pressure of around  $3 \times 10^{-6}$  mbar.

<sup>1</sup>https://www.pantechnik.com/

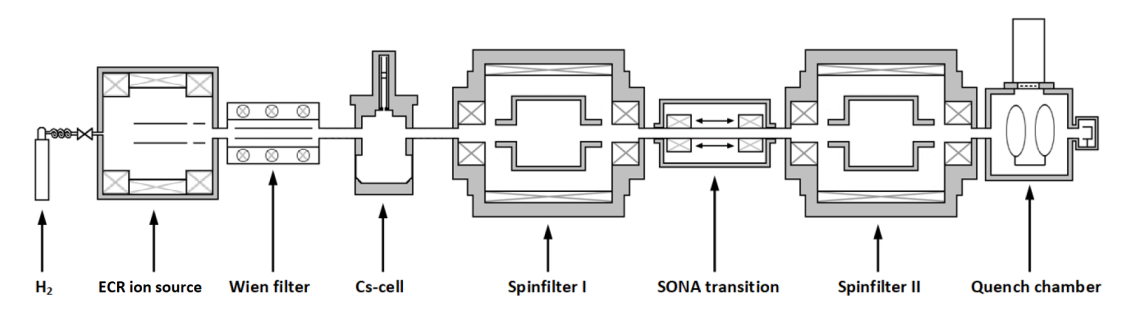


FIGURE 3.1: Schematic drawing of the experimental setup. Stating from left to right, there is the H<sub>2</sub>-bottle, the ECR ion source, the Wienfilter, the cesium cell, the first spinfilter, the sona transition, the second spin filter, and the quench chamber with a photomultiplier tube mounted on top of it.

## 3.1 Electron Cyclotron Resonance Ion Source

The electron cyclotron resonance ion source is used to generate a beam of ionized hydrogen atoms. Originally, it was fuelled by a hydrogen generator, which is now replaced by a bottle of molecular hydrogen, because the hydrogen generator proved to be insufficient for the purpose of this experiment. The incoming hydrogen flux is controlled by a mass flow controller, limiting the maximum possible hydrogen flux to  $2\,\mathrm{mbar}\,\mathrm{L\,s^{-1}}$ . A  $2.45\,\mathrm{MHz}$  radiofrequency with a power of up to  $100\,\mathrm{W}$  is used to induce the electron cyclotron resonance inside the source. The electrons excited by the ECR break the covalent bond of the molecular hydrogen, creating atomic hydrogen ions. To accelerate the ions, a positive potential of up to  $10\,\mathrm{keV}$  is used in combination with a negative potential of up to  $-20\,\mathrm{keV}$  used for focusing. After leaving the ECR source, the ion beam pass through another electrostatic focusing lens, located between ECR source and Wienfilter.

## 3.2 Wienfilter

The Wienfilter is located after the electrostatic lens and before the cesium cell. As discussed in subsection 2.3.2, it operates as a mass and velocity filter to ensure that the proton beam is mono energetic. The required magnetic fields perpendicular to the beam axis are generated by a magnet consisting of two copper coils, each surrounded by a C-shaped iron rod. The coils are cooled with water. Between the coils is a vacuum chamber through which the beam passes. On the top and the bottom of the inside of this chamber, two isolated plates are mounted parallel to each other. Each of the plates is connected to a high voltage supply, one to a positive, the other to a negative one. These are used to create the electric field perpendicular to the beam axis and the magnetic field direction. Because each plate can be controlled individually, they can also be used to slightly manipulate the beam axis. Around the whole apparatus a steel box is mounted, functioning as a magnetic yoke. Since the beam is not polarized at this point, Larmor precession does not affect the measurement, so the field combinations can be freely chosen.

## 3.3 Cesium Cell

The cesium cell consists of a stainless steel vacuum chamber with openings on both sides for the beam to pass through. Two holes are drilled in the bottom and top of the cell respectively, in each case one is equipped with a heating rod and the other with a Pt-100 thermal sensor. So, in combination with a PID controller, the temperatures of the top and bottom of the cell can be controlled up to an uncertainty of  $\Delta T = 0.1$  °C. The top temperature is set to a value of 60 °C and the bottom to 160 °C. At these temperatures, the vapor pressure of cesium is about 1 mbar at the bottom and about 0.01 mbar at the top, producing a cesium vapor that interacts

with the beam. On the top side of the cell, a mechanism to hold and crack a glass ampule filled with cesium is mounted, which is used to fill the cesium into the cell at the beginning of a measurement run. In this way, the beam can interact with the cesium and metastable hydrogen atoms are produced. Since the particle beam is not polarized yet, no magnetic holding field and therefore no coils around the cesium cell are needed. Figure 3.2 shows a schematic drawing of the cesium cell. Note, that once the cesium ampule is broken, over time the cesium diffuses to the other parts of the aperture and deposits there on surfaces which can create electric shortcuts. To minimize this effect, before and after the cesium cell valves are mounted, which are kept closed when no experiments are performed.

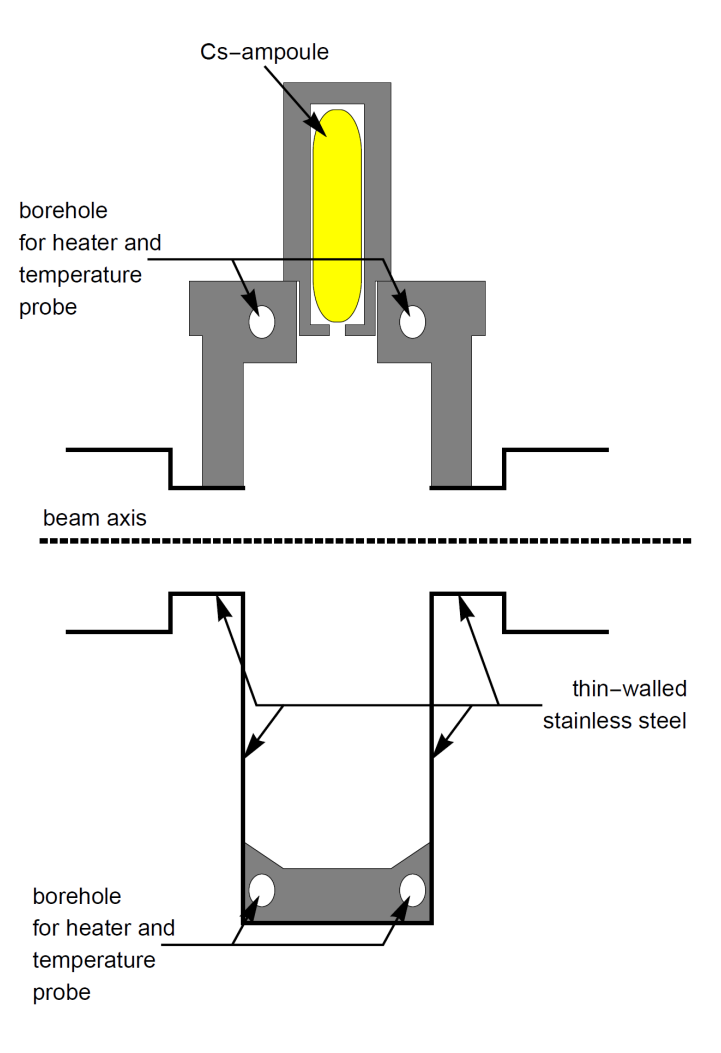


FIGURE 3.2: Schematic drawing of a cesium cell [18]. On the top side, inside the cracking mechanism, the cesium ampule is located. On the top and bottom, one can see the boreholes for the heating rods and temperature probes.

## 3.4 Spin Filters

As discussed in subsection 2.3.4 a spin filter allows a selective transmission of metastable atoms in one hyperfine substate only, using a combination of static magnetic and

electric fields and an injected radiofrequency. The magnetic fields are created by a solenoid, located around the beam axis. The static electric fields as well as the radiofrequency are provided by a cylindrical cavity placed in the center of the solenoid. Figure 3.3 shows a schematic drawing of the spin filter.

Two identical designed spin filters are used in this experiment. The first is set up before the Sona transition unit, generating the polarization of the particle beam. After the cesium cell, the beam consists of hydrogen atoms in all four metastable  $2S_{1/2}$  states. The magnetic field of the first spin filter is set to  $53.5\,\mathrm{mT}$ , which allows only atoms in the  $\alpha_1$  state to be transmitted. Atoms in the  $\alpha_2$  state and both  $\beta$  states are quenched to the ground state, so that after the spin filter, all remaining metastable particles in the beam are in the  $\alpha_1$  state. Thus, the beam is now polarized. The second spin filter is located behind the Sona transition unit and used in the classical way as part of the LSP. However, during the measurement the magnetic field is not ramped but fixed to either  $53.5\,\mathrm{mT}$  or  $60.5\,\mathrm{mT}$ , depending on whether the  $\alpha_1$  or  $\alpha_2$  oscillation spectrum is measured. Since the Sona transition unit inverts the magnetic field direction, the magnetic fields of both spin filters point in opposite directions.

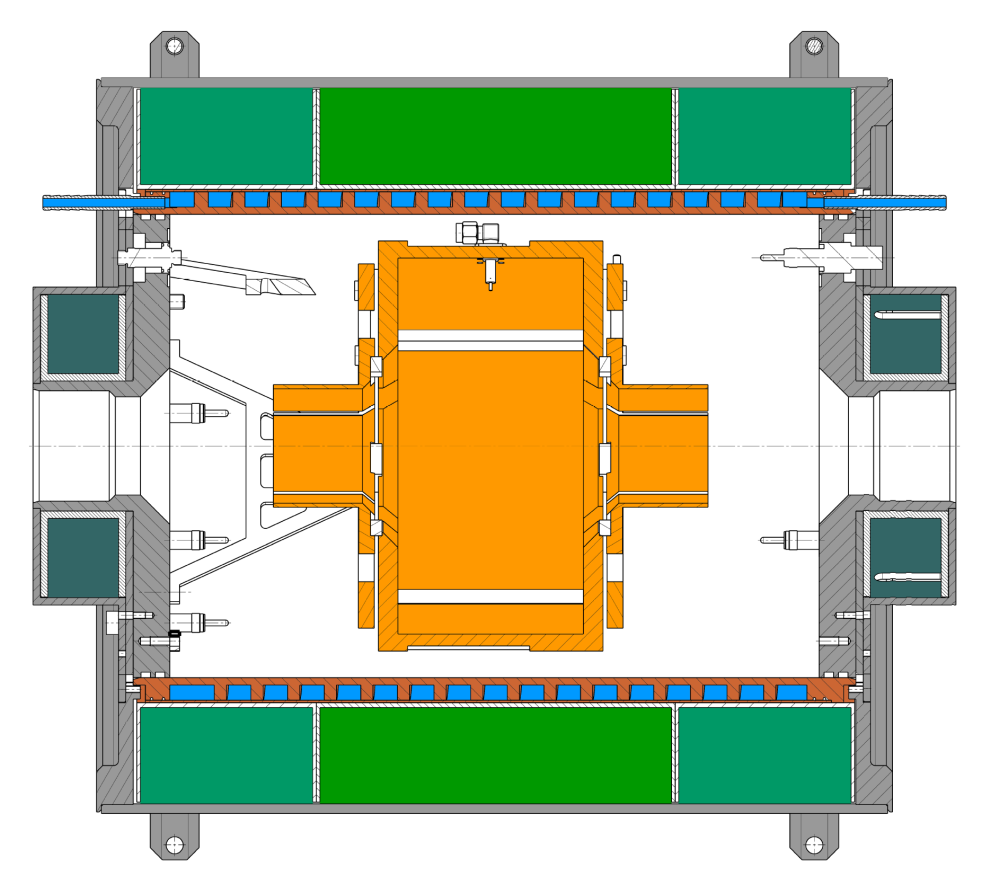


FIGURE 3.3: Schematic drawing of a spin filter [18]. The homogeneous magnetic field is primarily generated by the three main coils (green). The two end coils (dark green) reduce the gradients at both ends. The main coils are cooled by a copper heat sink (orange), which in turn is cooled by water (blue). The outer part have a high permeability to purpose as magnetic yock. The cavity (dark orange) and the inner parts have a low permeability to minimize their effect on the magnetic

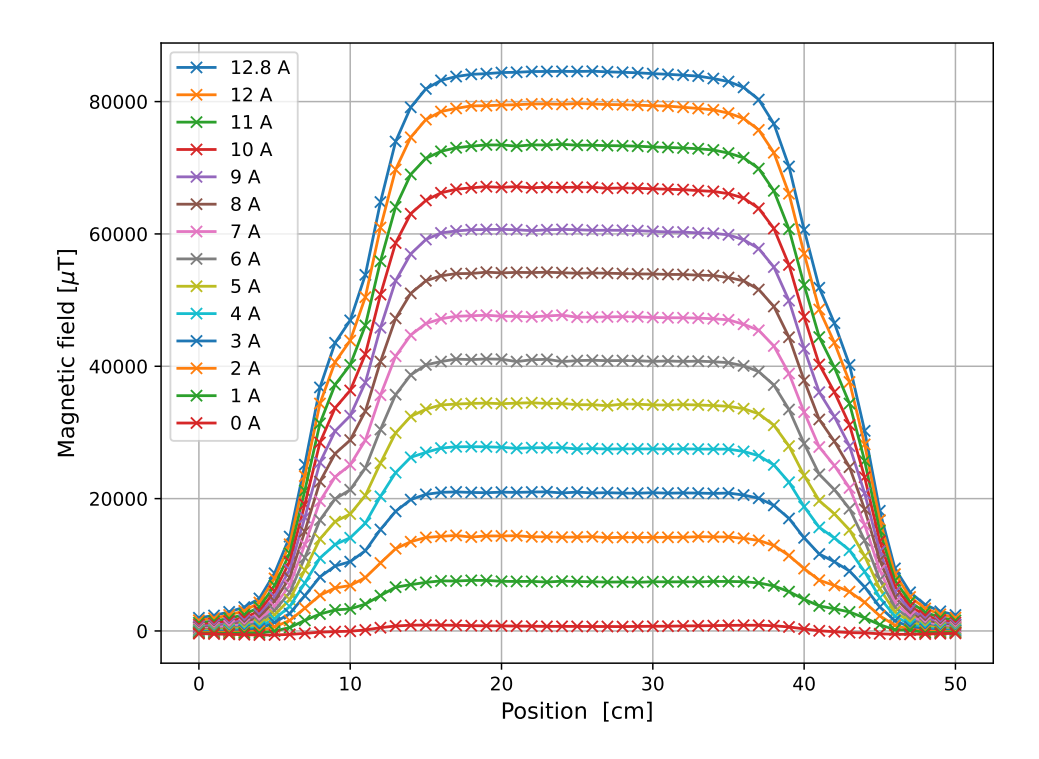


FIGURE 3.4: Longitudinal magnetic field along the spin filter beam axis at different currents.

### 3.4.1 Solenoid

For the spin filter to function properly, magnetic fields with a high homogeneity are needed. They are provided by a solenoid consisting of five coils which are connected in series. The three central coils create a magnetic field plateau in the area of the cavity. The coils are tuned to allow a high homogeneity of  $\frac{\Delta B}{B} < 10^{-3}$  for fields between 50 mT and 65 mT. Additionally, at both ends of the spin filter, two end coils are located. They decrease the magnetic gradient to avoid that the metastable atoms quench due to fast changing fields while entering or leaving the spin filter. Figure 3.4 shows the longitudinal magnetic field of the spin filter along the beam axis for different currents. The three central coils are cooled by a copper heat sink run through by water.

#### **3.4.2** Cavity

The cylindrical shaped cavity provides the static electric and the radiofrequency field. It is located in the center of the spin filter and is divided in three sections along the beam axis, the central section, in which the radiofrequency is stored, and two identical closure heads, confining it to the central part. Each section is divided into four quadrants. Each outer quadrant is connected to the corresponding inner quadrant, but each section is still electrically isolated. On two opposing quadrants

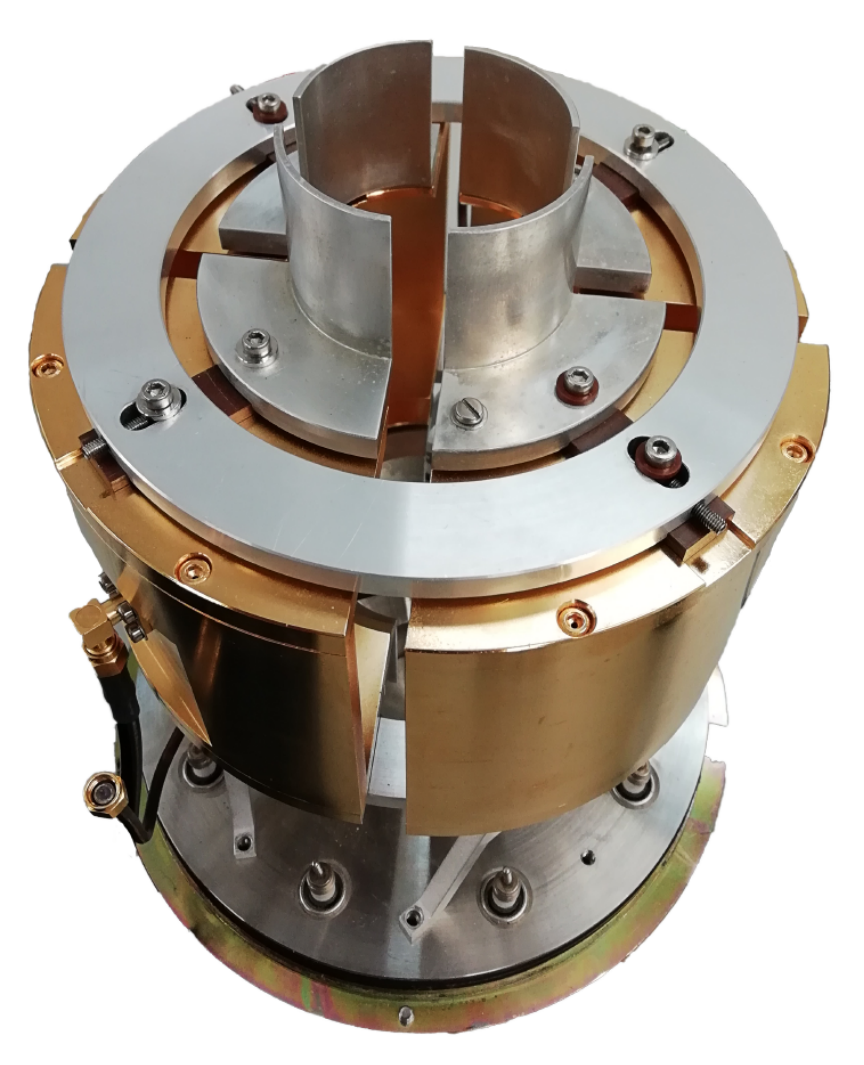


FIGURE 3.5: Photo of a dismantled spin filter cavity [18]. The four gold colored quadrants in the center are the main part of the cavity into which the high frequency is coupled. The silver colored outer quadrants can be seen at the top, as well as a silver colored ring that is part of the holding structure. An identical set is hidden on the bottom.

of the central section each, an antenna is mounted, one is connected to a frequency generator, used for supplying the radiofrequency, and the other serves as pickup to measure and tune the cavity. The other two quadrants are connected to high voltage power supplies, providing the static electrical field used for the quenching. The inner diameter of the main cylindrical part is  $d=142\,\mathrm{mm}$ . Due to the skin effect, the enclosed cylinder perfectly matches the required frequency of 1.6975 GHz to excite the transitions between the  $\alpha$  and e states. The quality factor of both spin filters was measured. Both comply with the  $Q=\frac{f_0}{\Delta f_0}\in[1000\ ;\ 3000]$  limitation, that is needed to ensure that when one  $\alpha$  state couples strongly, the other still couples with a medium strength. A photo of a dismantled cavity is shown in Figure 3.5

### 3.5 Sona Transition Unit

The Sona transition unit is located between the two spin filters and consists of two coils identical in design. They produce opposing longitudinal magnetic fields, each in the field direction of the adjacent spin filter field, so that in total the magnetic field reverses along the beam axis. An exemplary configuration of the longitudinal magnetic fields can be seen in Figure 3.6. The coils are shielded with four layers of  $\mu$ -metal against the stray fields of the spin filters and other magnetic fields. Everything is mounted on a vacuum pipe in which the beam passes through. Using a threaded nylon rod and nylon nuts, the coils are mounted with a fixed distance between their centers, for the purpose of the following experiment the distance was chosen to be  $16 \pm 0.5$  cm. During the measurements, the current is ramped using a ramp generator with a saw tooth function.

The magnetic field profile of the Sona transition unit and the two adjacent spin filters was measured using an axial Hall-probe, which was guided through the structure with a  $\rho \approx 10$  mm offset parallel to the beam axis. Figure 3.7 shows the longitudinal magnetic field  $B_z$  inside the Sona transition unit for different coil currents. One can see the well-defined zero crossing approximately in the middle of the transition unit. Figure 3.8 shows the radial magnetic field  $B_r$  for these currents, which were calculated using the derivative of the z-component of the magnetic field and the relation presented in Equation 2.54. Looking at radial magnetic field distribution, one can see that the expected  $\lambda$  should be about the order of 27 cm, perhaps even lower due to the double-peaked structure in the center.

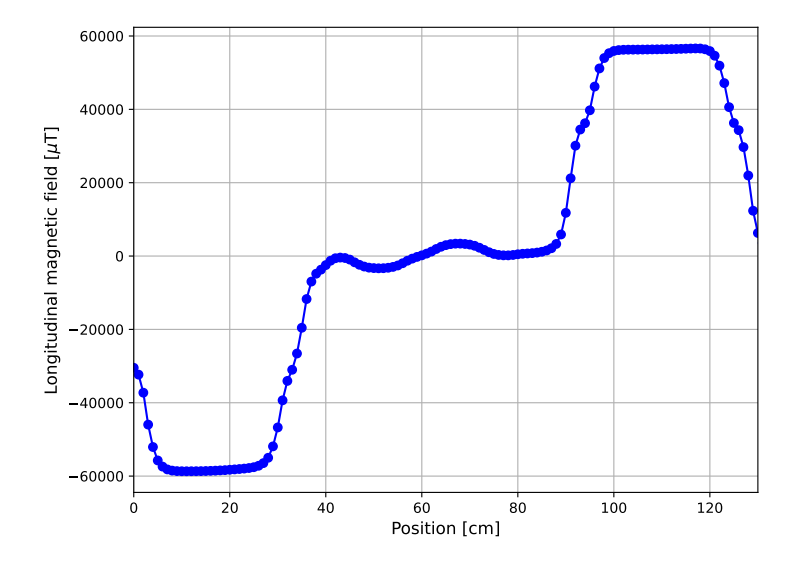


FIGURE 3.6: Longitudinal magnetic field configuration of the Sona transition unit and both spin filters. On the right is the field of the second spin filter, in the middle that of the Sona transition unit, and on the left that of the first spin filter. The current inside the Sona coils was 2 A and inside the spin filter coils 9 A.

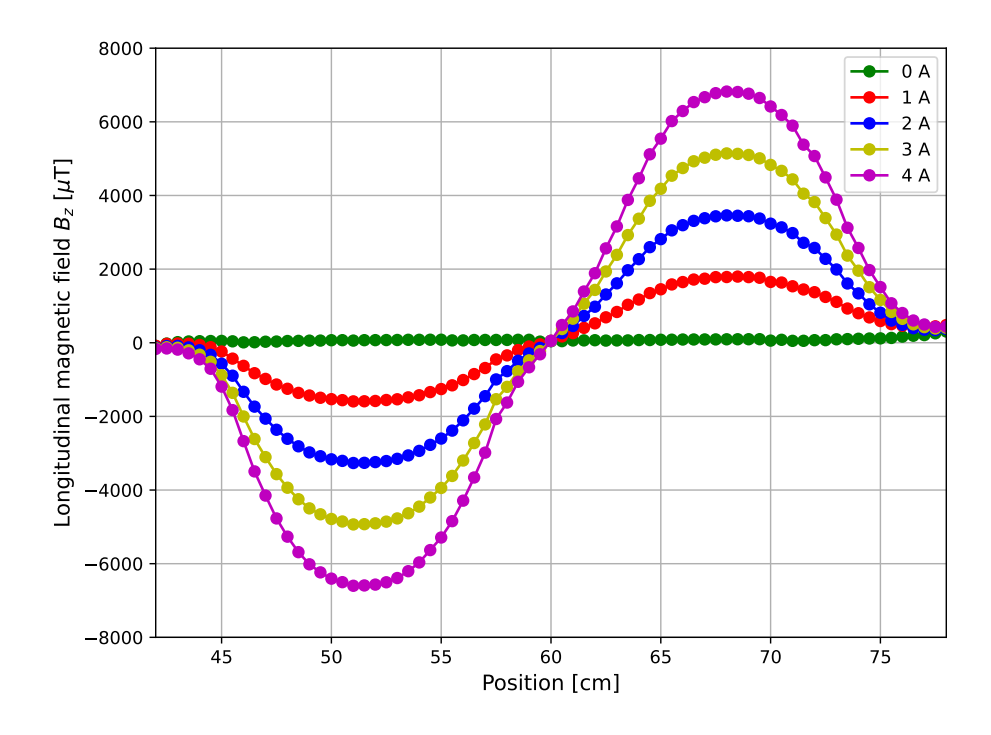


Figure 3.7: Longitudinal magnetic field  $B_z$  of the Sona transition unit measured for different currents.

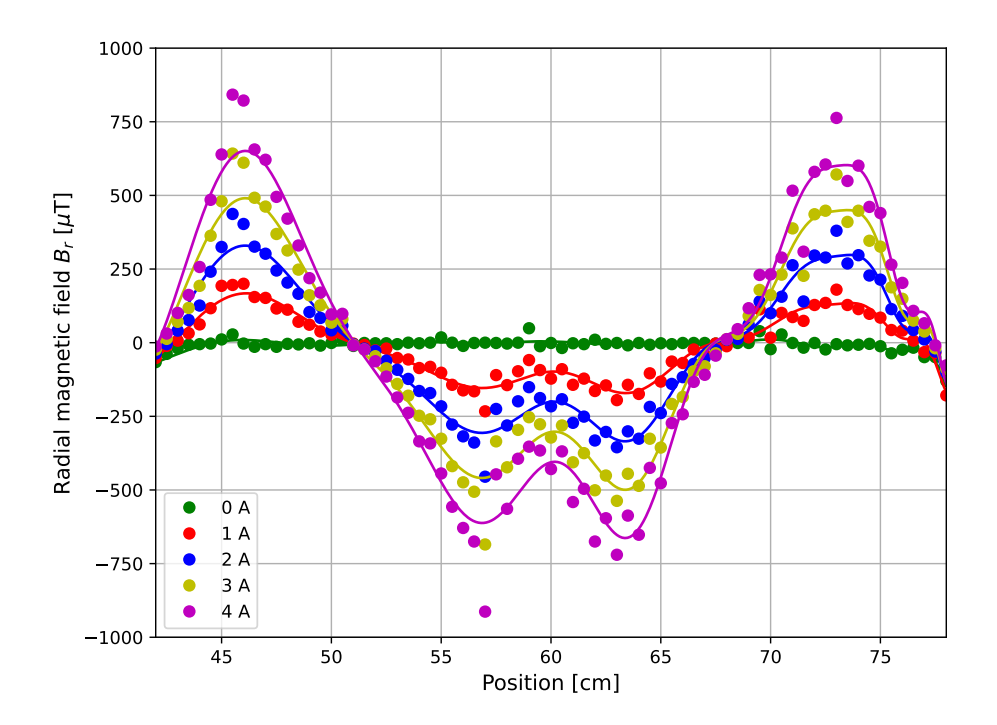


Figure 3.8: Calculated radial magnetic field of the Sona transition unit for different currents. The relation from Equation 2.54 is used and a distance to the beam axis of  $\rho \approx 10\,\mathrm{mm}$  was assumed.

## 3.6 Quench Chamber

As quench chamber, a cylindrical vacuum chamber is used. On the top side of the chamber, a photomultiplier tube is mounted, detecting the Lyman- $\alpha$  photons that are generated during the quenching of the remaining metastable particles inside the beam. The beam particles enter the chamber through a stainless steel tube. At the end of the chamber a second steel tube is positioned and between those a Teflon tube. Inside the Teflon tube an isolated electric ring electrode is mounted which is connected to a high voltage supply. The two steel tubes are grounded, so that a strong electric field of around  $E \approx 200\,\mathrm{V\,cm^{-1}}$  can be produced, inducing the quenching in the area of the Teflon tube. In the direction of the photomultiplier tube, the Teflon tube has a hole for the photons to escape. The signal of the photomultiplier tube is read out with an oscilloscope and recorded in combination with the signal of the ramp generator, ramping the magnetic field of the Sona transition unit.

## 3.7 Problems during the Measurements

During and after the measurements conducted presented in this thesis, a few problems with the experimental setup were discovered which had unforeseen influences on the measurements and need to be considered in the analysis and interpretation of the measurements. The problems are of different significance and can be clearly associated with individual parts of the setup.

### 3.7.1 ECR Plasma

Already during the measurements the ECR source was not working properly, only for short periods of time and only an instable plasma could be ignited. After a maximum of two measurements, the plasma extinguished, and the source needed to be restarted. During each restart, the high voltages needed to be readjusted, resulting in different beam conditions after each restart. Also, the accelerating and focusing voltages were limited far beyond the manufacturer specifications. Another main problem was, that the generated particle beam mostly consisted of ionized N, O, N<sub>2</sub>, and O<sub>2</sub>. Hydrogen accounted for only a few percent of the beam current. Thus, it is assumed that a leak in the ECR source allowed atmosphere to enter. Figure 3.9 shows the beam current after the Wienfilter as function of the magnetic field of the Wienfilter. In agreement with Equation 2.46, the first peak corresponds to the lightest ions, i.e., protons, and with  $\sqrt{B}$  dependence the other heavier ions follow.

By now, it is understood that these problems arose from a wrongly connected high voltage, which is going to be fixed for future measurements. However, for the measurements presented later, this means that the measured beam was far from being Gaussian shaped like assumed in the simulation presented in subsection 2.3.5. Also, the different measurement runs can only be compared with caution, because the stability of the beam energy was limited.

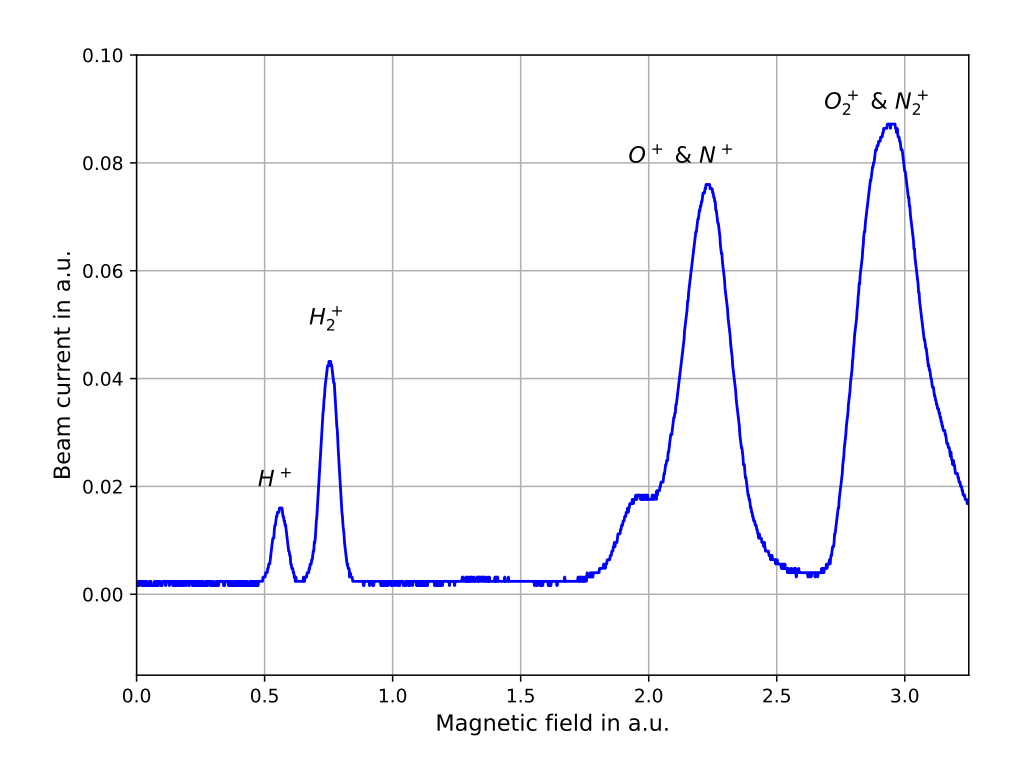


FIGURE 3.9: Wienfilter mass spectrum of the ion beam generated by the ECR source.

### 3.7.2 Spin Filter Stray Fields

Another influence on the measurement that was discovered later is that the  $\mu$ -metal shielding around the Sona unit is not sufficient. Due to that, the stray fields of the spin filters reach inside the Sona transition unit, slightly changing its magnetic field curve. For the first spin filter, this is effect is negligible, because during the measurements the first spin filter fields are not changed. However, for the second spin filter, this is not the case. As discussed before, depending on which spectrum should be measured, a magnetic field of either 53.5 mT or 60.5 mT has to be setup inside the second spin filter. Figure 3.10 shows the two longitudinal magnetic fields inside the Sona transition unit for the same current inside the Sona coils, but for the different magnetic field settings of the second spin filter. One can clearly see, that for the 60.5 mT setting, over the hole length of the Sona transition unit, an additional offset is added to the magnetic field in comparison to the 53.5 mT setting. Figure 3.11 shows the direct difference  $\Delta B$  between the different spin filter settings. Coming closer the to the second spin filter, the offset drastically increases, reaching a relative deviation  $\frac{\Delta B}{B_z}$  of up to 20 % while the average difference is in the order of less than 20  $\mu$ T. This asymmetric offset changes the shape of the magnetic field in a way that should result in a different  $\lambda$  for each of the two settings. To get an idea of the magnitude of the  $\lambda$  change, sine function fits were applied to the curves shown in Figure 3.10. The relative change of  $\lambda$  for the two settings is approximately in the order of 0.2%.

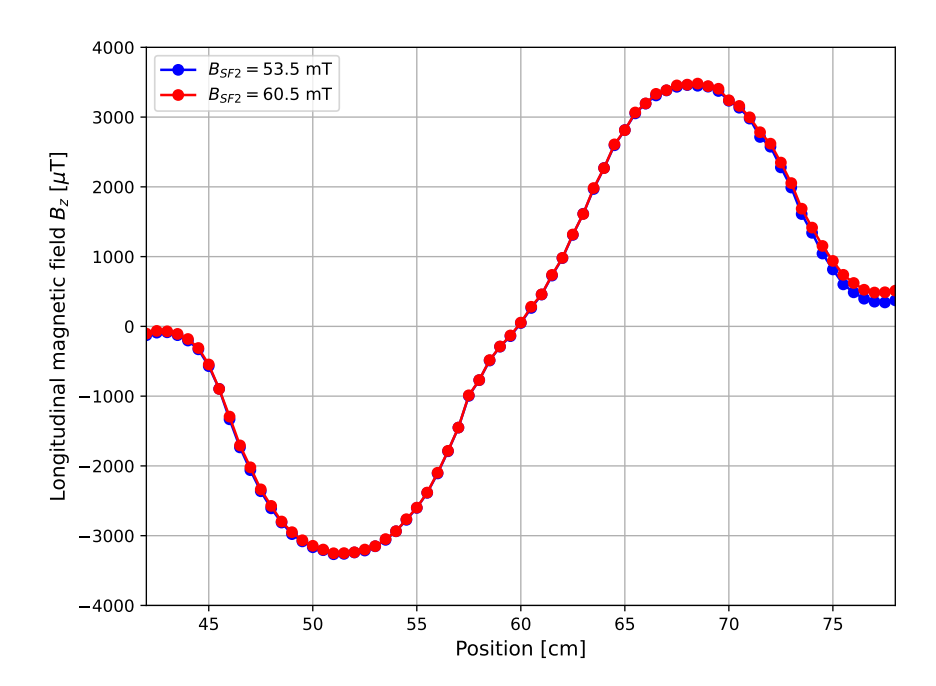


FIGURE 3.10: Longitudinal magnetic fields of the Sona transition unit for different magnetic field settings of the second spin filter (i.e. for  $53.5\,\mathrm{mT}$  (blue) and  $60.5\,\mathrm{mT}$  (red) in the second spin filter.). For both lines, the current inside the Sona coils was  $2\,\mathrm{A}$ .

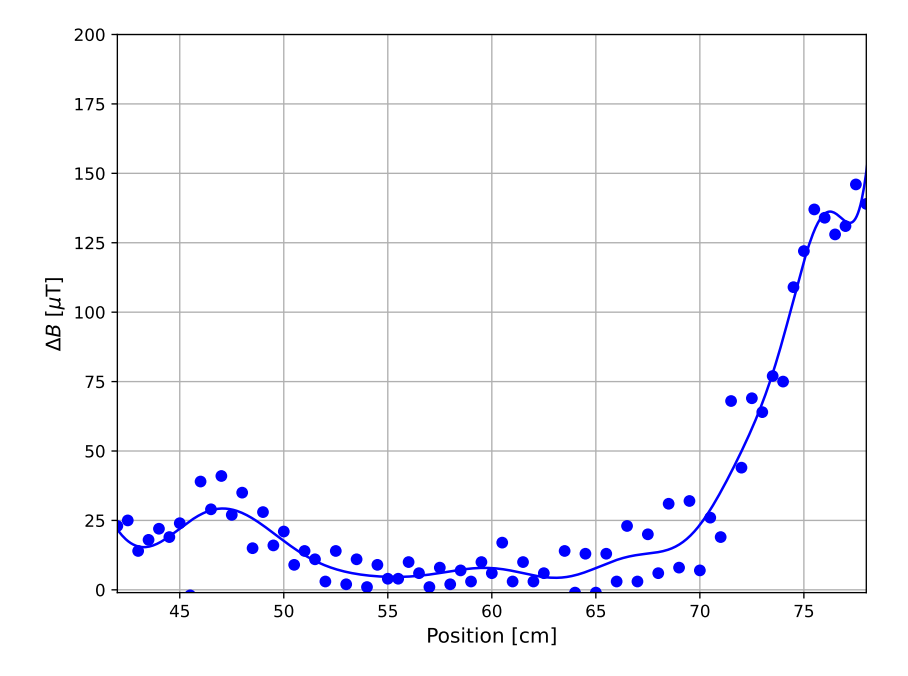


Figure 3.11: Influence of stray fields of the second spin filter on the Sona transition unit. The difference  $\Delta B$  increases as the distance to the second spin filter decreases.

# Chapter 4

# Measurements and Analysis

## 4.1 Principle of Measurement

As stated in chapter 1 the first goal of this thesis is to observe and measure the oscillations between the occupation numbers of different hyperfine substates of metastable  $2S_{1/2}$  hydrogen induced inside a Sona transition unit. To achieve this, the in chapter 3described setup is used. A beam of unpolarized hydrogen ions is created by the ECR ion source and made mono energetic using a Wienfilter. Inside the cesium cell, the ions are transformed back into atoms, where some of them end up in the metastable  $2S_{1/2}$  state. In the first spin filter, three out of four hyperfine substates are quenched to the ground state and atoms in one substate, either  $\alpha_1$  or  $\alpha_2$ , will survive. Inside the Sona transition unit while its field is ramped, the oscillations between the different substates occur and the metastable  $2S_{1/2}$  hydrogen passes into the second spin filter in either the  $\alpha_1$ ,  $\alpha_2$  or  $\beta_3$  state. Since the magnetic field of the second spin filter is set on the fixed strength and not ramped, again only the metastable hydrogen in one of the  $\alpha$ -states is transmitted, quenched inside the quench chamber and detected by the photomultiplier tube. Thereby, the measured photon intensity corresponds to the relative amount of the respective  $\alpha$  state that is transmitted. So, by measuring the signal of the photomultiplier tube as function of the ramped magnetic field of the Sona transition unit, the oscillations spectra shown in Figure 2.17 are measured for  $\alpha_1$  and  $\alpha_2$ , respectively. The recording of one ramping operation is counted as a single measurement. For a better statistic, in one measurement series, multiple measurements of the same spectrum are averaged to get one Sona spectrum for each  $\alpha$  state per measurement series.

Due to the problems with the ECR ion source, described in section 3.7, only twelve measurements series could be recorded, of which only nine are complete, including the Sona spectra for both  $\alpha$  states. The measurements were taken at beam energies from 0.99 keV to 1.5 keV. A list of the measurements series and the measurement parameters can be found in Appendix C. For all kinetic energies, the oscillations of the occupation numbers could be detected. Figure 4.1 and Figure 4.2 show exemplary the measured Sona spectra of the  $\alpha_1$  and  $\alpha_2$  state at a kinetic energy of  $E_{kin} = 1.27 \,\text{keV}$ . The shapes of the other measurement series are quite similar. The oscillations are clearly visible for all measurement series. However, each spectrum is superimposed with a non-linear

offset function. Here, the partial negative offset in the  $\alpha_2$  spectra is surprising. The fact that the signal strength falls below the value at t=0 indicates that the amount of  $\alpha_2$  after the first spin filter is non-zero, which should not be the case and could be an indication of beam misalignment.

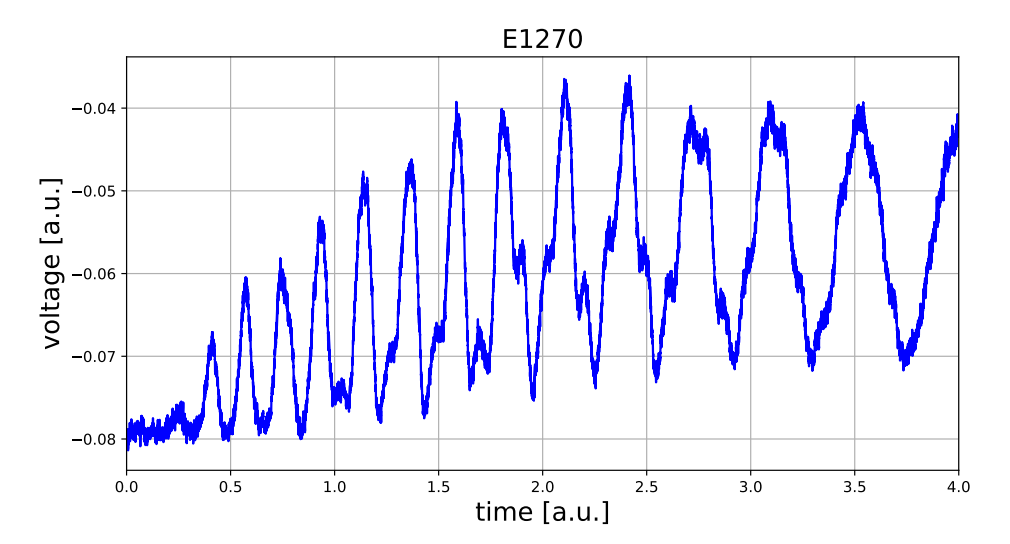


FIGURE 4.1: Measured Sona spectrum of the  $\alpha_1$  state of the measurement series 'E1270\_1'. The magnetic field inside the second spin filter was at 53.5 mT. The kinetic energy of the metastable hydrogen atoms was 1.27 keV.

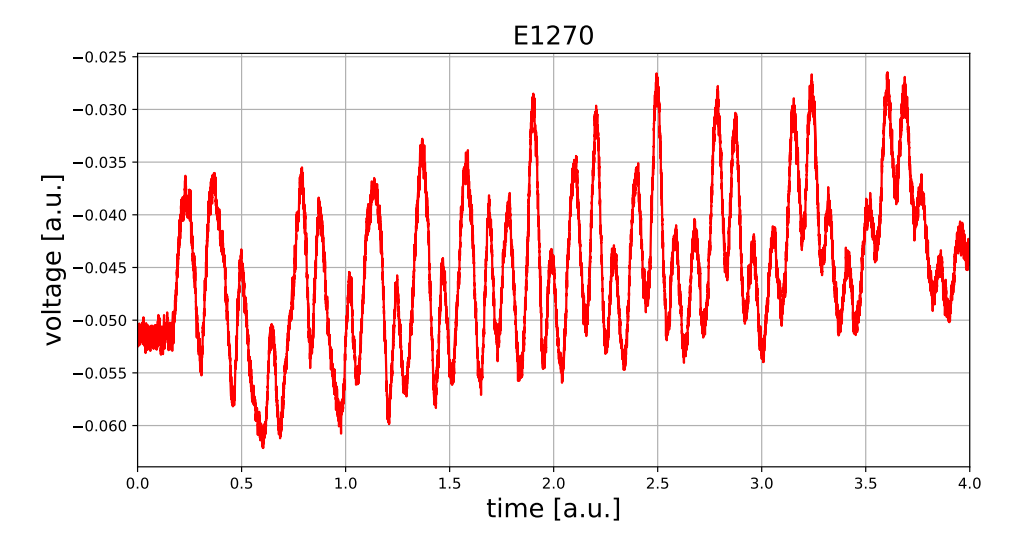


FIGURE 4.2: Measured Sona spectrum of the  $\alpha_2$  state of the measurement series 'E1270'. The magnetic field inside the second spin filter was at 60.5 mT. The kinetic energy of the metastable hydrogen atoms was  $1.27\,\mathrm{keV}$ .

## 4.2 Principle of Analysis

The second goal of this thesis is to investigate the change in the binding energy of  $2S_{1/2}$  hydrogen, with a precision that allows to verify the in subsection 2.2.2 introduced QED corrections to the Breit-Rabi formula. However, in the experiment, the Breit-Rabi curves can not be measured directly. The only available data are the Sona spectra of the two  $\alpha$  states. Therefore, the relation between the energy difference  $\Delta E_{\alpha_1,\alpha_2} = (\delta E_{\alpha_1,QED} - \delta E_{\alpha_2,QED})$  and  $\Delta E_{\alpha_2,\beta_3} = (\delta E_{\alpha_2,QED} - \delta E_{\beta_3,QED})$  and the recorded Sona spectra is used to investigate the Breit-Rabi formula. Using the Breit-Rabi formulas given in Equation 2.42, the energy differences result in

$$\Delta E_{\alpha_1,\alpha_2}(B) = \frac{\Delta E_{HFS,0}}{2} + d_1 (1 + \eta_1) - \frac{\Delta E_{HFS,0}}{2} \sqrt{1 + c_2 (1 + \delta_2) \frac{\mu_B B^2}{\Delta E_{HFS,0}}}$$
(4.1)

$$\Delta E_{\alpha_2,\beta_2}(B) = -\frac{\Delta E_{HFS,0}}{2} + d_1 (1 + \eta_1) + \frac{\Delta E_{HFS,0}}{2} \sqrt{1 + c_2 (1 + \delta_2) \frac{\mu_B B^2}{\Delta E_{HFS,0}}} \ . \ (4.2)$$

Figure 4.3 shows these energies differences as function of a longitudinal magnetic field. These energy differences are the transition energies required for the polarized hydrogen atoms to change from the  $\beta_3$  to the  $\alpha_2$  state and  $\alpha_2$  to the  $\alpha_1$  state. The further procedure is now to extract the transition energy as function of the longitudinal magnetic field from the measured  $\alpha$  spectra.

As discussed in section 2.4 the assumption is made, that the  $\alpha_1$  spectra peaks every time the longitudinal magnetic field inside the Sona transition unit reaches a value where the energy difference between the  $\alpha_1$  and  $\alpha_2$  states is equal to an odd multiple of the energy  $\Delta E_{Sona}$  which is defined by the basic harmonic frequency of the Sona transition unit. The same assumption is made for the relation between the  $\alpha_2$  spectra and the energy difference between the  $\alpha_2$  and  $\beta_3$  states. So the transition energies at the center of the peaks are according to their chronological appearance 1  $\Delta E_{Sona}$ ,  $\Delta E_{Sona}$ , ..., (2n+1)  $\Delta E_{Sona}$ .

To get the magnetic field of each peak, one needs to consider that the longitudinal magnetic field inside the Sona transition unit is not constant. So, for the purpose of the following analysis, an average longitudinal magnetic field  $B = B_{av}$  has to be assumed, that defines the Breit-Rabi diagram inside the Sona transition unit. The specific values of this average magnetic field are not known, but it should also be a linear function of the coil current. Since, this current is ramped linearly over time, the measured time can be used to describe  $B_{av}$ , if one shifts t = 0 to the starting point of the ramping signal. Therefore, for simplicity, the Sona spectrum is analyzed as a function of the measured time t.

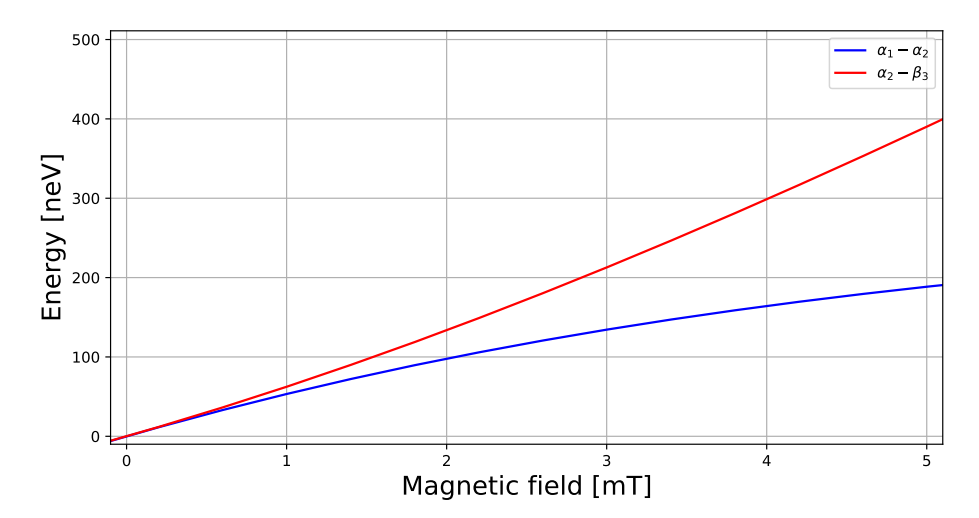


FIGURE 4.3: Sona transition energy as function of the longitudinal magnetic field. For increasing magnetic fields, the energy of the  $\Delta E_{\alpha_1,\alpha_2}$  transition (blue curve) is approaching a constant value, while the energy of the  $\beta_3 \to \alpha_2$  transition (red curve) becomes a linear function.

### 4.2.1 Search for the Peak Positions

To calculate the position of the peak centers, the simplified assumption is made that in first order, the resonance peaks inside a Sona spectra follow a Lorentz-like function. Thus a simple Lorentz function is fitted on each peak to get the corresponding measurement time of the peak center. For most of the peaks, this method works quite well, Figure 4.4 and Figure 4.5 show exemplary the method applied to both Sona spectra measured in the measurement series 'E1270'. However, for some peaks, the method shows some differences between data and fit. Some peaks are deformed at their center or their flanks, while others are not, due to the interaction between the different hyperfine substates inside the Sona transition unit. The more a peak is deformed, the greater is the uncertainty in the calculated position of the peak center. This can be observed particularly well in the peaks in the middle of the  $\alpha_1$  spectrum. Another point that is only partially taken into account is that the measured spectra are superimposed with an offset function. For the  $\alpha_1$  spectrum, this seems to be a non-linear increasing offset, while for the  $\alpha_2$ -spectra the offset seems to be much more complex. To compensate this background effect, the fit function is allowed to assume an individual constant offset for each peak. In this way, the center of most peaks should still be fairly well determined.

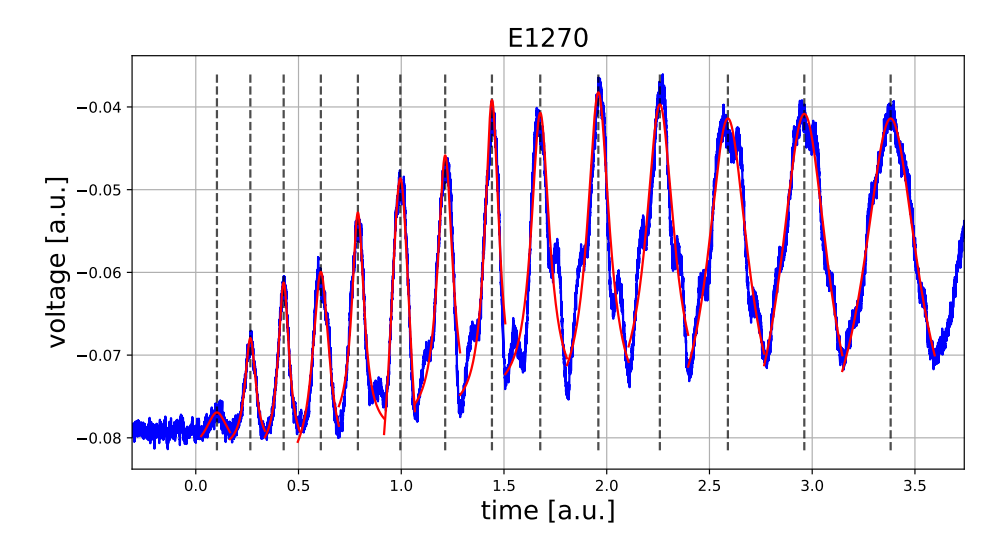


Figure 4.4: Lorentz curves fitted on the measured  $\alpha_1$  spectrum of the 'E1270' measurement series. Data in blue, fitted Lorenz curves in red.

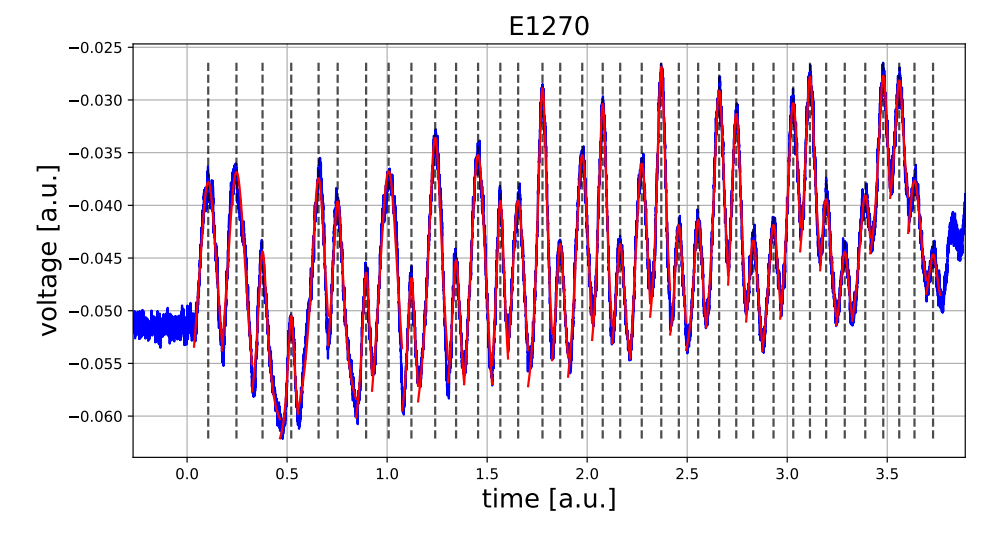


FIGURE 4.5: Lorentz curves fitted on the measured  $\alpha_2$  spectrum of the 'E1270' measurement series. Data in blue, fitted Lorenz curves in red

## 4.2.2 Fits to the Breit-Rabi Transition Energies

With the calculated peak positions as a function of the measured time and the assumed transition energies in multiples of  $\Delta E_{Sona}$ , at each peak, one gets a distribution of data points that matches the shape of the transition energies  $\Delta E_{\alpha_1,\alpha_2}$  and  $\Delta E_{\alpha_2,\beta_2}$ . However, to directly compare the generated data points with Equation 4.1 and Equation 4.2 one needs to rescale them. To accomplish that, two fit functions are introduced

$$N_{\alpha_1 - \alpha_2}(t) = \mathbf{A} \left( \frac{\Delta E_{HFS,0}}{2} + d_1 \left( 1 + \eta_1 \right) - \frac{\Delta E_{HFS,0}}{2} \sqrt{1 + c_2 (1 + \delta_2) \frac{\mu_B (\mathbf{B_{sca}} t + \mathbf{B_{off}})^2}{\Delta E_{HFS,0}}} \right)$$
(4.3)

$$N_{\alpha_2 - \beta_3}(t) = -\mathbf{A} \left( \frac{\Delta E_{HFS,0}}{2} + d_1 (1 + \eta_1) + \frac{\Delta E_{HFS,0}}{2} \sqrt{1 + c_2 (1 + \delta_2) \frac{\mu_B (\mathbf{B_{sca}} t + \mathbf{B_{off}})^2}{\Delta E_{HFS,0}}} \right)$$
(4.4)

Here, t is the measured time, N is the Nth multiple of  $\Delta E_{Sona}$ ,  $\mathbf{A}$  is the scaling parameter of the energy, which in theory should be  $\frac{1}{\Delta E_{Sona}}$ ,  $\mathbf{B_{sca}}$  is the scaling parameter of the magnetic field, giving the relation between measured time and  $B_{av}$ , and  $\mathbf{B_{off}}$  is the magnetic field offset created by external fields, i.e. the stray fields of the spin filter and the earth field. Figure 4.6 and Figure 4.9 shows exemplary the result of applying the appropriate fitting functions to the data of measurement series 'E1270' using the least squares method. Figure 4.7 and Figure 4.10 show the corresponding residuals. The analysis for the other measurement series showed similar behavior. The calculated fit parameter for all measurement series can be found in Appendix C.

Based on the plots, a few things can now be determined. First, the distribution of the data points, generated from the position of the peak centers in the two  $\alpha$  spectra, fit the shapes of the transition energy curves very well and for each transition energy curve a fit can be found. However, the fits do not agree with each other. Looking at Figure 4.6 and Figure 4.9, one can see that only for the energy transition curve whose fit parameters were used, the curve fits the data. This becomes especially clear when looking at the residuals in Figure 4.7 and Figure 4.10, where the measured data points of the transition whose fit parameters were not used run away linearly with increasing measurement time. Comparing the fit parameter of the different transitions directly, one finds that only the calculated fit parameters of the  $\alpha_1 - \alpha_2$  transition fits are in the range of the expected Sona energy. As pointed out above, using the relation  $\mathbf{A} = \frac{1}{\Delta E_{Sona}}$ , the fitting parameter  $\mathbf{A}$  can be used to calculate  $\Delta E_{Sona}$ . For the "E1270" measurement series, assuming that the kinetic energy of the particles was 1.270 keV and the  $\lambda$  of the Sona transition field was approximately 27 cm, a Sona energy of  $\Delta E_{Sona} \approx 7.56 \,\text{eV}$  is expected. However, the fit for the  $\alpha_2 - \beta_3$  transition delivers a result of  $6.2 \pm 0.5 \,\mathrm{neV}$ , while the fit for the  $\alpha_1 - \alpha_2$  transition delivers a

value of  $7.44 \pm 0.05$  neV. Why the results for the two transitions differ so much and only roughly fit the expected value has not yet been determined and needs further investigation.

Another mayor point that needs to be discussed is that the calculated uncertainties for each data point seems to be too to small. Considering Figure 4.8 and Figure 4.11, which show only the residuals for the transition after which was fitted, it becomes apparent that the data points do not match the fits within the scope of their uncertainties. The uncertainties given here are only defined by the uncertainties on the calculated peak positions in the respective  $\alpha$  spectra. Moreover, the spread of the residuals of the  $\alpha_1 - \alpha_2$  transition is generally always an order of magnitude smaller than that of the  $\alpha_2 - \beta_3$  transition. In total, for the  $\alpha_2 - \beta_3$  transition, the data points deviate at most in the order of  $0.3 \times \Delta E_{Sona}$  ( $\approx 1.5 \, \mathrm{neV}$ ), while for the  $\alpha_1 - \alpha_2$  they always deviate below  $0.1 \times \Delta E_{Sona}$  ( $\approx 0.7 \, \mathrm{neV}$ ). In general, it appears that the uncertainties of the individual data points are far too small.

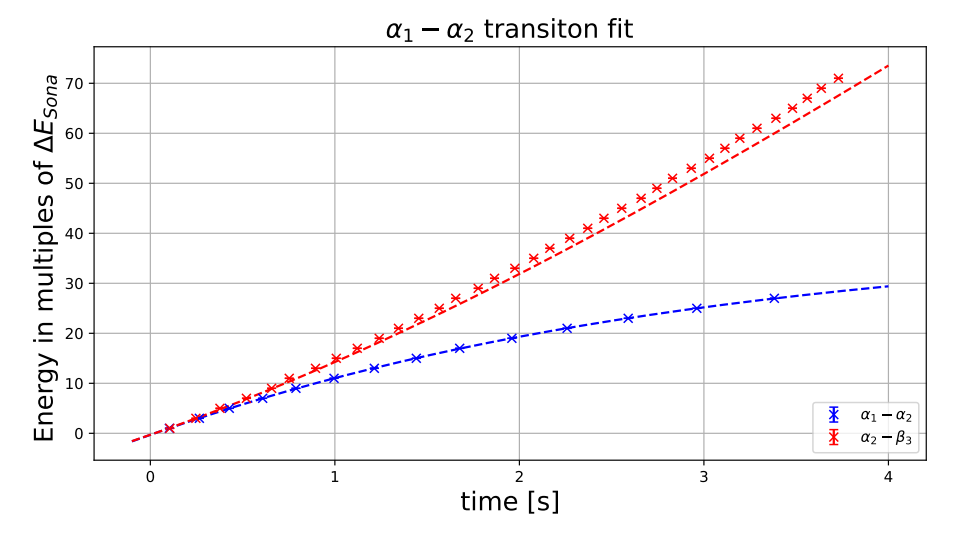


FIGURE 4.6: Plot of the measured data points and fit functions using the parameters of the  $\alpha_1-\alpha_2$  transition fit of the measurement series 'E1270'. Blue:  $(\alpha_1-\alpha_2)$ , red:  $(\alpha_2-\beta_3)$ , the x-marker show the data points, the dashed lines (--) show Equation 4.1 and Equation 4.2 using the parameters of the  $\alpha_1-\alpha_2$  fit.

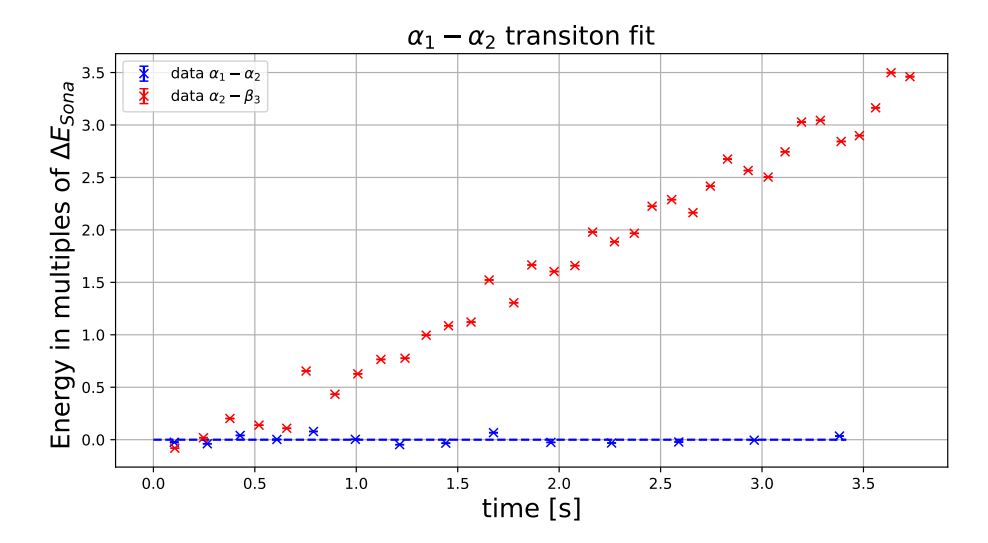


Figure 4.7: Residuals of the  $\alpha_1-\alpha_2$  transition energy fits of the measurement series 'E1270'.

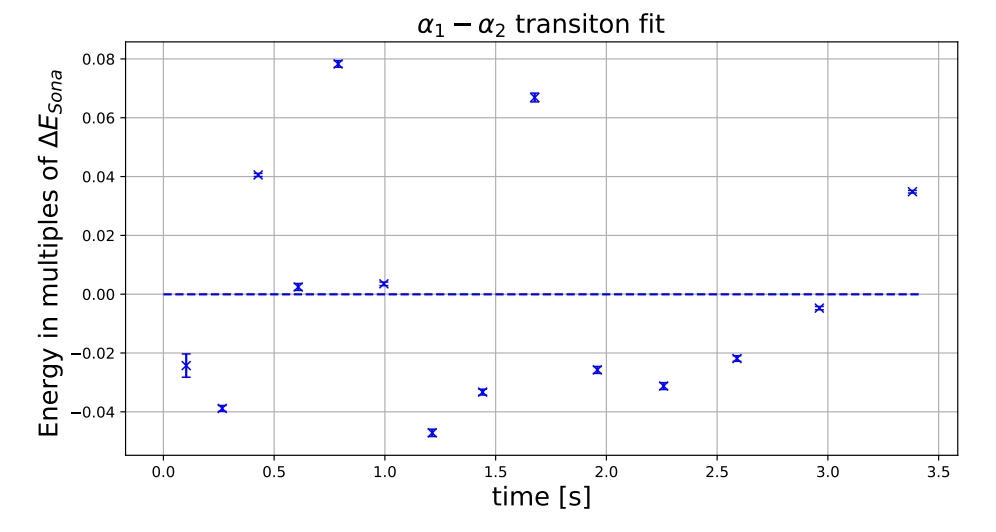


Figure 4.8: Residuals of the  $\alpha_1 - \alpha_2$  transition energy fits of the measurement series 'E1270' (only  $\alpha_1 - \alpha_2$ ).

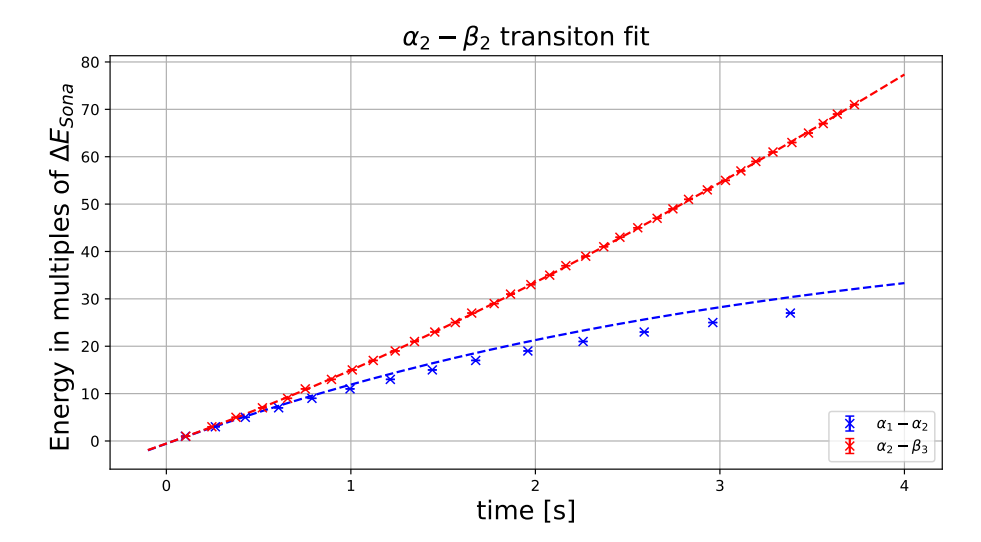


FIGURE 4.9: Plot of the measured data points and fit functions using the parameters of the  $\alpha_1-\alpha_2$  transition fit of the measurement series 'E1270'. Blue:  $(\alpha_1-\alpha_2)$ , red:  $(\alpha_2-\beta_3)$ , the x-marker show the data points, the dashed lines (- -) show Equation 4.1 and Equation 4.2 while using the parameters of the  $\alpha_2-\beta_3$  fit.

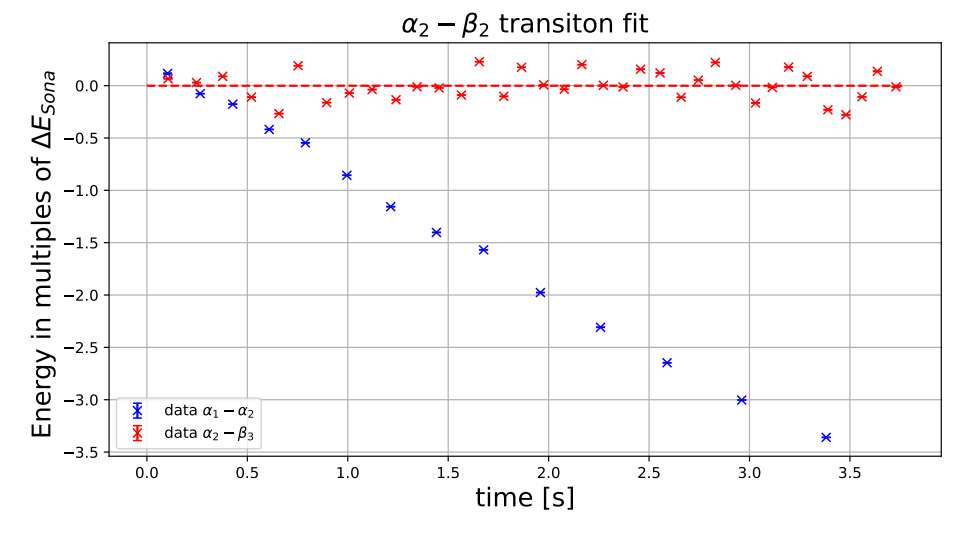


Figure 4.10: Residuals of the  $\alpha_2 - \beta_3$  transition energy fits of the measurement series 'E1270'.

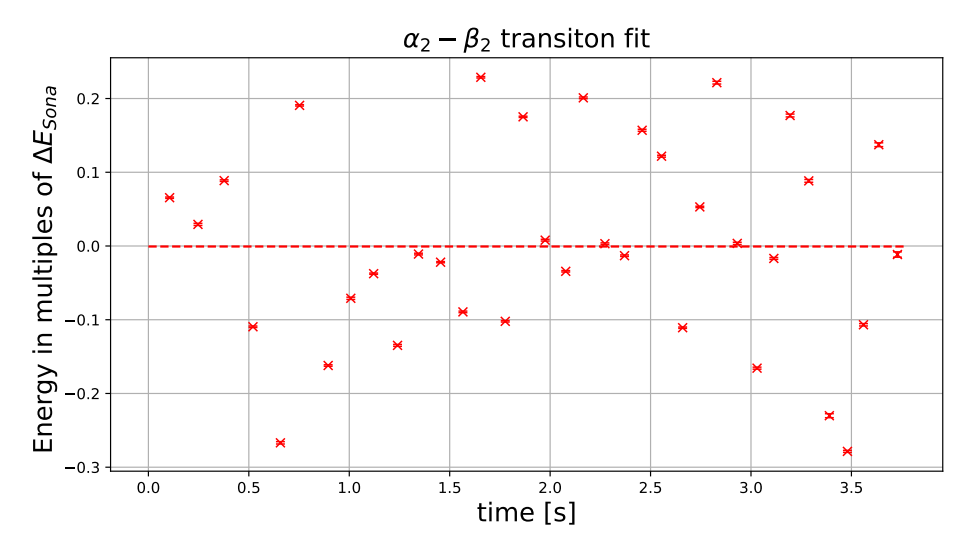


Figure 4.11: Residuals of the  $\alpha_2-\beta_3$  transition energy fits of the measurement series 'E1270' (only  $\alpha_2-\beta_3$ ).

## 4.3 Comparison of the Measurements Series

Since all the series of measurements were performed with the same experimental setup, in particular with the same Sona setup, the fits should give the same magnetic fit parameters  $\mathbf{B_{sca}}$  and  $\mathbf{B_{off}}$  for each of the measurement series, regardless of the kinetic energy chosen in the ECR source. Furthermore, since  $\Delta E_{Sona}$  is a function of the kinetic energy of the beam  $E_{kin}$ , and again using the fact that the Sona setup is always the same, one can derive the following relation

$$\Delta E_{Sona} = \frac{h}{\lambda} \sqrt{\frac{2E_{kin}}{m_p}} \ . \tag{4.5}$$

Again using the relation  $\mathbf{A} = \frac{1}{\Delta E_{Sona}}$ , one can calculate  $\lambda$  of the Sona transition unit by plotting the calculated  $\Delta E_{Sona}$  as a function of the different kinetic energies and using Equation 4.5 as fit function with  $\lambda$  as the only free parameter. Figure 4.12 shows the result of this fit, with Figure 4.13 showing a close-up of the area of interest. Figure 4.14, and Figure 4.15 show the magnetic fit parameters of each measurement series as a function of  $E_{kin}$ . Table 4.1 lists the averages for the magnetic parameters and the calculated  $\lambda$  for all measurements for each transition, respectively.

Looking at the plots and the values for the fit parameters in Appendix A, it becomes apparent that over all measurement series, the result for each transition on its own are consistent. However, the results of the transitions do not agree with each other. Looking at Table 4.1, one can see that for all three fit parameters, the results diverge by a multiple of the calculated uncertainties. Furthermore, only the calculated  $\lambda$  of the  $\alpha_1 - \alpha_2$  transition is roughly in the area of the expected  $\lambda = 27$  cm. Moreover, the uncertainties of the  $\alpha_1 - \alpha_2$  transition for all parameters are again much smaller than those of the  $\alpha_2 - \beta_3$  transition. A discussion of the possible reasons explaining all these discrepancies can be found in chapter 5.

TABLE 4.1: List of the magnetic fit parameter and the calculated  $\lambda$  of the Sona transition unit for both transitions.

transition	$\lambda$ [cm]	$B_{sca} [\mathrm{mT  s^{-1}}]$	$B_{off}$ [mT]
$\alpha_1 - \alpha_2$	$27.30 \pm 0.05$	$1.69 \pm 0.01$	$-0.061 \pm 0.002$
$\alpha_2 - \beta_3$	$33.8 \pm 0.5$	$1.47 \pm 0.03$	$-0.049 \pm 0.003$

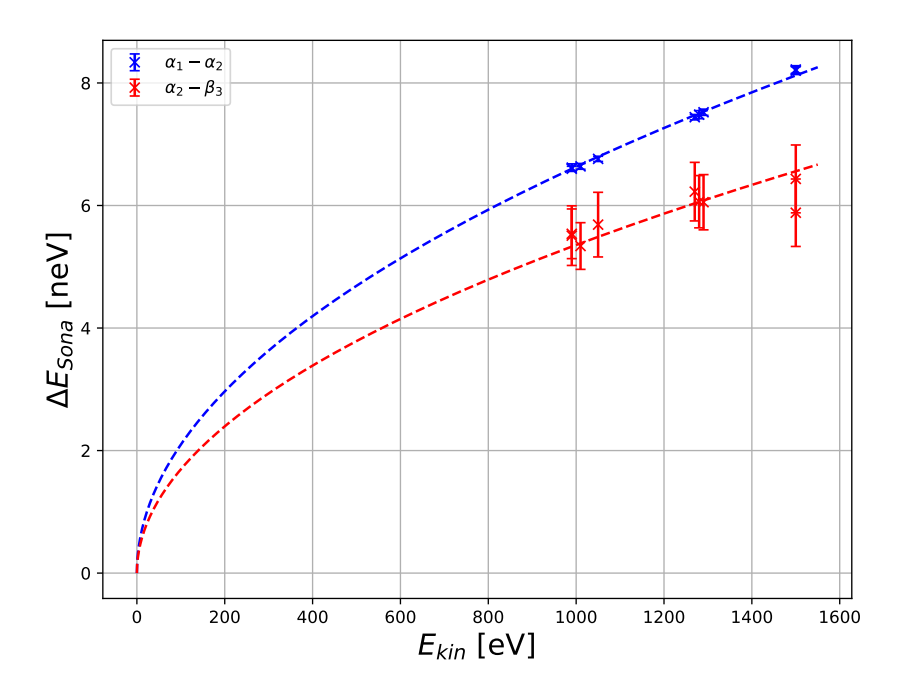


FIGURE 4.12: Energy of the basic photon energy  $\Delta E_{Sona}$  as function of  $E_{kin}$  for all measurement series.  $\alpha_1 - \alpha_2$  transition in blue,  $\alpha_2 - \beta_3$  transition in red. The dashed lines (--) show the fit for relation between  $\Delta E_{Sona}$  and  $E_{kin}$  for each transition.

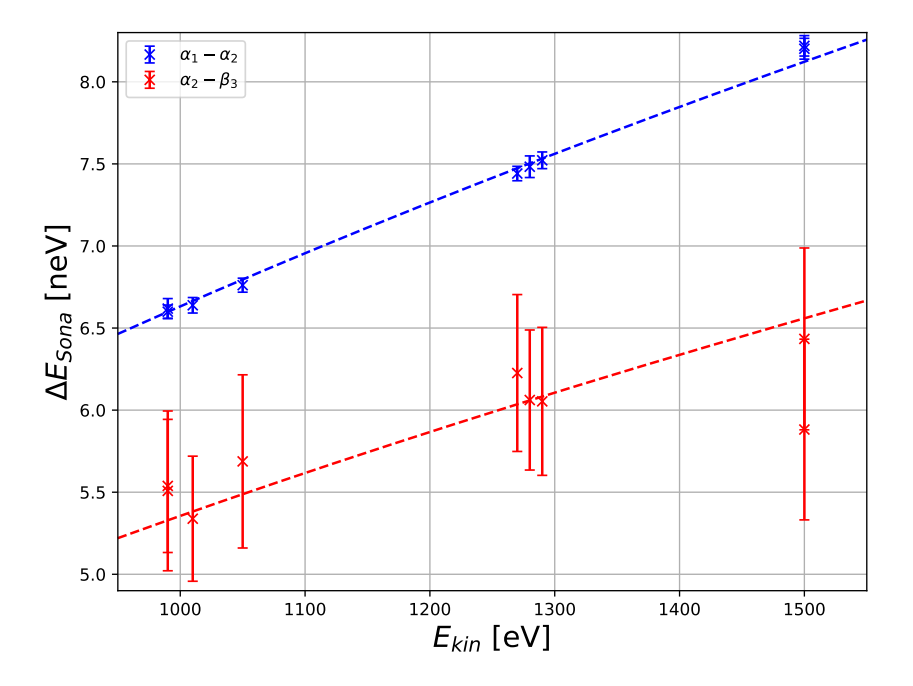


FIGURE 4.13: Energy of the basic photon energy  $\Delta E_{Sona}$  as function of  $E_{kin}$  for all measurement series (Zoom).  $\alpha_1 - \alpha_2$  transition in blue,  $\alpha_2 - \beta_3$  transition in red. The dashed lines (--) show the fit for relation between  $\Delta E_{Sona}$  and  $E_{kin}$  for each transition.

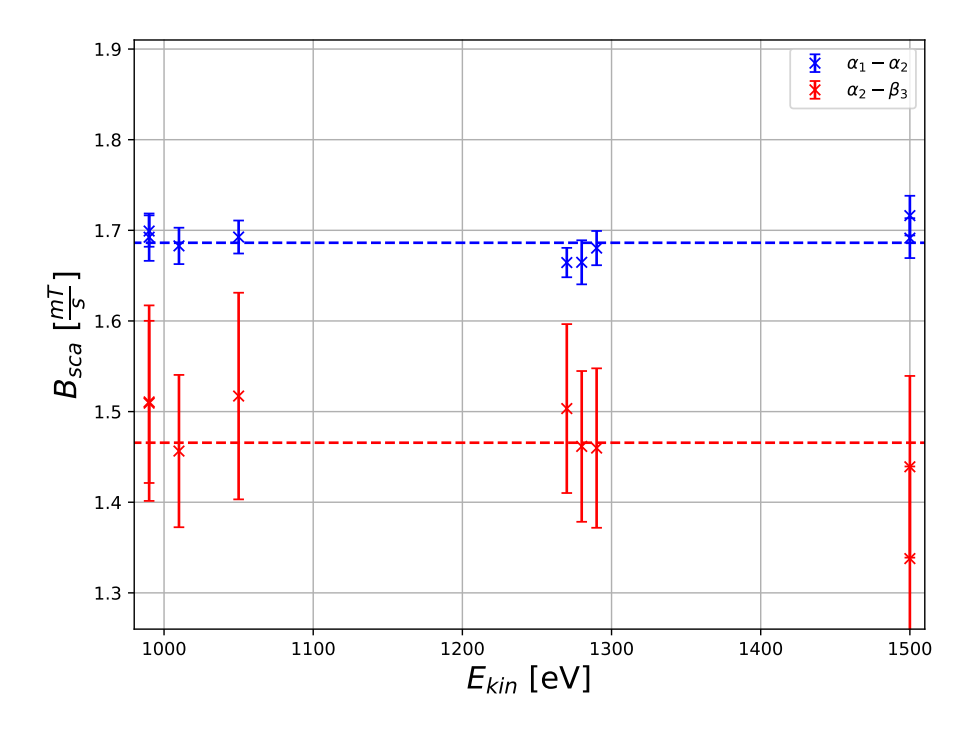


FIGURE 4.14: Magnetic scaling parameter  $\mathbf{B_{sca}}$  as function of  $E_{kin}$  for all measurement series.  $\alpha_1 - \alpha_2$  transition in blue,  $\alpha_2 - \beta_3$  transition in red. The dashed lines (--) are the average values for each transition.

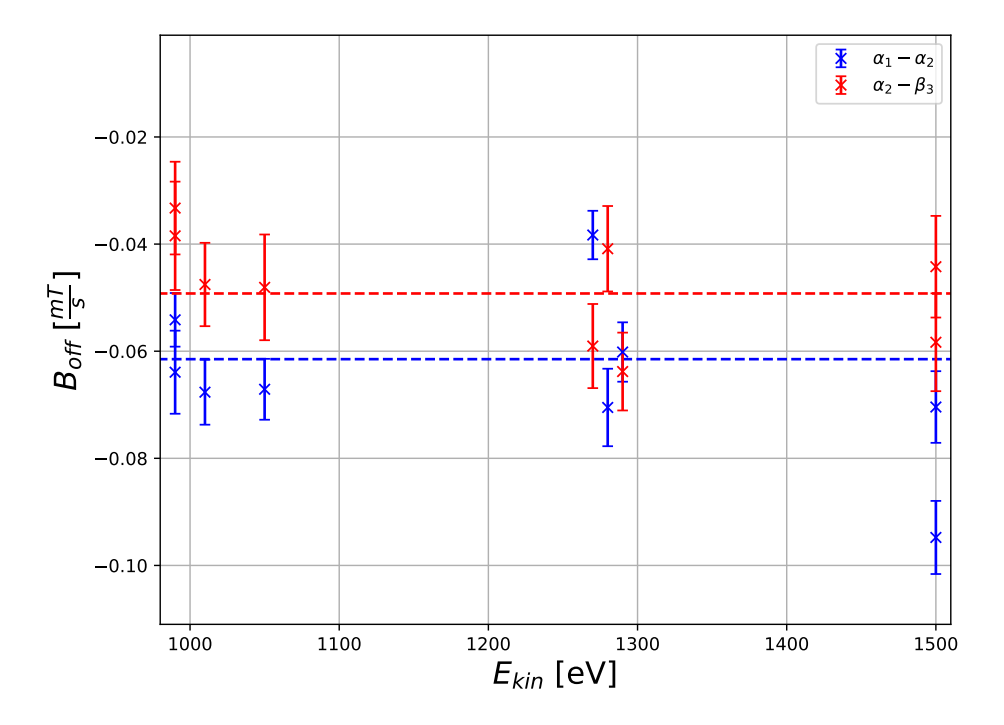


FIGURE 4.15: Magnetic offset parameter  $\mathbf{B_{off}}$  as function of  $E_{kin}$  for all measurement series.  $\alpha_1 - \alpha_2$  transition in blue,  $\alpha_2 - \beta_3$  transition in red. The dashed lines (--) are the average values for each transition.

## Chapter 5

# Conclusions and Outlook

## 5.1 Conclusions

As far as the first goal of this thesis is concerned, it looks like that the experiment presented in chapter 3 is generally suitable for measuring oscillations between occupation numbers of the different hyperfine substates of metastable  $2S_{1/2}$  hydrogen. For a variety of kinetic energies of the hydrogen atoms, the oscillations induced by the Sona transition units were recorded. Thereby, the signal strength of the recorded spectra even reached much higher values than in previous experiments. However, while performing the measurements, it became apparent that the setup has a series of issues that negatively influenced the data taking. Firstly, it was discovered that the shielding of the Sona transition unit is not sufficient and thereby the stray fields of the second spin filter are influencing the shape of the magnetic field inside the Sona transition unit. Secondly, the ECR source does not work properly. Only for short periods of time, a stable plasma beam could be produced, which limited the amount of data that could be taken.

With regard to the second goal of this thesis, the situation is more complicated. The here presented analysis is not able to reach the small energy uncertainties of less than  $10^{-11}$  eV that are needed to verify the QED corrections, although the fits for the  $\alpha_1 - \alpha_2$  transition came close to this value and reached uncertainties of multiples of  $10^{-11}$  eV. Moreover, the analysis of the measured data provides different sets of parameters for the two transitions, which physically cannot be. The question therefore arises whether the method of analysis is generally not accurate enough and therefore not suitable, or whether there was an undetected problem with the data taking. During the measurements and analysis, the following things were noticed that could explain some discrepancies:

#### Search for the positions of the peak centers:

One problem of the fitting method seems to be the search for the positions of the peak centers. The residual plots of the individual fits for each measurement series shown in subsection 4.2.2 suggest that in search for the position of the peak centers, simple Lorentz fits are not accurate enough. From the beginning, it was already clear that the Lorentz curve is only an oversimplified approximation for the shape of the peaks. Due to the interference of the transitions, e.g. the  $\alpha_1 - \alpha_2$  transition can only happen, if  $\alpha_2$  state is populated (see. section 2.4), the peaks are systematically deformed. As a result, the calculated positions of the peak centers should be shifted compared to their true positions. This systematic effect should have a much stronger influence on the  $\alpha_2 - \beta_3$  transition analysis, due to the small width of the peaks in the  $\alpha_2$  spectrum. This, in turn, could explain why the uncertainties of the fitting parameters of the  $\alpha_2 - \beta_3$  transition are so large compared to their spread around the average values (see figures in section 4.3).

### Spin filter stray fields:

Another point are the stray fields of the spin filter. As pointed out in subsection 3.7.2, if the magnetic field of the second spin filter is increased from 53.5 mT to 60.5 mT, the shape of the magnetic field changes and with it the  $\lambda$  of the Sona transition is modified as well. This means that depending on whether the  $\alpha_1$  or  $\alpha_2$  spectrum is measured, different  $\Delta E_{Sona}$  can be expected for the same kinetic energy of the particles. However, the resulting change in  $\lambda$  is likely to be only of the order of 0.2% and therefore cannot explain the large discrepancy of 20% resulting from the analysis. Looking at Figure 3.11, we see that the stray fields also produce an additional magnetic offset, which has an average value of about 20 mT. This value in turn is of the same order of magnitude as the difference between the two calculated magnetic offset parameters  $\mathbf{B}_{\text{off}}$  (see Figure 4.15).

### Correlation of the fit parameters:

An additional problem of the fit method is that the fit parameter **A** and  $\mathbf{B_{sca}}$  are correlated. Up to a certain point, increasing **A** and decreasing  $\mathbf{B_{sca}}$  results in a similar fitting curve. However, for the  $\alpha_2 - \beta_3$  transition, since the function becomes more and more straight with increasing magnetic fields, the correlation is rather strong, while for the  $\alpha_1 - \alpha_2$  transition, the correlations is much weaker due to the slope of the  $\alpha_1 - \alpha_2$  transition energy function. This could explain, why the uncertainties of the  $\alpha_2 - \beta_3$  transition fit parameters are always much bigger than the ones of the  $\alpha_1 - \alpha_2$  transition.

### Possible non linearity between measured time and magnetic field:

Another explanation for the discrepancies between the two transitions could be a non-linearly increasing magnetic field as a function of the measured time t. For the analysis, it was assumed that the relationship between t and the longitudinal magnetic field inside the Sona transition unit was linear. In preparatory measurements, it was tested that the ramp generator produces an almost perfectly linear voltage as a function of the measured time. The relationship between the current of the Sona coil and the magnetic field strength was also found to be almost perfectly linear. However, it was not tested whether the output current of the power supply feeding the Sona coils was a linear function of the

5.2. Outlook 59

control signal supplied by the ramp generator. Therefore, a nonlinearity may have occurred at this point, which is currently being investigated.

Nevertheless, the calculated data points, consisting of the position of the peak center and the corresponding multiples of  $\Delta E_{Sona}$ , follow clearly the transition energy functions calculated with the Brei-Rabi formula. For the  $\alpha_1 - \alpha_2$  transition, the fitting method is able to deliver fits which match the measured data within very small uncertainties, which shows the potential of this experiment. However, it still has to be investigated why the results for the  $\alpha_2 - \beta_3$  transition fits are so far away from the expected values and why they disagree with the calculated parameters of  $\alpha_1 - \alpha_2$  transition (see figures in section 4.3). In particular, it needs to be determined whether this is caused by the analysis method or by unknown systematics within the experiment that have not yet been discovered. The latter seems to be more likely at this point, since this systematics did not appear in earlier measurements (cf. [8] and [18]), and the old analysis method is also unable to provide a reasonable solution. Therefore, it is very important to perform further measurements with this setup, on the one hand to obtain more data for better statistics, and on the other hand to determine if there is indeed an unknown systematic, and if so, what causes it.

## 5.2 Outlook

A series of improvements to the experimental setup are foreseen for the future or undergoing at the moment. As already mentioned in subsection 3.7.1, the high voltage connections of the ECR ion source are now going to be connected correctly, so that for future measurement runs a well shaped hydrogen beam with an even higher intensity can be expected. Also the shielding of the Sona transition unit is going to be improved so that the stray fields of the spin filters will no longer influence the magnetic field inside the Sona transition unit, so that the basic transition energy  $\Delta E_{Sona}$  is the same for all spectra.

Moreover, for the near future, a redesign of the Sona transition unit is foreseen. The coils of this new Sona transition unit will be arranged in a way that the resulting shape of the magnetic field comes as close as possible to the shape of a sine-function. In that way, it should be possible to calculate the resulting wavelength  $\lambda$  in advance with a relative uncertainty of  $10^{-3}$ , and the measured spectra can be directly compared to simulations. Furthermore, a spin filter with a complete new design is in preparation. This new spin filter will provide the ability to use two radiofrequencies. With this, not only the two  $\alpha$ -states can be measured, but the  $\beta$  states as well, so that all three for this experiment relevant substate spectra can be investigated.

Another thing which can be investigated, which is already possible with the current setup, is to measure the combined signal of both  $\alpha$  states. By switching off the radiofrequency in the second spin filter, the  $\alpha$  and e states are no longer coupled. This allows both  $\alpha$  states to be transmitted into the quench chamber. This could be one way to get a simpler spectrum which is free of the interactions between the two

 $\alpha$  states, because the atoms in the  $\beta_3$  state will move into a superposition of the  $\alpha_1$  and  $\alpha_2$  state.

In terms of the analysis, new methods to find the peak positions are under investigation. One possible approach could be to fit the measured spectra in combination which each other, using rate equations generated from numerical simulations. There is hope that this approach will lead to better results, because it is intended to account for the interaction between the different states. A working analysis method should allow performing spectroscopy of metastable hydrogen with uncertainties in the range of less than  $10^{-11}$  eV.

## Appendix A

## Breit Rabi formula Coefficients

Table A.1 lists the numerical values of the Breit-Rabi formula coefficients of hydrogen for the  $2S_{1/2}$ - and  $2P_{1/2}$ -state, taken from [38].

Atom	$H_1^1(1S_{1/2}) / H_1^1(2S_{1/2})$	$H_1^1(2P_{1/2})$
$g_j$	2.002310441392(22)	0.6651585(46)
$\langle r^2 \rangle^{1/2}$	0.879(9) fm	0.879(9) fm
Ι	1/2	1/2
$\epsilon_2 \ (= \eta_2)$	$2.62894 \cdot 10^5$	$-2.50741(2) \cdot 10^9$
$c_2$	4.02143867224(16)	0.446492(6)
$\delta_2$	-0.00000001346	-0.001348954(10)
$c_2(1+\delta_2)$	4.02143861810(16)	0.445890(6)
$d_1$	0.99963418853(2)	0.331058(2)
$\eta_1$	0.000000006752	0.000680675(5)
$d_1(1+\eta_1)$	0.99963419528(2)	0.331284(2)

Table A.1: Numerical values of the Breit-Rabi formula coefficients of hydrogen.

## Appendix B

# Photos of the Experimental Setup

In the following, photos of the experimental setup that is located in a laboratory at the Institut für Kernphysik at the Forschungszentrum Jülich is presented.

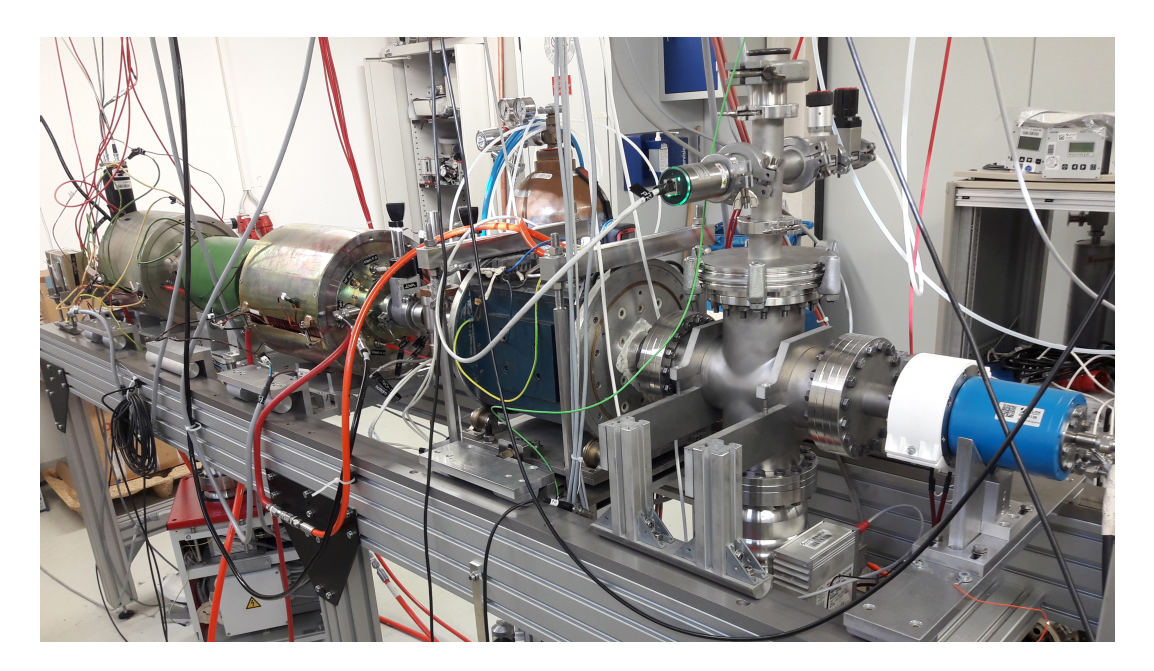


Figure B.1: Photo of the complete experimental setup.

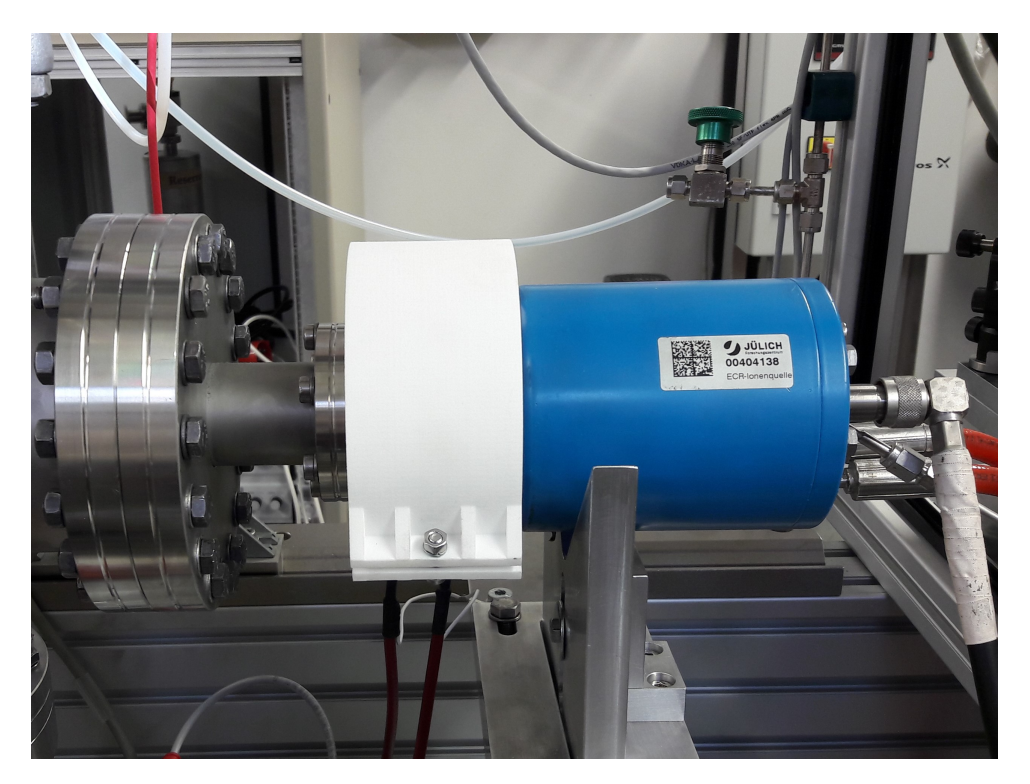


Figure B.2: Photo of the ECR ion source. On the right side, one can see the radiofrequency, water and hydrogen connection lines. On the left side starts the cross connection tube.

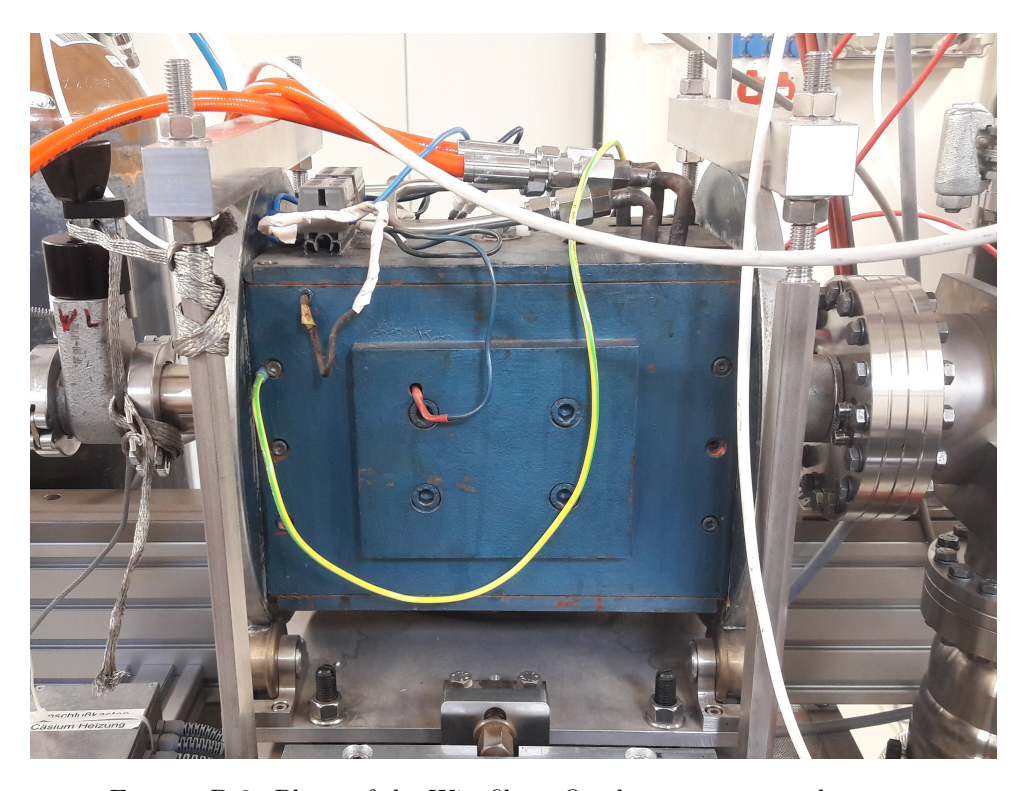


Figure B.3: Photo of the Wienfilter. On the top, one sees the water connection line. On the right side ends the cross connection tube. On the left side, the first valve of the cesium cell is visible.

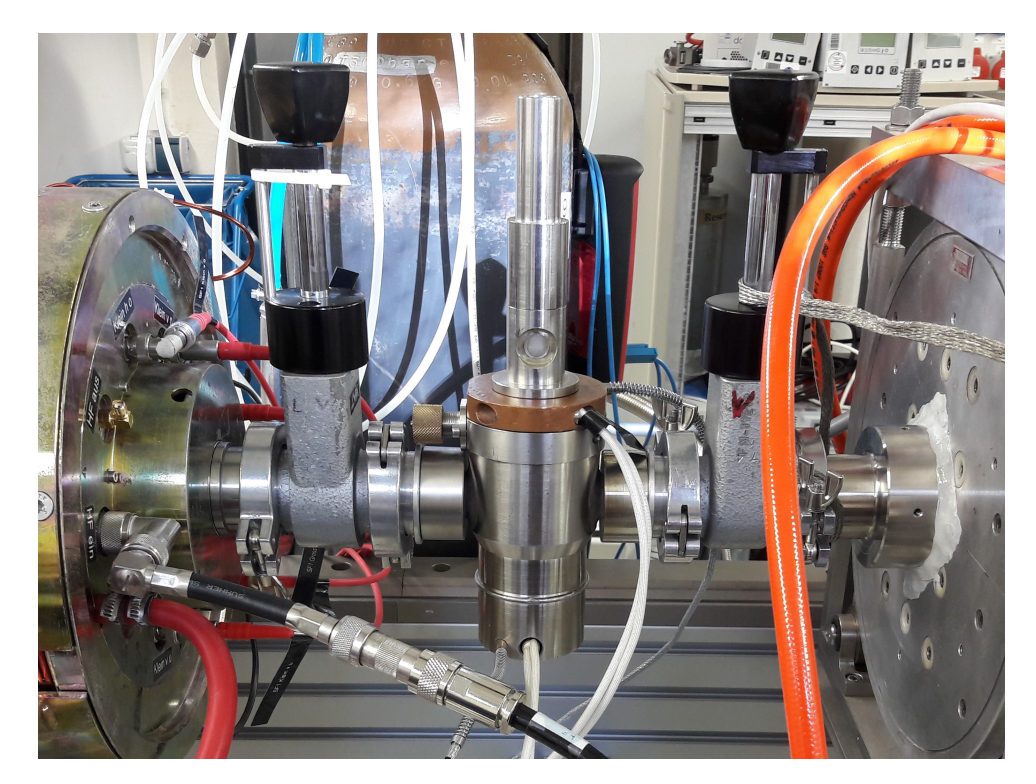


FIGURE B.4: Photo of the cesium cell. Attached to each side is a valve. On the left side starts the first spin filter. On the right side ends the Wienfilter.

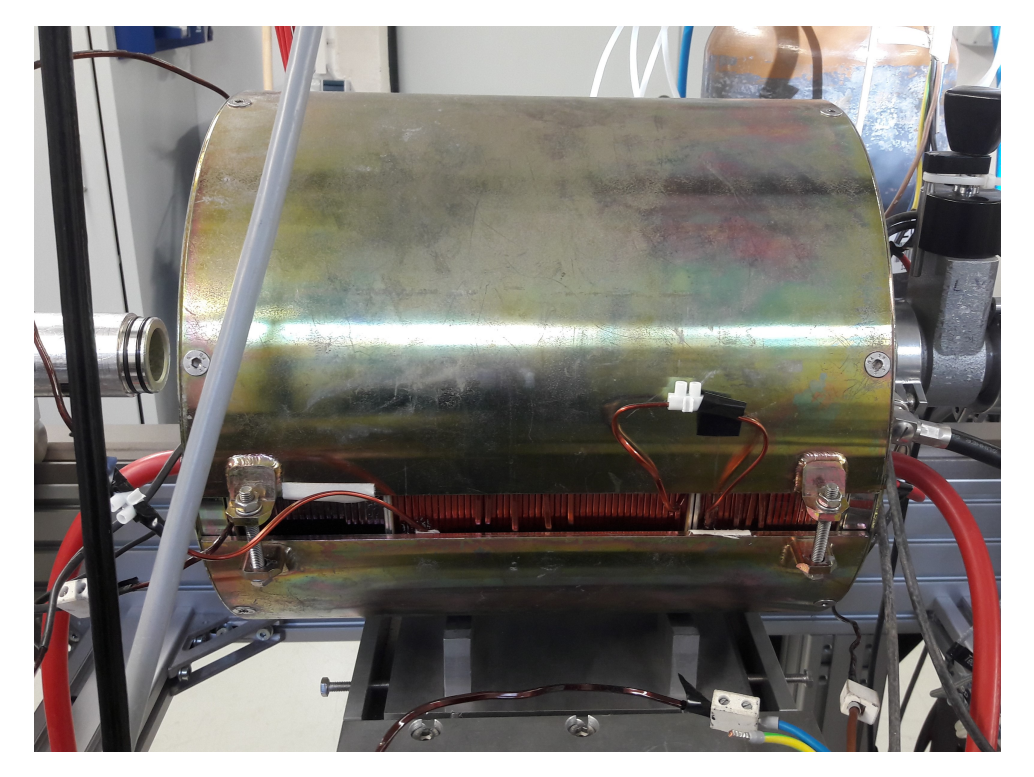


FIGURE B.5: Photo of the first spin filter. On the right side, the second valve of the cesium cell is visible. On the left side, one can see the connection pipe that leads to the Sona transition unit (Here it is disconnected).

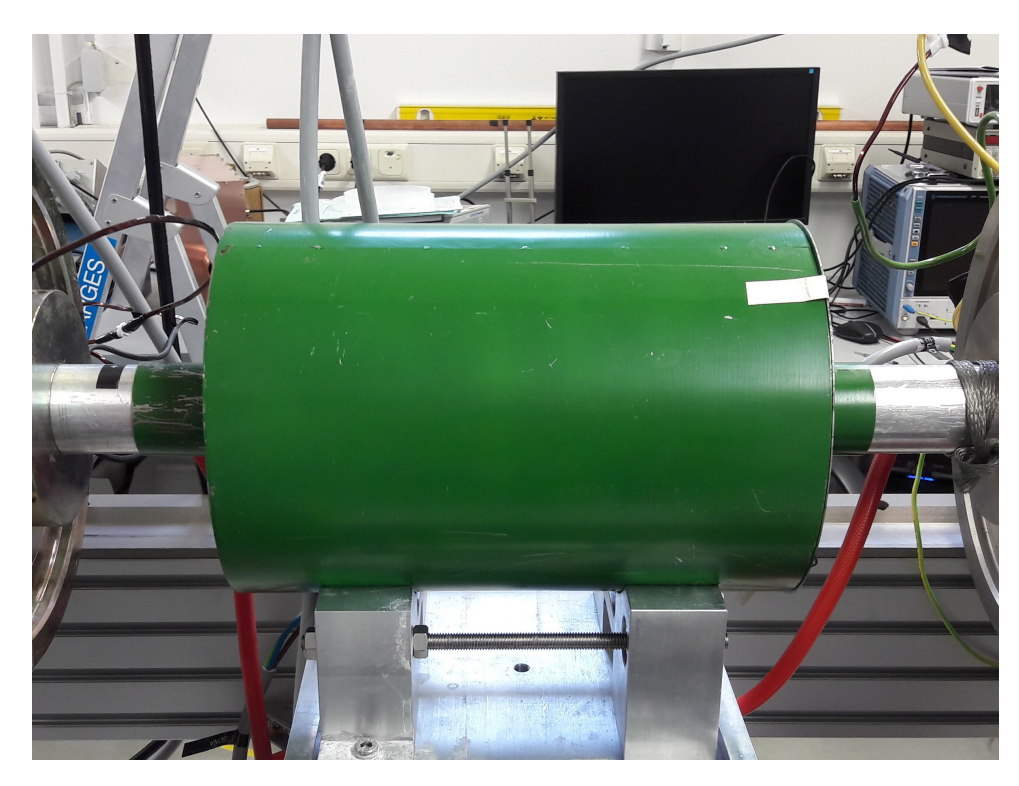


FIGURE B.6: Photo of the Sona transition unit. On both sides, the spin fitlers are visible.

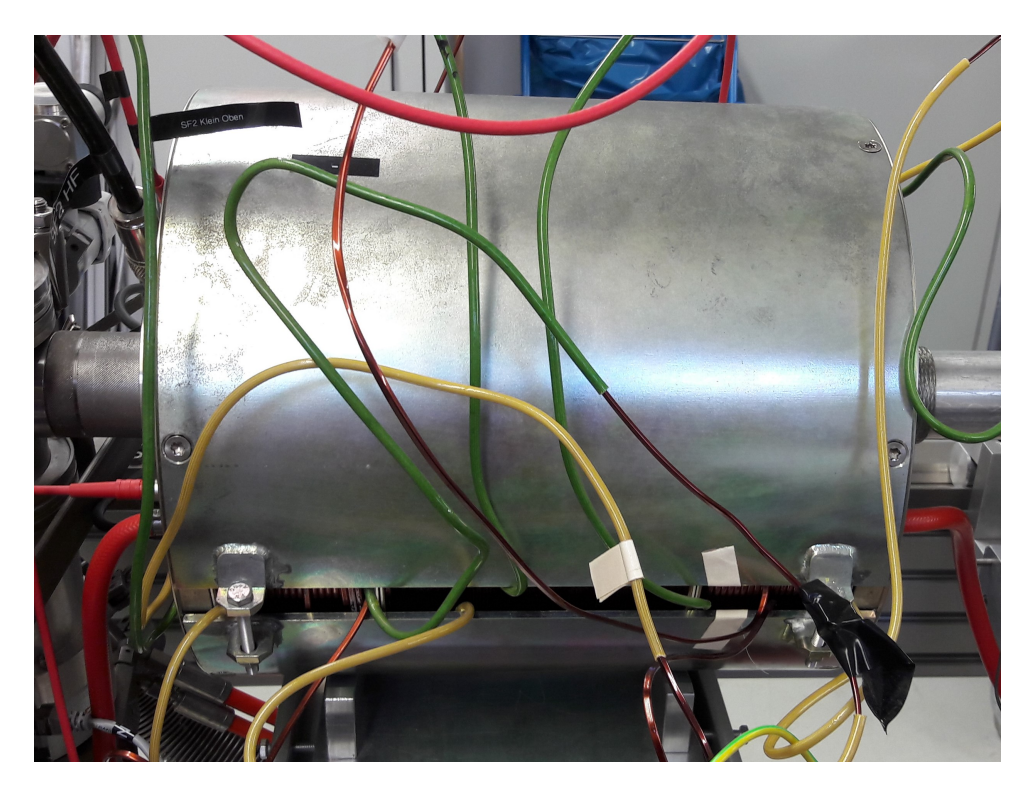


FIGURE B.7: Photo of the second spin filter. On the right side, the connection pipe that leads to the Sona transition is visible. On the left side starts the quench chamber.

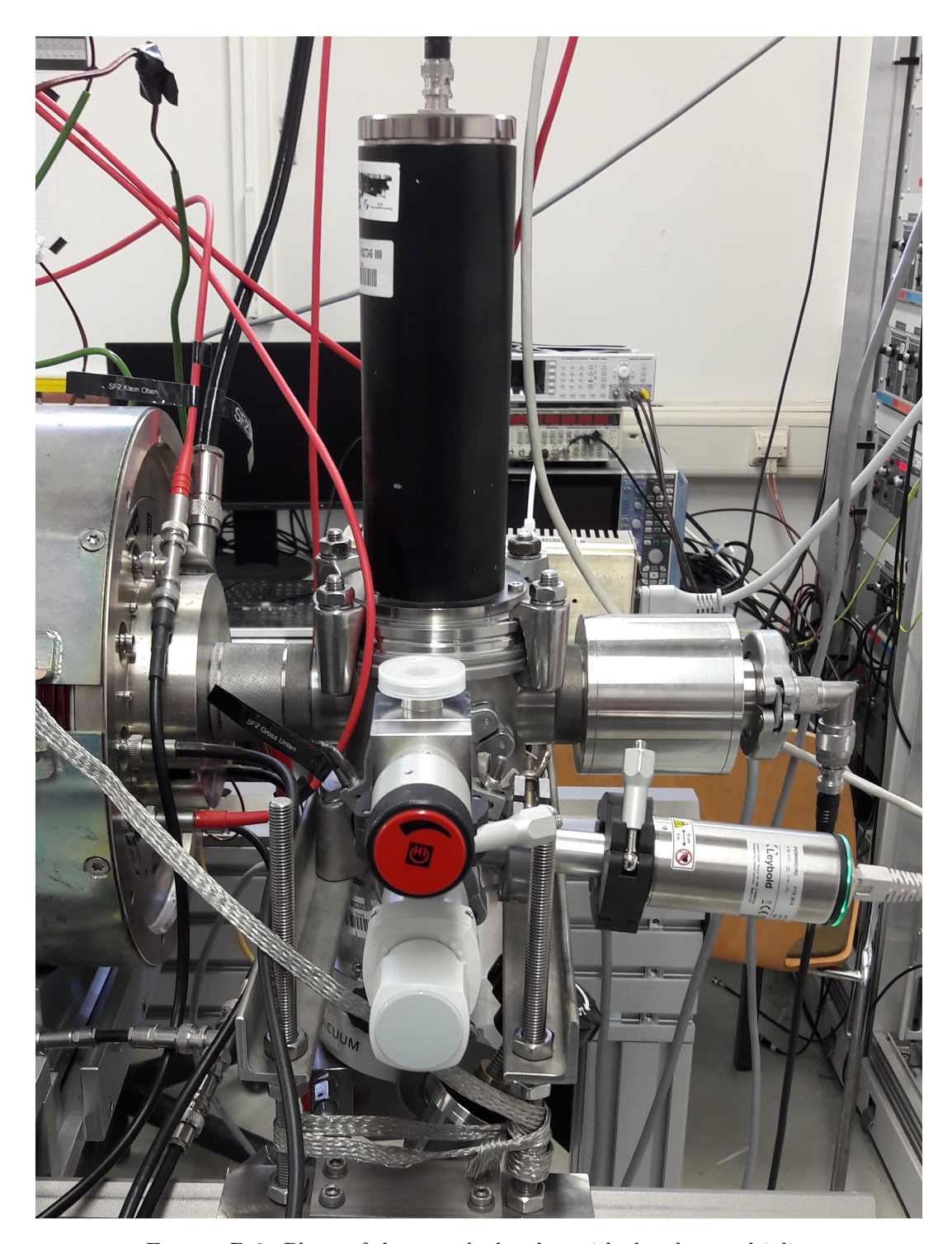


FIGURE B.8: Photo of the quench chamber with the photomultiplier tube on top. In the center right, the Faraday cup is visible. In front of the quench chamber a ventilation valve and a pressure gauge can be seen.

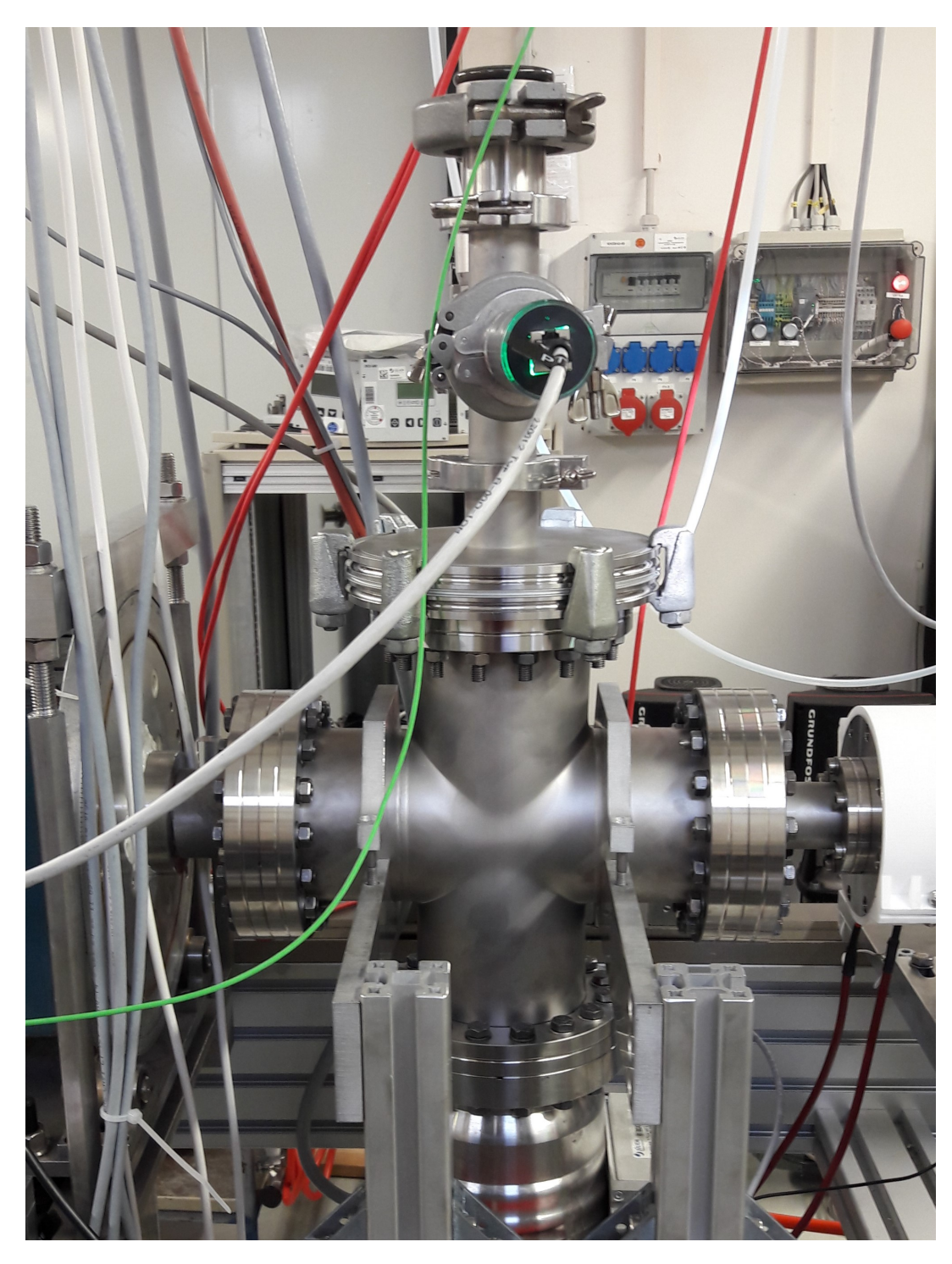


FIGURE B.9: Photo of the cross connection between ECR and Wienfilter, with a viewing window and a pressure gauge on top. On the bottom, a turbo molecular pump is mounted.

### Appendix C

# Listing of the Measurement and Fit Parameters

#### C.1 Listing of the Measurement Parameters

Twelve different measurement series were recorded. The beam energies<sup>1</sup> were between 0.99 keV and 1.5 keV. Only for eight measurement series, both spectra could be recorded. The wavelength of the Sona transition unit was assumed to be  $\lambda = 27$  cm.

Table C.1: List of the measurement series.

measurement series	kin. Energy [neV]	expected $\Delta E_{Sona}$ [neV]	recorded Spectra
E990_1	990	6.67	$\alpha_1 \& \alpha_2$
E990_2	990	6.67	$\alpha_1 \& \alpha_2$
E1000	1000	6.70	$\alpha_1$
E1010	1010	6.74	$\alpha_1 \& \alpha_2$
E1050	1050	6.87	$\alpha_1 \& \alpha_2$
E1270	1270	7.56	$\alpha_1 \& \alpha_2$
E1280_1	1280	7.59	$\alpha_2$
E1280_2	1280	7.59	$\alpha_1$
E1280_3	1280	7.59	$\alpha_1$
E1290	1290	7.61	$\alpha_1 \& \alpha_2$
E1500_1	1500	8.21	$\alpha_1 \& \alpha_2$
E1500_2	1500	8.21	$\alpha_1 \& \alpha_2$

<sup>&</sup>lt;sup>1</sup>Remember that it is not clear whether the hydrogen atoms actually reached these energies. See subsection 3.7.1.

#### C.2 Listing of the Fit Parameters

In the following table, the fit parameter calculated for each measurement series and each transition are listed. The measurement series 'E1000' and 'E1280\_2' were not analyzed because the recorded spectra have too low a resolution.

Table C.2: List of the fit parameters for the analyzed measurement series.

measurement series	transition	$\frac{1}{A} = \Delta E_{Sona} \text{ [neV]}$	$B_{sca} [\mathrm{mT  s^{-1}}]$	$B_{off}$ [mT]
E990_1	$\alpha_1 - \alpha_2$	$6.62 \pm 0.06$	$1.682 \pm 0.026$	$-0.064 \pm 0.008$
	$\alpha_2 - \beta_3$	$5.5 \pm 0.5$	$1.51 \pm 0.09$	$-0.033 \pm 0.009$
E990_2	$\alpha_1 - \alpha_2$	$6.60 \pm 0.04$	$1.699 \pm 0.017$	$-0.054 \pm 0.005$
	$\alpha_2 - \beta_3$	$5.5 \pm 0.5$	$1.50 \pm 0.11$	$-0.038 \pm 0.010$
E1010	$\alpha_1 - \alpha_2$	$6.64 \pm 0.05$	$1.683 \pm 0.020$	$-0.068 \pm 0.006$
	$\alpha_2 - \beta_3$	$5.3 \pm 0.4$	$1.46 \pm 0.08$	$-0.048 \pm 0.008$
E1050	$\alpha_1 - \alpha_2$	$6.76 \pm 0.04$	$1.693 \pm 0.018$	$-0.067 \pm 0.006$
E1000	$\alpha_2 - \beta_3$	$5.7 \pm 0.6$	$1.51 \pm 0.11$	$-0.048 \pm 0.010$
E1270	$\alpha_1 - \alpha_2$	$7.44 \pm 0.05$	$1.664 \pm 0.016$	$-0.038 \pm 0.005$
	$\alpha_2 - \beta_3$	$6.2 \pm 0.5$	$1.50 \pm 0.09$	$-0.059 \pm 0.008$
E1280_1	$\alpha_2 - \beta_3$	$6.1 \pm 0.5$	$1.46 \pm 0.08$	$-0.041 \pm 0.008$
E1280_3	$\alpha_1 - \alpha_2$	$7.48 \pm 0.07$	$1.665 \pm 0.024$	$-0.071 \pm 0.007$
E1290	$\alpha_1 - \alpha_2$	$7.52 \pm 0.06$	$1.680 \pm 0.019$	$-0.060 \pm 0.006$
	$\alpha_2 - \beta_3$	$6.1 \pm 0.5$	$1.46 \pm 0.09$	$-0.064 \pm 0.007$
E1500_1	$\alpha_1 - \alpha_2$	$8.20 \pm 0.07$	$1.691 \pm 0.022$	$-0.070 \pm 0.007$
	$\alpha_2 - \beta_3$	$6.4 \pm 0.06$	$1.43 \pm 0.10$	$-0.044 \pm 0.009$
E1500_2	$\alpha_1 - \alpha_2$	$8.22 \pm 0.06$	$1.716 \pm 0.022$	$-0.095 \pm 0.007$
	$\alpha_2 - \beta_3$	$5.9 \pm 0.6$	$1.34 \pm 0.10$	$-0.058 \pm 0.009$

- [1] Joseph Fraunhofer. "Bestimmung des Brechungs- und des Farbenzerstreungs-Vermögens verschiedener Glasarten, in Bezug auf die Vervollkommung achromatischer Fernröhre". In: *Annalen der Physik* 56.7 (1817), pp. 264–313. DOI: https://doi.org/10.1002/andp.18170560706.
- [2] Johann Jakob Balmer. "Notizen über die Spektralinien des Wasserstoffs". In: Annalen der Physik 260.2 (1885), pp. 84–87.
- [3] R. Engels et al. "Precision Lamb-shift polarimeter for polarized atomic and ion beams". In: *Review of Scientific Instruments* 74.11 (2003), pp. 4607–4615. DOI: 10.1063/1.1619550.
- [4] Ralf Engels. "Entwicklung eines universellen Lambshift-Polarimeters für polarisierte Atomstrahltargets wie an ANKE/COSY". Record converted from VDB: 12.11.2012; Köln, Univ., Diss., 2002. Dr. (Univ.) Jülich: Univ. Köln, 2002. URL: https://juser.fz-juelich.de/record/23573.
- [5] Ralf Engels et al. "Measurement of the nuclear polarization of hydrogen and deuterium molecules using a Lamb-shift polarimeter". In: *Review of Scientific Instruments* 85.10 (2014), p. 103505. DOI: 10.1063/1.4897479.
- [6] R. Engels et al. "Production of HD Molecules in Definite Hyperfine Substates". In: Phys. Rev. Lett. 124.11 (2020), p. 113003. DOI: 10.1103/PhysRevLett.124.113003.
- [7] W. Schott et al. "An experiment for the measurement of the bound--decay of the free neutron". In: *The European Physical Journal A* 30 (2006), 603–611. DOI: 10.1140/epja/i2006-10136-3.
- [8] Ralf Engels et al. "Direct observation of transitions between quantum states with energy differences below 10 neV employing a Sona unit". In: *The European physical journal* / D 75.9 (2021), p. 257. DOI: 10.1140/epjd/s10053-021-00268-4.
- [9] G. Breit and I. I. Rabi. "Measurement of Nuclear Spin". In: *Phys. Rev.* 38.11 (1931), pp. 2082–2083. DOI: 10.1103/PhysRev.38.2082.2.
- [10] J.J. Thomson. "XL. Cathode Rays". In: The London, Edinburgh, and Dublin Philosophical Magazine and Journal of Science 44.269 (1897), pp. 293–316. DOI: 10.1080/14786449708621070.

[11] E. Rutherford. "LXXIX. The scattering of and particles by matter and the structure of the atom". In: *The London, Edinburgh, and Dublin Philosophical Magazine and Journal of Science* 21.125 (1911), pp. 669–688. DOI: 10.1080/14786440508637080.

- [12] N. Bohr. "I. On the constitution of atoms and molecules". In: *The London, Edinburgh, and Dublin Philosophical Magazine and Journal of Science* 26.151 (1913), pp. 1–25. DOI: 10.1080/14786441308634955.
- [13] Louis De Broglie. "Recherches sur la théorie des Quanta". Theses. Migration université en cours d'affectation, Nov. 1924. URL: https://tel.archives-ouvertes.fr/tel-00006807.
- [14] E. Schrödinger. "Quantisierung als Eigenwertproblem". In: Annalen der Physik 385.13 (1926), pp. 437–490. DOI: https://doi.org/10.1002/andp.19263851302.
- [15] Paul Adrien Maurice Dirac and Ralph Howard Fowler. "The quantum theory of the electron". In: Proceedings of the Royal Society of London. Series A, Containing Papers of a Mathematical and Physical Character 117.778 (1928), pp. 610–624. DOI: 10.1098/rspa.1928.0023.
- [16] W. Heisenberg. "Über den anschaulichen Inhalt der quantentheoretischen Kinematik und Mechanik". In: Zeitschrift für Physik 43.3 (1927), pp. 172–198. DOI: 10.1007/BF01397280.
- [17] Walther Gerlach and Otto Stern. "I. On the constitution of atoms and molecules". In: Zeitschrift für Physik 9.1 (1922), pp. 349–352. DOI: 10.1007/BF01326983.
- [18] Lukas Huxold. "A Lamb-Shift Polarimeter for a Molecular Beam Source and Further Applications". Dissertation, HHU Düsseldorf, 2021. PhD thesis. Jülich: HHU Düsseldorf, 2021, p. 148. URL: http://juser.fz-juelich.de/record/902255.
- [19] G. E. UHLENBECK and S. GOUDSMIT. "Spinning Electrons and the Structure of Spectra". In: Nature 117.2938 (1926), pp. 264–265. DOI: 10.1038/117264a0.
- [20] T. E. Phipps and J. B. Taylor. "The Magnetic Moment of the Hydrogen Atom". In: Phys. Rev. 29.2 (1927), pp. 309-320. DOI: 10.1103/PhysRev.29.309. URL: https://link.aps.org/doi/10.1103/PhysRev.29.309.
- [21] Peter J. Mohr, David B. Newell, and Barry N. Taylor. "CODATA recommended values of the fundamental physical constants: 2014". In: *Reviews of Modern Physics* 88.3 (2016). DOI: 10.1103/revmodphys.88.035009.
- [22] A.A. Michelson and E.W. Morley. "On a Mehtod of making the Wavelength of Sodium Light the actual and practical standard of length". In: *The American Journal of Science*. 3rd ser. 34 (1887), p. 427. URL: https://archive.org/details/americanjourna3341887newh/page/427/mode/2up.
- [23] W. V. Houston. "A New Method of Analysis of the Structure of H $\alpha$  and D $\alpha$ ". In: *Phys. Rev.* 51.6 (1937), pp. 446–449. DOI: 10.1103/PhysRev.51.446.

[24] Simon Pasternack. "Note on the Fine Structure of H $\alpha$  and D $\alpha$ ". In: *Phys. Rev.* 54.12 (1938), p. 1113. DOI: 10.1103/PhysRev.54.1113. URL: https://link.aps.org/doi/10.1103/PhysRev.54.1113.

- [25] Robley C. Williams. "The Fine Structures of H $\alpha$  and D $\alpha$  Under Varying Discharge Conditions". In: *Phys. Rev.* 54.8 (1938), pp. 558–567. DOI: 10.1103/PhysRev.54.558.
- [26] Willis E. Lamb and Robert C. Retherford. "Fine Structure of the Hydrogen Atom by a Microwave Method". In: *Phys. Rev.* 72.3 (1947), pp. 241–243. DOI: 10.1103/PhysRev.72.241.
- [27] R. P. Feynman. "Space-Time Approach to Non-Relativistic Quantum Mechanics". In: *Rev. Mod. Phys.* 20.2 (1948), pp. 367–387. DOI: 10.1103/RevModPhys. 20.367.
- [28] W. Demtröder. Experimentalphysik 3: Atome, Moleküle und Festkörper. Springer-Lehrbuch. Springer Berlin Heidelberg, 2016. ISBN: 9783662490945. URL: https://books.google.de/books?id=tR5kDAAAQBAJ.
- [29] Pieter Zeeman. "The Effect of Magnetisation on the Nature of Light Emitted by a Substance". In: *Nature* 55.1424 (1897), p. 347. DOI: 10.1038/055347a0.
- [30] Paschen F. and E. Back. "Liniengurppen magnetisch vervollständigt". In: *Physica* 1 (1921), pp. 261–273.
- [31] T. P. Hezel et al. "Classical view of the Stark effect in hydrogen atoms". In: American Journal of Physics 60.4 (1992), pp. 324–328. DOI: 10.1119/1.16875.
- [32] D. L. Moskovkin and V. M. Shabaev. "Zeeman effect of the hyperfine-structure levels in hydrogenlike ions". In: *Phys. Rev. A* 73.5 (2006), p. 052506. DOI: 10.1103/PhysRevA.73.052506.
- [33] Willy Wien. "Untersuchungen über die electrische Entladung in verdünnten Gasen". In: *Annalen der Physik* 301.6 (1898), pp. 440–452. DOI: https://doi.org/10.1002/andp.18983010618.
- [34] P. Pradel et al. "Formation of H(n=2) atoms by the nearly resonant process  $H^+$  in Cs. Multiple collision processes". In: *Phys. Rev. A* 10.3 (1974), pp. 797–812. DOI: 10.1103/PhysRevA.10.797.
- [35] Joseph L. McKibben, George P. Lawrence, and Gerald G. Ohlsen. "Nuclear Spin Filter". In: *Phys. Rev. Lett.* 20.21 (1968), pp. 1180–1182. DOI: 10.1103/PhysRevLett.20.1180.
- [36] C. Schwob et al. "Optical Frequency Measurement of the 2S-12D Transitions in Hydrogen and Deuterium: Rydberg Constant and Lamb Shift Determinations". In: *Phys. Rev. Lett.* 82.25 (1999), pp. 4960–4963. DOI: 10.1103/PhysRevLett. 82.4960.
- [37] P.G. Sona. "A new method proposed to increase polarization in polarized ion sources of H<sup>-</sup> and D<sup>-(\*)</sup>". In: *Energia Nucleare* 14 (1967), pp. 295–299.

[38] M. P. Westig. "Preparation of a Precision Spectroscopy Measurement of Metastable Hydrogen and Deuterium with a Lamb-shift Polarimeter". Diplom (Univ.) Jülich: Univ. Köln, 2008. URL: https://juser.fz-juelich.de/record/2364.

## Acknowledgements

At the end of my thesis, I would like to say a few words of thanks to all those who have contributed to the creation of this thesis.

First of all, I would like to thank all my co-workers at the IKP. Nothing in Experimental Physics would be possible without the help of the various workshops and working groups. For every problem that came up, there was always someone you could ask for help and with experience to learn from. Even in the troubled times of Corona, productive work was always possible.

Next, I would like to thank the Forschungszentrum Jülich for allowing me to properly complete my thesis by extending my employment for three months after the actual experiment that was intended to be the topic of my thesis was not feasible due to delays caused by the Corona pandemic.

In particular, my special thanks goes to:

Ralf Engels, my (informal) supervisor, thanks to you I was able to work at the IKP again. You gave me the opportunity to do and learn the practical basics and details of experimental physics, which are unfortunately so often neglected at university. I have had the opportunity to get a glimpse of real research again. I believe that I have gained more experience in performing experiments in these last 15 months than during my entire time at university before. I have learned a lot from our discussions and your tireless drive to try to explain everything. And of course, I would also like to thank you for proofreading this thesis and helping to improve its structure and readability.

Another special thanks goes to my colleague Chrysovalantis Kannis, with whom I set out to find the correct Breit-Rabi formulas. It was quite an educational adventure that showed me once again what a tiny difference a simple sign can make and how complicated it can be to determine the correct one with sufficient certainty. Thank you for all the discussions and for taking the time to explain a lot of things to me, especially regarding the Sona transition unit and other parts of the experiment, that was very helpful.

All the other students who were part of our working group during my time at the IKP, Philipp Schnicke, Onur Bilen, Jonas Salmann, Moritz Westphal, Simon Pütz, Aditya Mandiwal, and Nicolas Faatz. Thank you for the pleasant working atmosphere and the constructive exchange. Discussing with you really helped me to better understand what we were doing and to always question myself, whether I really understood it or not.

Furthermore, I would like to thank Prof. Andreas Lehrach for becoming my supervisor and giving me the opportunity to work in Ralf Engels' group again. I am also grateful for the opportunity to gain insight into teaching at the university as part of the accelerator lecture tutorial team over the past year and a half, as well as for the great understanding related to the delay caused by the change in my thesis topic.

At last, I would like to address a few words of thanks to my parents and my sister in my native language, German.

Ein langer Weg liegt hinter mir. Doch jetzt nach all den Jahren und einigen teils ungewollten Abzweigungen ist dieser Teil endlich ans Ende gekommen.

Mutter, Vater, Isabel,

ich glaube das ein Großteil meines Studium, dieser Arbeit und wahrscheinlich auch ein Großteil von dem, was ich in Zukunft machen werde, für euch etwas sehr Abstraktes und Fremdes ist, mit dem ihr wenig anfangen könnt. Dennoch habt ihr mich immer unterstützt und lasst mich meinen Weg gehen, so wie ich es für richtig halte. Ganz besonders euch meinen Eltern, möchte ich dafür danken, gerade weil ich weiß, dass ihr beide diese Freiheit nicht hattet. Ohne eure Unterstützung und auch deine Isabel, hätte ich nicht erreichen können, was ich nun geschafft habe. Ich danke euch von ganzem Herzen.